UNIVERSITY OF CALIFORNIA, SAN DIEGO

Mathematical Analysis of Signal Transduction and Information Measurement in Cells

A dissertation submitted in partial satisfaction of the
requirements for the degree
Doctor of Philosophy

in

Physics (Biophysics)

by

Wen Chen

Committee in charge:

Herbert Levine, Chair
Alex Groisman
José Onuchic
Wouter-Jan Rappel
Ruth J. Williams
Jack K. Wolf

2011

The dissertation of Wen Chen is approved, and it is acceptable in quality and form for publication on microfilm and electronically:

_____

_____

_____

_____

_____

_____

Chair

University of California, San Diego

2011

DEDICATION

To my parents.

EPIGRAPH

Imagination is more important than knowledge. For knowledge is limited to all we now know and understand, while imagination embraces the entire world, and all there ever will be to know and understand.

—Albert Einstein

TABLE OF CONTENTS

Signature Page iii

Dedication iv

Epigraph v

Table of Contents vi

List of Figures viii

Acknowledgements ix

Vita and Publications xi

Abstract of the Dissertation xii

Chapter 1 Introduction 1

Chapter 2 Second Messenger Compartmentalization 4
2.1 A mathematical analysis of second messenger compartmentalization 4
2.1.1 Introduction 4
2.1.2 Compartment Model 6
2.1.3 Analytical Steady State Solution 8
2.1.4 Results and discussion 10
2.2 Compartmentalization of Second Messengers in Neurons: a Mathematical Analysis 19
2.2.1 Introduction 19
2.2.2 Model 21
2.2.3 Results 23
2.2.4 Discussion 28
2.3 Acknowledgements 30

Chapter 3 Gradient Sensing 32
3.1 External and internal constraints on eukaryotic chemotaxis 32
3.1.1 Introduction 32
3.1.2 Results 34
3.1.3 Discussion 40
3.2 Estimation Theory of Eukaryotic Gradient Sensing 42
3.2.1 Introduction 42
3.2.2 Gradient sensing for a circular cell 44
3.2.3 Summary 51

3.3 Acknowledgements 52

Chapter 4 Biological Switch 53
4.1 Introduction 53
4.2 Model 54
4.3 Discussion 61

Appendix A Laplace Transforms 63
A.1 Region 1 65
A.2 Region 2 70

Appendix B Proof of equation (2.43) 73

Appendix C 3D model of cAMP distribution 75

Appendix D Calculation of mutual information 80
D.1 External Mutual Information 80
D.1.1 Exponential Gradient 81
D.1.2 Linear Gradient 87
D.1.3 Comparison between the numerical and analytical results 87
D.2 External and Internal Mutual Information 88

Bibliography 91

LIST OF FIGURES

Figure 2.1: Geometry of cAMP compartmentalization 7
Figure 2.2: Normalized concentration of distance 12
Figure 2.3: Normalized concentration of time 15
Figure 2.4: Concentration profile 17
Figure 2.5: Simplified geometry of a neuron 22
Figure 2.6: Concentration in dendrite 27
Figure 2.7: Gradient at soma-dendrite junction 27
Figure 2.8: cAMP distribution without degradation 29
Figure 2.9: cAMP distribution 29

Figure 3.1: Chemotactic response of cells 35
Figure 3.2: Chemotactic index 36
Figure 3.3: Mutual information 39

Figure 4.1: Illustration of model 55
Figure 4.2: Results of CIR model 58
Figure 4.3: Statistics of CIR model 60

Figure A.1: Contour integral for region 1 66
Figure A.2: Contour integral for region 2 70

Figure D.1: Sector number 87
Figure D.2: Cost function 89

ACKNOWLEDGEMENTS

This dissertation would not have been possible without the support of many people.

I would first like to express my deep and sincere gratitude to my advisor, Herbert Levine, for accepting me into his group and giving me the freedom, patience and guidance during the past five years of research. I am impressed by his wisdom and wide knowledge. I am also very grateful to Wouter-Jan Rappel for his collaboration, support and mentoring. Herbert and Wouter were always there when I had questions and helped me going through difficulties.

I am truly grateful to Alex Groisman, José Onuchic, Ruth Williams, and Jack Wolf for being my mentors and teachers, serving as my committee members, and providing invaluable advices on my research. Alex is a great experimental physicist, and it is he who provided the microfluid device to make our chemotaxis research go through well. José is a great leader and an admiring role model in science, who stimulates me to contribute high quality of research. They are priceless treasures and the department is lucky to have them. Ruth is one of the greatest mathematicians I have ever met. I appreciate all the time I spent under her instructions. It is her amazing classes which introduced me into the fantastic world of stochasticity. Jack and his wife Toby are not only my teachers but also my dearest friends. They are extremely helpful in every aspect of my life.

I must also thank my collaborators: William F. Loomis, Danny Fuller, and Micha Adler. Without them this dissertation could not have been written. William is always patient and ready to answer biology questions. Danny and Micha provided the valuable data for our research. I feel honored to have worked with them.

Finally, I wish to thank my family and friends. My parents have always believed in me and their support forged my desire to achieve all that I could in life. My fiancé, Bo Hu, whose love and encouragement allowed me to finish this journey. I wish I could show my family how much I love and appreciate them. The people I have met while in graduate school have become my friends, and counselors, and to all of them I give my love and thanks.

Chapter 2, in part, contains the published material as it appears in "A mathematical analysis of second messenger compartmentalization", Wen Chen, Herbert Levine, and Wouter-Jan Rappel, *Physical Biology*, **5**, 046006 (2008), and "Compartmentalization of second messenger in neurons: A mathematical analysis", Wen Chen, Herbert Levine, and Wouter-Jan Rappel, *Phys. Rev. E*, **80**, 041901 (2009). The dissertation author was the primary investigator and author of these papers.

Chapter 3, in part, contains the published material as it appears in "External and internal constraints on eukaryotic chemotaxis", Danny Fuller, Wen Chen, Micha Alder, Alex Groisman, Herbert Levine, Wouter-Jan Rappel and Williams F. Loomis, *Proc. Nat. Acad. Sci. USA*, **107**, 9656 (2010), and "How geometry and internal bias affect the accuracy of eukaryotic gradient sensing", Bo Hu, Wen Chen, Wouter-Jan Rappel, and Herbert Levine, *Physical Review E*, **83**, 021917 (2011). The dissertation author was the primary investigator and author of these papers.

VITA

2011	Ph. D. in Physics, University of California, San Diego
2007	M. S. in Physics, University of California, San Diego
2005	B. S. in Physics, University of Science and Technology of China

PUBLICATIONS

Bo Hu, Wen Chen, Wouter-Jan Rappel, and Herbert Levine, "How geometry and internal bias affect the accuracy of eukaryotic gradient sensing." *Physical Review E*, **83**, 021917 (2011).

Bo Hu, Wen Chen, Herbert Levine, and Wouter-Jan Rappel, "Quantifying Information Transmission in Eukaryotic Gradient Sensing and Chemotactic Response." *Journal of Statistical Physics*, **142**, 1167, (2011).

Bo Hu, Wen Chen, Wouter-Jan Rappel, and Herbert Levine, "Physical limits on cellular sensing of spatial gradients." *Physical Review Letters*, **105**, 0481041 (2010).

Danny Fuller, Wen Chen, Micha Alder, Alex Groisman, Herbert Levine, Wouter-Jan Rappel and Williams F. Loomis, "External and internal constraints on eukaryotic chemotaxis", *Proc. Nat. Acad. Sci. USA*, **107**, 9656 (2010)

Wen Chen, Herbert Levine, and Wouter-Jan Rappel, "Compartmentalization of second messenger in neurons: A mathematical analysis", *Phys. Rev. E*, **80**, 041901 (2009)

Wen Chen, Herbert Levine, and Wouter-Jan Rappel, "A mathematical analysis of second messenger compartmentalization", *Physical Biology*, **5**, 046006 (2008)

ABSTRACT OF THE DISSERTATION

Mathematical Analysis of Signal Transduction and Information Measurement in Cells

by

Wen Chen

Doctor of Philosophy in Physics (Biophysics)

University of California, San Diego, 2011

Herbert Levine, Chair

In biology signal transduction is the process by which an extracellular signaling molecule activates a membrane receptor that in turn alters intracellular molecules creating a response. The chemical signal binds to the outer portion of the receptors, which span the cell membrane with part outside the cell, changing its shape and conveying another signal inside the cell. Some chemical messengers can pass through the cell membrane, and bind directly to receptors in the cytoplasm or nucleus. Sometimes there is a cascade of signals within the cell. With each step of the cascade, the signal can be amplified, so a small signal can result in a large response. Eventually, the signal creates a change in the cell, either in the expression of genes in the nucleus or in the activity of enzymes in the cytoplasm.

Since signal transduction and information measurement are so important for the cell, we are aiming to theoretically understand how signals are transferred inside cell and how cell measures its environment information.

The first part of this dissertation focused on the compartmentalization of second messengers. Intracellular signal transduction is largely carried out by second messenger molecules. It is well known that a variety of signaling pathways can share a common second messenger, generated through different external stimuli. Obviously, this leads to the potential of cross-talk between these pathways. One possibility to avoid this cross-talk and thus ensure pathway specificity is to create spatial regions in which the concentration of the second messenger is markedly different. By spatially localizing the targets of the second messenger in these microdomains it would be possible to excite different pathways for different external stimuli. The second part of this dissertation studied how cell as a information processing machine senses chemical gradients in its environment. Using information theory, a formula for the mutual information between the input gradient and the spatial distribution of bound receptors was derived. By estimation theoretic methods, the physical limits of gradient sensing was also determined for both circular and ellipse cells. The third part of this dissertation investigated how biological processes are controlled by biochemical switches which are regulated by upstream signal, in order to understand how input fluctuation affect the dynamic of a molecular switch. This understanding is critical toward a full understanding of noise regulation in biological signaling systems.

Chapter 1

Introduction

This dissertation mainly contains three parts, which cover different aspects of signal transduction and information measurement in cells. First, it is well known that a large number of signaling pathways share the same second messengers. How to avoid cross-talk to achieve signaling specificity is one major concern of signal transduction in cells. Chapter two aims to give a possible solution to this signaling specificity problem. One of the other topics is chemotaxis, the chemically guided movement of cells, which plays an important role in several biological processes including cancer, wound healing, and embryogenesis. Many motile cells determines their direction by measuring external chemical gradients through the binding of ligands to membrane bound receptors. The physical limit of this measurement is discussed in Chapter three. The topic discussed in Chapter four is biochemical switches, which are regulated by certain upstream molecules. Understanding how the noise of upstream chemical signal affects downstream switch is important to understand the signal transduction in a biochemical cascade.

Chapter two studies intracellular compartmentalization of a second messenger, which leads to microdomains of elevated concentration. The elevated concentration is thought to be involved in ensuring signaling specificity. Most experimental evidence for this compartmentalization involves the second messenger adenosine monophosphate (cAMP), which is degraded by phosphodiesterases (PDEs). One possible way of creating these compartments, supported by recent experiments, is to spatially separate the source of cAMP from regions of elevated PDE concen-

tration. To quantify this possibility, we study here a simplified geometry in two dimensions (2D) and in three dimensions (3D), containing a cAMP point source and regions with different degradation constants. Using the symmetry of our geometry, we are able to derive steady state solutions for the cAMP concentration as a function of the system parameters. Furthermore, we show, using analytical as well as direct numerical simulations, that for physiologically relevant time scales the steady state solution has been reached. Our results indicate that elevating the degradation constant throughout the cell, except for a small microdomain surrounding the source, requires an unphysiologically high cellular PDE concentration. On the other hand, a tight spatial relationship of localized PDEs with the cAMP source can result in functional microdomains while maintaining a physiologically plausible cellular PDE concentration. Some experiments in hippocampal neurons have demonstrated the existence of compartments with elevated levels of second messenger molecules such as cAMP. This compartmentalization is believed to be necessary to ensure downstream signaling specificity. Here we use analytical and numerical techniques to investigate the diffusion of a second messenger in the soma and in the dendrite of a neuron. We obtain analytical solutions for the diffusion field and examine the limit in which the width of the dendrite is much smaller than the radius of the soma. We find that the concentration profile depends both the degradation rate and the width of the dendrite and that compartmentalization can be indeed be achieved for small width to soma radius ratio.

Chapter three studies eukaryotic chemotaxis. Chemotacting cells are able to sense shallow chemical gradients where the concentration of chemoattractant differs by only a few percent from one side of the cell to the other, over a wide range of local concentrations. Exactly what limits the chemotactic ability of these cells is presently unclear. Here we determine the chemotactic response of Dictyostelium cells to exponential gradients of varying steepness and local concentration of the chemoattractant cAMP. We find that the cells are sensitive to the steepness of the gradient as well as to the local concentration. Using information theory techniques, we derive a formula for the mutual information between the input gradient and the spatial distribution of bound receptors and also compute the mutual informa-

tion between the input gradient and the motility direction in the experiments. A comparison between these quantities reveals that for shallow gradients, in which the concentration difference between the back and the front of a $10\mu m$-diameter cell is $< 5\%$, and for small local concentrations ($< 10nM$) the intracellular information loss is insignificant. Thus, external fluctuations due to the finite number of receptors dominate and limit the chemotactic response. For steeper gradients and higher local concentrations, the intracellular information processing is suboptimal and results in a smaller mutual information between the input gradient and the motility direction than would have been predicted from the ligand-receptor binding process. In this chapter, we apply estimation-theoretic methods to determine the physical limits of gradient sensing for cells that are non-circular and for cells that have an internal bias. Specifically, we derive theoretical expressions for the accuracy of gradient sensing in elliptical cells. This accuracy for highly elliptical cells can significantly deviate from the gradient sensing limits derived for circular cells. Furthermore, we find that a cell cannot improve its sensing of the gradient steepness and direction simultaneously by elongating its cell body. Finally, we derive a lower bound on the accuracy of gradient sensing for cells that possess an internal bias and compare our analytical results with recent experimental findings.

Chapter four studies biochemical switches. Many biological processes are controlled by biochemical switches which themselves are regulated by certain upstream molecules (input). Understanding how input fluctuations affect the dynamics of a molecular switch is critical toward a full understanding of noise regulation in biological signaling systems. In this chapter, we propose a simple and general modeling framework in which the input signal, described by certain Markov diffusion process, directly modulate the transition rates of a downstream switch. We apply the Feynman-Kac theorem to characterize the probabilistic structure of the output switching process. Together with Monte-Carlo simulations, we show that our model system can exhibit a wide range of interesting dynamics, potentially corresponding to various important biophysical schemes. Our results suggest that the conventional additive input-output noise relationship is insufficient to describe signaling systems containing a single molecular switch.

Chapter 2

Second Messenger Compartmentalization

2.1 A mathematical analysis of second messenger compartmentalization

2.1.1 Introduction

It has long been known that a large number of signaling pathways can share a common second messenger, generated through a variety of different external stimuli. Obviously, this leads to the potential of cross-talk between these pathways in which an external stimulation excites multiple pathways in an indiscriminate manner. One possibility to avoid this cross-talk and thus ensuring pathway specificity is to create spatial regions in which the concentration of the second messenger is markedly different. By spatially localizing the targets of the second messenger in these microdomains it would be possible to excite different pathways for different external stimuli.

Most of the evidence for this compartmentalization comes from work studying cyclic adenosine monophosphate (cAMP) pathways. cAMP is a ubiquitous second messenger, involved in a multitude of processes including differentiation, development, and excitation/contraction coupling in muscle cells. cAMP primarily

activates the cAMP-dependent protein kinase (PKA) and is generated by membrane bound adenylyl cyclases (ACs) which, in turn, are activated by transmembrane receptors [1]. Experimental evidence has demonstrated that different stimuli can result in the activation of different downstream pathways [2]. In other words, cAMP-dependent pathways can be activated in a selective and specific fashion. This is surprising since cAMP is a small molecule with a large diffusion coefficient and thus any local elevation in cAMP concentration should rapidly lead to a homogeneous increase in cytosolic cell-wide cAMP levels.

The existence of cAMP microdomains was demonstrated in recent high resolution fluorescence resonance energy transfer (FRET) experiments with submicrometer resolution. These experiments showed that cardiac myocytes, following β-adrenergic stimulation, displayed multiple discrete microdomains of high cAMP concentration [3]. This compartmentalization is thought to play an important role in functional differences between β_1-adrenergic and β_2-adrenergic signaling [2, 4, 5, 6] and might be impaired during heart failure. Similar spatial cAMP gradients have also been found in human embryonic kidney cells [7] and hippocampal neurons [8].

Two scenarios to limit the spatial extent of the second messenger, and thus ensuring specificity, have been postulated. In the first, the cell geometry creates anatomical barriers that naturally limits the diffusion of cAMP. In the second scenario, the degradation of cAMP by phosphodiesterases (PDEs) acts to create a "functional" compartment [9]. These PDEs exist in many isoenzyme variants and have been shown to act either close to the membrane, in the cytosol or both [10]. Recent experiments have shown that the microdomains of cAMP can be abolished by treating the cells with a PDE inhibitor [11], strongly suggesting that the second scenario plays a dominant role in the creation of cAMP microdomains. In fact, additional experiments have demonstrated that the PDEs themselves are not uniformly distributed throughout the cell [12, 13]. Instead, they appear to be anchored to subcellular structures, possibly through A-kinase anchoring protein (AKAP) [14].

Several modeling studies have addressed the β-adrenergic pathway in my-

ocytes [15, 16]. What has been lacking to date, however, is a quantitative and analytical investigation of the effect of PDEs on the spatial distribution of cAMP. In this study we will examine a simplified spherically symmetric model in which molecules from a point source, located on an impermeable membrane, diffuse into a space that contains a region of elevated PDE concentration. Note that our model does not address localization effects that might arise from more complicated geometries. This was shown to occur in a recent numerical study in neurons where the different surface-to-volume ratios for the cell body and for the dendrites can lead to significant concentration gradients [17]. In addition, we do not include possible feedback from cAMP on the PDEs, as considered in [17].

In this study, we derive expressions for the steady state concentration in both 2D and 3D and obtain a simple expression that links the critical experimental parameters (the size of the microdomain, the diffusion constant of the second messenger, the production rate and the degradation constant) to a threshold value for PKA activation of the cAMP concentration. We find that a significant lowering of the concentration requires a large value of the degradation constant. If the PDEs are only excluded from the microdomain adjacent to the cAMP source, such a large degradation constant would necessitate cellular PDE concentrations that are unphysiological. On the other hand, our results show that a tight localization of PDEs can also create functional cAMP microdomains and that by limiting the spatial extent of PDEs the cellular PDE concentration can remain in the physiological range.

2.1.2 Compartment Model

The detailed cellular geometry of the cAMP machinery, including the location of PDEs is complex and not precisely known. Therefore, we have chosen a highly simplified geometry, depicted in Fig. 2.1, that is amenable to an analytical treatment. In this geometry, we consider the cell to occupy the half space below a reflecting boundary. A source is located at the origin, emitting molecules that can diffuse into the cell. As we are interested in the general localization properties of the ensuing diffusion, we do not specify the detailed nature of this source.

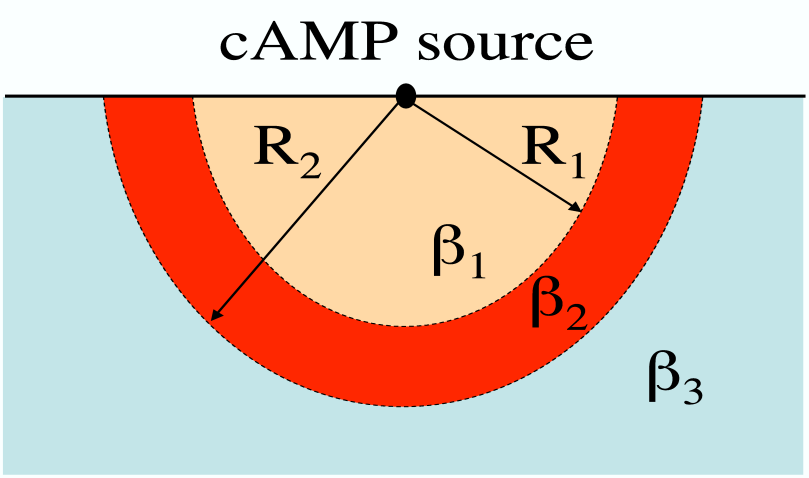

Figure 2.1: The geometry considered in this paper. A point source emits cAMP molecules into the unbounded half space below the reflecting membrane. The cAMP molecules diffuse freely but the degradation rate β is non-uniform: it is low in the first compartment, of size R_1, and second compartment ($r \geq R_2$) but is high in the region $R_1 < r < R_2$.

Furthermore, since we assume that the spatial scale of the source is much smaller that the cell body, we will consider a point source that emits molecules into an infinite domain. The effect of different zones of degradation in the cell is modeled by defining three regions with different degradation constants: a region of radius R_1 with degradation rate β_1, a region $R_1 < r < R_2$ with degradation rate β_2 and a region which extends beyond R_2 and which has a degradation constant β_3. Of course, since we are investigating scenarios where the degradation constant can form microdomains, we will be most interested in the case where β_2 is much larger than β_1.

The concentration in the microdomain, C_1, in the high degradation zone, C_2, and in the remainder of the cytosol, C_3, obey the diffusion equation:

$$\begin{aligned} \frac{\partial C_1}{\partial t} &= D\nabla^2 C_1 - \beta_1 C_1,\ 0 \leq r \leq R_1 \\ \frac{\partial C_2}{\partial t} &= D\nabla^2 C_2 - \beta_2 C_2,\ R_1 < r < R_2 \\ \frac{\partial C_3}{\partial t} &= D\nabla^2 C_3 - \beta_3 C_3,\ r \geq R_2 \end{aligned} \tag{2.1}$$

At the boundary separating the three regions, both the concentration and its derivative must be continuous:

$$\begin{aligned} C_1(R_1,t) &= C_2(R_1,t) \\ C_2(R_2,t) &= C_3(R_2,t) \end{aligned} \tag{2.2}$$

$$\begin{aligned} \frac{\partial C_1(R_1,t)}{\partial r} &= \frac{\partial C_2(R_1,t)}{\partial r} \\ \frac{\partial C_2(R_2,t)}{\partial r} &= \frac{\partial C_3(R_2,t)}{\partial r} \end{aligned} \tag{2.3}$$

while far from the source we have

$$C_3(\infty,t) = 0 \tag{2.4}$$

Finally, we assume that the initial concentration is zero throughout the domain:

$$C_1(r,0) = C_2(r,0) = C_3(r,0) = 0 \tag{2.5}$$

2.1.3 Analytical Steady State Solution

Two dimensions

The steady state solution for the concentration field in two dimensions can be found using the angular symmetry and writing the diffusion equation in polar coordinates. In these coordinates, the proper boundary condition for a constant source of F molecules/s reads

$$\lim_{r\to 0} r\frac{\partial C_1}{\partial r} = -\frac{F}{\pi D} \tag{2.6}$$

This, along with the boundary conditions at $r = R_1$ and $r = R_2$, can be used to find a general solution in terms of the flux F, the diffusion constant D, the degradation constants β_1, β_2, and β_3 and the radii of the compartments:

$$
\begin{aligned}
C_1(r) &= \frac{F}{\pi D}\left(A_1\frac{K_0(\alpha_1 r)}{K_0(\alpha_1 R_1)} + A_2\frac{I_0(\alpha_1 r)}{I_0(\alpha_1 R_1)}\right) \\
C_2(r) &= \frac{F}{\pi D}\left(B_1\frac{K_0(\alpha_2 r)}{K_0(\alpha_2 R_2)} + B_2\frac{I_0(\alpha_2 r)}{I_0(\alpha_2 R_2)}\right) \\
C_3(r) &= \frac{F}{\pi D}(B_1 + B_2)\frac{K_0(\alpha_3 r)}{K_0(\alpha_3 R_2)}
\end{aligned} \tag{2.7}
$$

where $\alpha_i = \sqrt{\frac{\beta_i}{D}}$ for $i = 1, 2, 3$. Here, and in the remainder of the paper, I_n and K_n represent the modified Bessel function of the first kind and second kind of order n (see, e.g. [18]). The coefficients are given by

$$
\begin{aligned}
A_1 &= K_0(\alpha_1 R_1) \\
B_1 &= \frac{dA_1}{b + ac} \\
B_2 &= aB_1 \\
A_2 &= \frac{K_0(\alpha_2 R_1)}{K_0(\alpha_2 R_2)}B_1 + \frac{I_0(\alpha_2 R_1)}{I_0(\alpha_2 R_2)}B_2 - A_1
\end{aligned}
$$

with

$$
\begin{aligned}
a &= \frac{\frac{\alpha_2 K_1(\alpha_2 R_2)}{K_0(\alpha_2 R_2)} - \frac{\alpha_3 K_1(\alpha_3 R_2)}{K_0(\alpha_3 R_2)}}{\frac{\alpha_2 I_1(\alpha_2 R_2)}{I_0(\alpha_2 R_2)} + \frac{\alpha_3 K_1(\alpha_3 R_2)}{K_0(\alpha_3 R_2)}} \\
b &= \alpha_1\frac{I_1(\alpha_1 R_1)K_0(\alpha_2 R_1)}{I_0(\alpha_1 R_1)K_0(\alpha_2 R_2)} + \alpha_2\frac{K_1(\alpha_2 R_1)}{K_0(\alpha_2 R_1)} \\
c &= \alpha_1\frac{I_1(\alpha_1 R_1)I_0(\alpha_2 R_1)}{I_0(\alpha_1 R_1)I_0(\alpha_2 R_2)} - \alpha_2\frac{I_1(\alpha_2 R_1)}{I_0(\alpha_2 R_2)} \\
d &= \alpha_1\left(\frac{K_1(\alpha_1 R_1)}{K_0(\alpha_1 R_1)} + \frac{I_1(\alpha_1 R_1)}{I_0(\alpha_1 R_1)}\right)
\end{aligned}
$$

Note that for the special case of uniform degradation $\alpha_1 = \alpha_2 \equiv \alpha$ the solution simplifies to

$$
C_{uni}(r) = \frac{F}{\pi D}K_0(\alpha r) \tag{2.8}
$$

Three dimensions

In three dimensions the diffusion equations can be written in spherical coordinates while the proper flux condition reads

$$\lim_{r\to 0} r^2 \frac{\partial c_1}{\partial r} = -\frac{F}{2\pi D} \tag{2.9}$$

Now, the solution is written in terms of modified spherical Bessel functions k_n and i_n [18]. To distinguish our 3D steady state results from the 2D results we will denote the 3D solutions in lower case:

$$\begin{aligned} c_1(r) &= \frac{F}{2\pi D}\left(A_1' \frac{k_0(\alpha_1 r)}{k_0(\alpha_1 R_1)} + A_2' \frac{i_0(\alpha_1 r)}{i_0(\alpha_1 R_1)}\right) \\ c_2(r) &= \frac{F}{2\pi D}\left(B_1' \frac{k_0(\alpha_2 r)}{k_0(\alpha_2 R_2)} + B_2' \frac{i_0(\alpha_2 r)}{i_0(\alpha_2 R_2)}\right) \\ c_3(r) = &= \frac{F}{2\pi D}(B_1' + B_2') \frac{k_0(\alpha_3 r)}{k_0(\alpha_3 R_2)} \end{aligned}$$

The expressions for the coefficients are identical to the ones in 2D with K_n and I_n replaced by k_n and i_n, respectively and with

$$A_1' = \alpha_1 k_0(\alpha_1 R_1)$$

For completeness, we also give the solution for uniform degradation

$$c_{uni}(r) = \frac{F\alpha}{2\pi D} k_0(\alpha r) \tag{2.10}$$

and for free diffusion ($\alpha_1 = \alpha_2 = \alpha_3 = 0$)

$$c_{free}(r) = \frac{F}{2\pi D}\frac{1}{r} \tag{2.11}$$

2.1.4 Results and discussion

$R_2 \to \infty$

We first address the case of an infinite compartment with high degradation, i.e. $R_2 \to \infty$. In this case, the steady state solutions can be simplified considerably,

leading to

$$\begin{aligned} C_1(r) &= \frac{F}{\pi D}\left(A_1\frac{K_0(\alpha_1 r)}{K_0(\alpha_1 R)} + A_2\frac{I_0(\alpha_1 r)}{I_0(\alpha_1 R)}\right) \\ C_2(r) &= \frac{F}{\pi D}(A_1 + A_2)\frac{K_0(\alpha_2 r)}{K_0(\alpha_2 R)} \end{aligned} \tag{2.12}$$

with

$$A_1 = K_0(\alpha_1 R) \tag{2.13}$$

$$A_2 = \frac{\alpha_1 K_0(\alpha_2 R)K_1(\alpha_1 R)I_0(\alpha_1 R) - \alpha_2 K_0(\alpha_1 R)K_1(\alpha_2 R)I_0(\alpha_1 R)}{\alpha_1 I_1(\alpha_1 R)K_0(\alpha_2 R) + \alpha_2 K_1(\alpha_2 R)I_0(\alpha_1 R)} \tag{2.14}$$

where we have defined $R \equiv R_1$. The 3D solutions can be found from these expression by replacing K_n and I_n with k_n and i_n, the prefactor with $F/(2\pi DR)$ and A_1 with A_1'. In Fig. 2.2A we show the concentration, normalized by the prefactor of Eq. 2.12, as a function of the radial distance from the source for several values of the degradation constant β_2. The first compartment has radius $R = 0.1\mu m$, indicated by the dashed line, and was chosen to have a negligible degradation constant. As expected, the effect of the degradation in the second compartment becomes more pronounced for larger values of the degradation constant.

In Fig. 2.2B we show a similar set of curves, but now for the 3D case. Again, the concentration profile is normalized by the prefactor $(F/(2\pi DR))$ and is markedly altered for large values of the degradation constant. As a comparison, we have also plotted the concentration for the freely diffusion case (i.e., $\beta_i = 0$). Note that such a comparison can not be made in 2D since there the free diffusion profile diverges ($C_{free} \sim ln(r)$).

Obviously, the presence of a non-zero degradation constant reduces the concentration, especially for large values of β_2. To quantify the effect of the degradation in 3D, we can calculate the ratio of the concentration at $r = R$, $c(R) \equiv c_1(R) = c_2(R)$, for non-zero β_2 and for $\beta_2 = 0$:

$$\frac{c(R)}{c_{free}(R)} = \frac{1}{\alpha_2 R}\frac{k_0(\alpha_2 R)}{k_1(\alpha_2 R)} \tag{2.15}$$

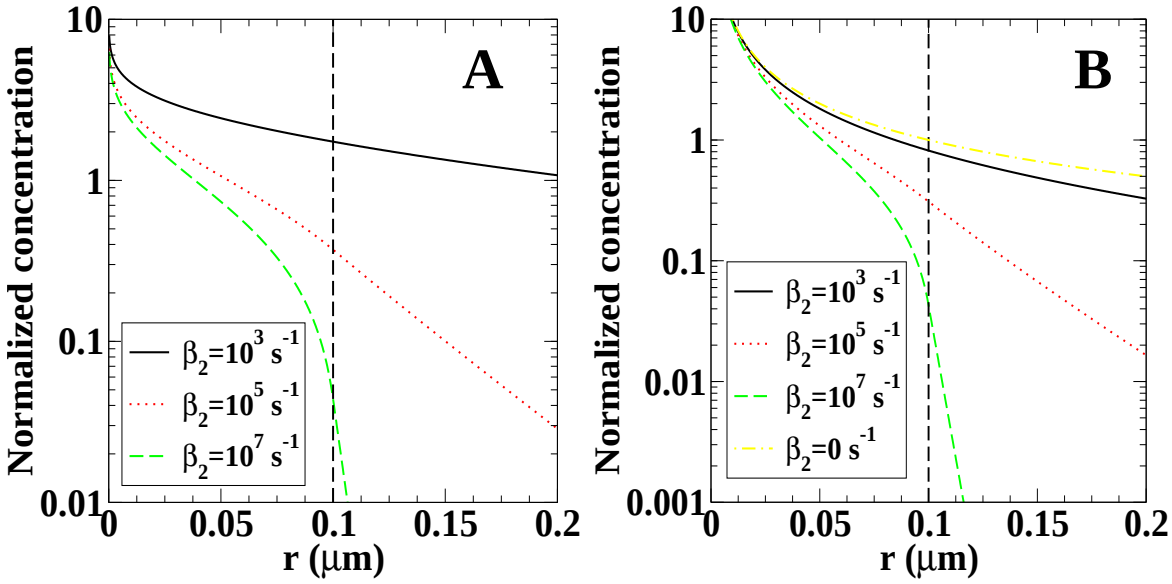

Figure 2.2: Results for $R_2 \to \infty$. The concentration as a function of the distance from the source in 2D (A; normalized by $F/(\pi D)$) and in 3D (B; normalized by $F/(2\pi DR)$) for different values of the degradation constant. The compartment size is indicated by the dashed line and was chosen to be $R = 0.1\mu m$. For $r \leq R$ the degradation constant was set to zero while for $r > R$ it was chosen to be β_2.

For large values of $\alpha_2 R$ this becomes

$$\frac{c(R)}{c_{free}(R)} \sim \sqrt{\frac{D}{\beta_2}}\frac{1}{R} \tag{2.16}$$

This result shows that, as expected, the difference between free diffusion and diffusion in the presence of a high degradation region increases as the degradation constant is increased.

To further determine the effect of high degradation rates in the second compartment we compare the value of the concentration at $r = R$ to a threshold value ϵ. After all, the desired effect of the second region is to create a compartment in which the concentration of cAMP is high enough to activate downstream pathways while decreasing the concentration in the second compartment such that it is lower than this activation threshold. In the limit $\alpha_1 \to 0$, the expression for concentration at $r = R$ in 2D, $C(R) \equiv C_1(R) = C_2(R)$, simplifies to

$$C(R) \sim \frac{F}{\pi D} \frac{K_0(\alpha_2 R)}{\alpha_2 R K_1(\alpha_2 R)} \tag{2.17}$$

with an equivalent expression in 3D. The resulting threshold condition $C(R) \leq \epsilon$ can be further simplified in the limit of large degradation constants ($\alpha_2 R \geq 1$). Thus in 2D, we find a minimum value for the degradation constant

$$\beta_2 \quad \widetilde{>} \frac{F^2}{\pi^2 D \epsilon^2 R^2} \tag{2.18}$$

and as following, in 3D we obtain

$$\beta_2 \quad \widetilde{>} \frac{F^2}{4\pi^2 D \epsilon^2 R^4} \tag{2.19}$$

Of course, the expression in 3D is only valid if the concentration for the free diffusion case is above the threshold value. This sets a constraint on the flux, which has to be at least $F_{min} = 2\pi D R \epsilon$. Again, since its free diffusion case is divergent there is no equivalent constraint in 2D. The above expressions show the expected dependence on the system parameters. For example, for increasing flux one needs to increase the degradation constant. Also, a smaller compartment size requires a larger degradation constant.

To address possible transient effects, we have also obtained an analytical time-dependent two dimensional solution in the case of a instantaneous flux source in 2D (see Appendix A):

$$\lim_{r \to 0} r \frac{\partial C_1}{\partial r} = -\frac{F}{\pi D} \delta(t) \tag{2.20}$$

The solution can be found using the method of Laplace transforms and details are given in the Appendix A. The final expressions are given by

$$
\begin{aligned}
C_1(r,t) &= \frac{F}{\pi D}\left[\frac{1}{2t}\exp(-\frac{r^2}{4Dt}-\beta_1 t)+\right. \\
&\left. \sum_{j=1}^{n}\frac{N_1(x_j)}{N'(x_j)} I_0(rk_1(x_j))\exp(x_j t)-\mathcal{L}[F_1(r,s)]\exp(-\beta_2 t)\right] \\
C_2(r,t) &= \frac{F}{\pi D}(\sum_{j=1}^{n}\frac{K_0(r\sqrt{\frac{x_j+\beta_2}{D}})}{N'(x_j)}\exp(x_j t)-\mathcal{L}[F_2(r,s)]\exp(-\beta_2 t)) \quad (2.21)
\end{aligned}
$$

The first term in C_1 can be recognized as the free diffusion solution. The second term is a sum over all the zeroes x_j of a function N, given in the Appendix A, in the interval $(-\beta_2, \beta_1)$. The final term involves the Laplace transform of the function F_1, again given in the Appendix A. Likewise, the expression for C_2 contains a term which is a sum over the zeroes x_j of a function given in the Appendix A, along with a term which is the Laplace transform of F_2, which can be found in the Appendix.

It is possible to simplify the expression by expanding the Laplace transform for large values of t (see Appendix A). To examine the accuracy of this expansion we have plotted in Fig. 2.3A the normalized concentration at $r = R/2$ as a function of time following a sudden turning on of the flux F at $t = 0$. The red line represents the result using Eq. 2.21 without the Laplace transform and the green line shows the results with the first term in the expansion. As a comparison, the black line is the result of the full numerical solution. The figure shows that keeping only the first term in the expansion accurately captures the time dynamics, especially for larger times. In Fig. 2.3B we plot the concentration at $r = R$, assuming a source that releases a constant flux for 1 ms which should be well below the time of activation of AC. Importantly, the concentration in the compartment reaches steady state within 1 ms.

In three dimensions, finding an analytical solution for the dynamic case becomes more difficult. To obtain time-dependent solutions for this geometry we have numerically integrated our equations. Again, we find that the concentration reaches a steady state within 1 ms (data not shown). Taken together, these results demonstrate that to investigate cAMP microdomains in our simple model it is

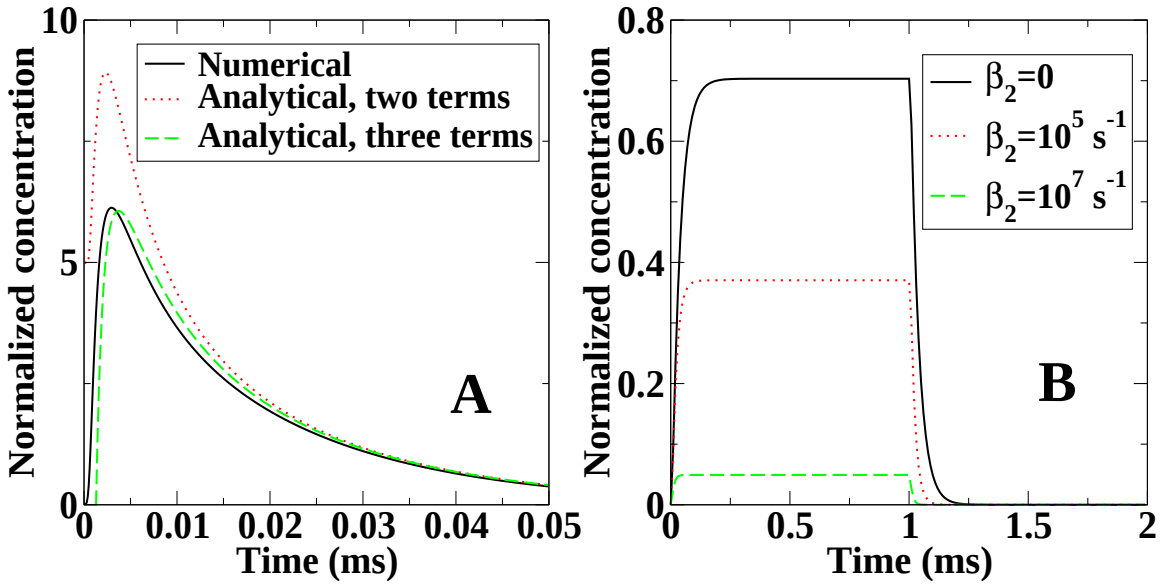

Figure 2.3: Time-dependent solutions for the concentration field for $R_2 \to \infty$ in 2D. (A) The concentration, normalized by $F/(\pi D)$, as a function of time at $r = R/2$ for $R = 0.1\mu m$. The flux was turned on at $t = 0$. Shown are the exact numerical solution (black line) and two approximative analytical solutions (see text). (B) The numerically obtained concentration at $r = R$, $R = 0.1\mu m$, as a function of time for different degradation constants β_2. The source was turned on at $t = 0$ and turned off at $t = 1ms$.

sufficient to examine the steady state response.

Finite R_2

From the above results, it becomes clear that the degradation rate in the second region needs to be large to ensure a small value of the second messenger concentration at its boundary. This degradation rate can be translated into a cellular PDE concentration when we assume Michaelis-Menten dynamics. If we use simple first order kinetics, we can approximate the degradation rate as

$$\beta = \frac{k_{cat}[PDE]}{K_m + [cAMP]} \tag{2.22}$$

where k_{cat} is the catalytic constant and K_m is the Michaelis-Menten constant. Experimental values for these constants are subject to considerable uncertainty. Nevertheless, if we use reported values ($k_{cat} = 5s^{-1}$ and $K_m = 1.3\mu M$, [19]), based on our model we can rewrite above equation as below (since the concentration beyond the boundary, c_2, is much lower than K_m)

$$\beta_2 = \frac{k_{cat}[PDE]}{K_m + c_2} \approx \frac{k_{cat}[PDE]}{K_m} \tag{2.23}$$

Hence, we find that for the degradation rates presented in Fig. 2.2B require PDE concentrations that are many orders of magnitude larger than K_m and much larger than reported values [19, 20]. Thus, our results suggest that using a a uniform high degradation zone is physiologically implausible.

Next, we examined the case of finite R_2 and take, for the sake of simplicity, $\beta_1 = \beta_3 = 0$. Results are shown in Fig. 2.4 where we plot the normalized concentration as a function of r in 3D for different values of R_2 and a fixed value of β_2 and R_1. From the figure we can see that the concentration profile within the high degradation compartment approaches the one corresponding to $R_2 \to \infty$ already for small values of $R_2 - R_1$. This can be understood by realizing that when the size of the high degradation zone is larger than the decay length, i.e. when

$$R_2 - R_1 > \sqrt{\frac{D}{\beta_2}} \tag{2.24}$$

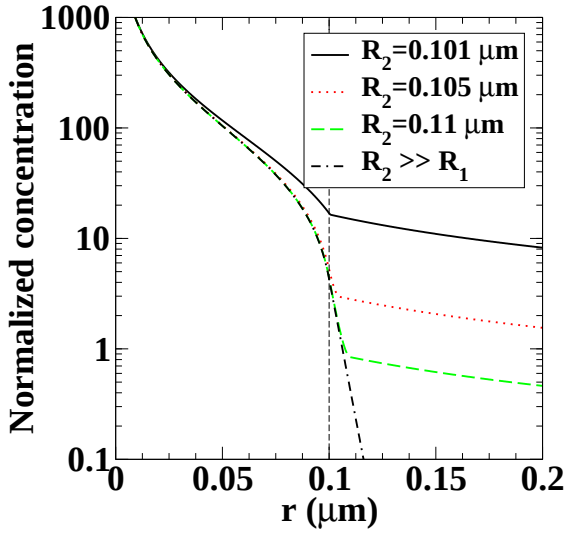

Figure 2.4: The 3D steady state concentration profile, normalized by $F/(2\pi DR_1)$, for a fixed value of $\beta_2 = 10^7 s^{-1}$ and for different values of R_2. The size of the first compartment is $R_1 = 0.1\mu m$.

the size of the region becomes irrelevant. For the parameter values used in Fig. 2.4 and for $D = 100\mu m^2/s$ we find that $\sqrt{\frac{D}{\beta_2}} \sim 0.003\mu m$.

To quantify the effect of the high degradation rate in the second compartment, we can again compare the steady state solution to a threshold value ϵ. In particular, we can determine for which parameter values $c_2(R_2)$ crosses this threshold. In the limit of large $\alpha_2 R_2$ we can again find a simple relationship between this threshold and the relevant system parameters. Apart from a numerical factor of order 1, and assuming that $(R_2 - R_1)/R_1 << 1$, these expressions are identical to the ones shown in Eqns. 2.18 and 2.19. It then becomes obvious that localizing the PDEs can, at the same time, produce a region with a large degradation constant while maintaining an overall PDE concentration that is physiologically plausible. In fact, we can estimate the ratio between the PDE concentration in high degradation area and the cellular PDE concentration. This ratio is simply the ratio of the total volume of spherical half shells and the cell volume:

$$\frac{[PDE](\text{finite } R_2)}{[PDE](R_2 \to \infty)} \sim N_{tot} \frac{2\pi R_1^2 (R_2 - R_1)}{V_{cell}} \tag{2.25}$$

where N_{tot} is the total number of separate sites emitting cAMP (*i.e.* the number of the spherical half shells). Taking a cell volume of $V_{cell} = 1.6 \times 10^4 \mu m^3$ [21] and using the parameter values of Fig. 2.4 with $R_2 - R_1 = 0.01 \mu m$ we get that this ratio is approximately $5 \times 10^{-8} N_{tot}$. Using the reported value of $\sim 10^5$ β-adrenergic receptors per cell [22] for N_{tot} we find that the cellular concentration of PDE can be several orders of magnitude smaller than the concentration within the high degradation compartment.

An accurate estimate of the required degradation constant is difficult without a precise knowledge of the involved parameters. Nevertheless, we can estimate its order of magnitude using a threshold value of $\epsilon = 0.1 \mu M$ [23]. Recalling the experiments that show that PDE inhibitors abolish microdomains [11], this threshold should be significantly lower that the value reached via pure diffusion. Hence, the flux should be larger than the aforementioned minimum value $F_{min} = 2\pi D R \epsilon$. For this value of the threshold, combined with a microdomain size of $R = 0.1 \mu m$ and a diffusion constant of $D = 100 \mu m^2/s$ we find a minimum 3D flux rate of at least $F_{min} \sim 4000 molecules/s$. Comparing this to the turn over rate of AC, which is estimated for the soluble form to be around $10 s^{-1}$ [24], we find, as in a previous modeling study [25], that the source needs to consist of multiple ACs. Of course, a significant reduction of the diffusion constant, as argued in a recent study [26], might alter this conclusion. Note also that if this source contains multiple receptors the ratio computed above (Eq. 2.25) will become even larger.

Assuming that the flux at our source is $F = 10000 molecules/s$, we find that for $R_2 \to \infty$ the minimum degradation rate is $\beta_2 \sim 10^4 s^{-1}$. With the previously quoted catalytic and Michaelis-Menten constants, this would require a local PDE concentration of roughly $2 \times 10^3 \mu M$. Clearly, the reduction in the required *cellular* PDE concentration by limiting the spatial extent of the PDEs is able to bring this number into the physiological range. Furthermore, this local concentration of PDEs translates to ~ 750 PDE molecules in a thin spherical shell of thickness $0.01 \mu m$. Assuming a single layer of PDEs, this would result in an inter-PDE spacing of approximately $0.01 \mu m$, equal to the thickness of the shell. Thus, we can conclude that our study demonstrates that the PDEs need to be localized in the

neighborhood of the cAMP sources to ensure a tight control of the spatial extent of the cAMP concentration.

Our approach has made a number of simplifications and is amenable to future extensions. For example, we have assumed simple Michaelis-Menten dynamics and have ignored potentially more complicated interactions between the second messenger and the PDE, including possible feedback loops. Such interactions will certainly alter the dynamics of cAMP but should be easy to implement, at least at the numerical level. Also, we have not explicitly modeled PKA activation, AC activation etc. [15, 16] but this can be incorporated easily. Finally, we have neglected the detailed structure of the cell by assuming a simple spherical symmetry. Going beyond this idealized geometry requires currently unavailable detailed anatomical knowledge of the location of the PDEs and the cell geometry. Incorporating these details in a numerical approach is, in principal, straightforward. We do not expect, however, that the main conclusion of this study, that PDEs need to be localized to ensure compartmentalization in cAMP signaling, will be changed by these extensions.

2.2 Compartmentalization of Second Messengers in Neurons: a Mathematical Analysis

2.2.1 Introduction

A large variety of cellular processes are regulated by the diffusible second messenger cyclic AMP (cAMP). This messenger is generated by membrane bound adenylyl cyclases (ACs) which, in turn, are activated by external signals. cAMP is degraded by phosphodiesterases (PDEs), which can be localized to specific cell locations or can be diffusible. The fact that cAMP is able to activate multiple pathways raises the question of signal specificity: how can one avoid the activation of undesirable pathways following the input to a specific pathway? One way to achieve signaling specificity is to have cAMP levels that are elevated in small spatial compartments but remain low in the rest of the cell. Indeed, an increasing number

of experiments had shown that there exist cAMP microdomains in several different cell types, including cardiac myocytes [27, 28], kidney cells [29] and neurons [30].

This compartmentalization is surprising since cAMP is a small, hydrophilic molecular, which diffuses very fast with a diffusion constant of $D = 100 \sim 700\mu m^2/s$. Thus, with no restriction on diffusion, AC activation will quickly lead to an increase in the global cAMP level. To prevent the indiscriminate activation of multiple pathways, there needs to be a mechanism that restricts the diffusion away from the microdomain. Possible mechanisms to create compartments with elevated levels of cAMP include physical barriers, including cell membranes and intercellular structures, and non-uniform degradation. An example of the latter mechanism was suggested for myocytes where physical barriers appear not to play a significant role. In this mechanism, cross-talk is avoided by co-localizing the final targets of the signaling pathway with the ACs, and by spatially separating the source of cAMP from regions with an elevated PDE concentration. In our previous work we constructed a mathematical model to investigate the viability of this mechanism. Using an analytical approach, we derived expressions for the steady state cAMP concentration field and found conditions for which this mechanism can lead to signal specificity [31].

Here, we will again examine second messenger compartmentalization using analytical techniques but will now focus on the cAMP concentration profiles in neurons. We are motivated by recent experiments in rat hippocampal slices [32] which demonstrated that, after stimulation, cAMP accumulates preferentially at the distal dendrites and that the soma maintains a low level of cAMP. Thus, sharp gradients of cAMP exist at the junction between the dendrites and the soma and it was suggested that the two domains with sharply different cAMP concentrations ensure signal specificity.

Using a simple representation of the cell geometry, we will present asymptotic analytical solutions that quantify how cell shape and degradation rates affect the spatial cAMP concentration profiles. This will be done both in 2d and 3d, the latter assuming axial symmetry; for ease of presentation we have placed the 3d results in an Appendix C. Our model does not consider downstream pathways,

such as protein kinase A (PKA), but is able to capture the salient ingredients required for second messenger compartmentalization. Our main result, in agreement with the numerical findings of Neves *et al.* [32], is that a sharp cAMP gradient between the soma and the dendrite requires a minimum level of signal degradation. Furthermore, we find that the cAMP gradient at the junction depends critically on the width of the dendrite.

2.2.2 Model

As in the numerical work of Neves *et al.* [32], we assume a neuron with the simplified geometry shown in Fig. 2.5. It consists of a circle with radius R, representing the cell body, and a protruding rectangle with length L and half width w, representing the dendrite. The 3d version, where the rectangle is replaced by a right circular cylinder, is presented in the Appendix C. Since the width of the dendrite is much smaller than the radius of the soma, *i.e.* $w \ll R$, we can approximate the connecting part of the circle and the rectangle to be a straight line. Thus, we have

$$w = R \sin\theta_0 \simeq R\theta_0. \tag{2.26}$$

where θ_0 is defined in Fig. 2.5. Note that the surface-to-volume ratio for the dendrite is much larger than for the soma.

For simplicity, we will assume that the PDEs are uniformly distributed in both the soma and the dendrite. Thus, the concentration in the circle, C_1, and in the rectangle, C_2, obey the diffusion equation with a homogeneous degradation rate β

$$\frac{\partial C_1(r,\theta,t)}{\partial t} = D\nabla^2 C_1 - \beta C_1, (0 \le r \le R, -\pi \le \theta \le \pi) \tag{2.27}$$

$$\frac{\partial C_2(x,y,t)}{\partial t} = D\nabla^2 C_2 - \beta C_2, (0 \le x \le L, -w \le y \le w) \tag{2.28}$$

where D is the diffusion constant of cAMP and where we have used a Cartesian coordinate system for the dendrite and a polar coordinate system for the soma.

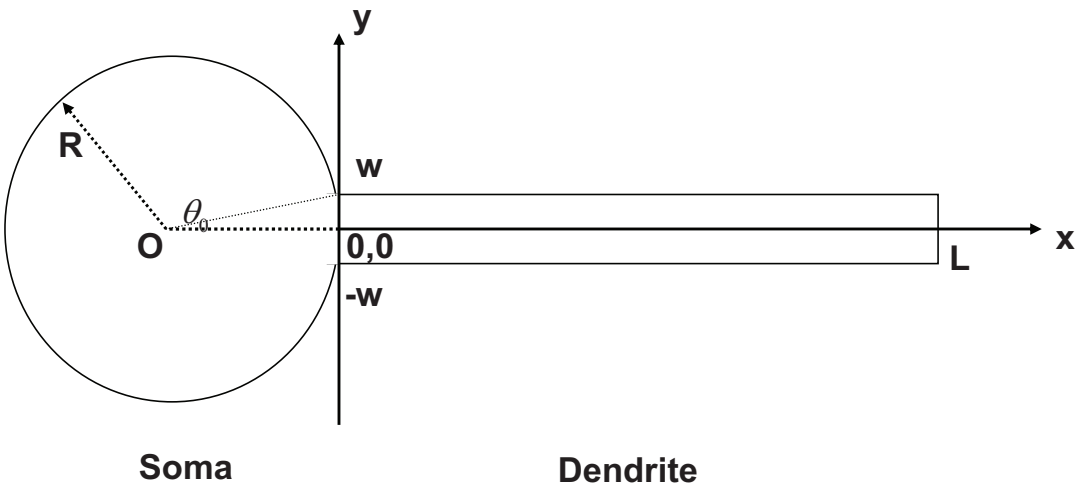

Figure 2.5: The circle with radius R represents the soma, and the rectangle with length L and half width w represents the dendrite. The sources for the second messengers are uniformly distributed on the perimeter, and the degradation molecules are uniformly distributed in both the soma and the dendrite.

It has been shown that the cAMP production machinery is distributed on both the soma and the dendrite membrane with little [33, 34] to no [35] observable spatial heterogeneity. Thus, it is reasonable to assume that the neuron has a constant cAMP source flux, f with unit $1/(s\mu m)$, on the entire membrane. Therefore, the boundary conditions on the various parts of the membrane read

$$\frac{\partial C_1(R,\theta,t)}{\partial r} = \frac{f}{D}, (\theta_0 \leq \theta \leq 2\pi - \theta_0) \tag{2.29}$$

$$\frac{\partial C_2(L,y,t)}{\partial x} = \frac{f}{D}, (-w \leq y \leq w) \tag{2.30}$$

$$\frac{\partial C_2(x,\pm w,t)}{\partial y} = \pm\frac{f}{D}, (0 \leq x \leq L). \tag{2.31}$$

We require that the concentration at the connection between the soma and the dendrite is continuous. Thus, under the condition that $w \ll R$, we have

$$C_1(R,\theta,t) = C_2(0,y,t), (-\theta_0 < \theta < \theta_0) \tag{2.32}$$

$$\frac{\partial C_1(R,\theta,t)}{\partial r} = \frac{\partial C_2(0,y,t)}{\partial x}, (-\theta_0 < \theta < \theta_0) \tag{2.33}$$

where $y \simeq R\theta$.

2.2.3 Results

We will focus here on steady state solutions which can be found by setting the left hand sides of Eqn. (2.27, 2.28) to zero. Then, a general steady state solutions for $C_1(r,\theta)$ and $C_2(x,y)$ can be obtained as

$$\begin{aligned} C_1(r,\theta) &= \sum_{m=0}^{\infty} B_m \frac{I_m(r/l)}{I'_m(R/l)} \cos m\theta \\ &+ \frac{f}{\sqrt{\beta D}} \frac{\pi-\theta_0}{\pi} \frac{I_0(r/l)}{I'_0(R/l)} \\ &- \sum_{n=1}^{\infty} \frac{2f}{\sqrt{\beta D}} \frac{\sin n\theta_0}{n\pi} \frac{I_n(r/l)}{I'_n(R/l)} \cos n\theta, \end{aligned} \tag{2.34}$$

$$\begin{aligned} C_2(x,y) &= \sum_{n=0}^{\infty} A_n [e^{x\sqrt{(\frac{1}{l})^2+(\frac{n\pi}{w})^2}} \\ &+ e^{(2L-x)\sqrt{(\frac{1}{l})^2+(\frac{n\pi}{w})^2}}] \cos(n\pi\frac{\theta}{\theta_0}) \\ &+ \frac{f}{\sqrt{\beta D}} \frac{\cosh(x/l)}{\sinh(L/l)} + \frac{f}{\sqrt{\beta D}} \frac{\cosh(y/l)}{\sinh(w/l)}, \end{aligned} \tag{2.35}$$

where $l = \sqrt{\frac{D}{\beta}}$ is a decay length. Here, and in the remainder of the paper, I_n represents the modified Bessel function of the first kind, and $'$ represents the derivative of the argument. The coefficients B_m are determined by A_n through Eqn.(2.33),

$$B_0 = \frac{l}{2\pi} \int_{-\theta_0}^{\theta_0} g(\theta) d\theta, \tag{2.36}$$

$$B_m = \frac{l}{\pi} \int_{-\theta_0}^{\theta_0} g(\theta) d\theta, m = 1, 2, 3, ... \tag{2.37}$$

where function $g(\theta)$ is the gradient at the connection of the circle and the rectangle, *i.e.* a function of A_n, for $-\theta_0 < \theta < \theta_0$

$$g(\theta) = \frac{\partial C_2(0,y)}{\partial x} = \sum_{n=0}^{\infty} A_n \sqrt{(\frac{1}{l})^2 + (\frac{n\pi}{w})^2}[1 - e^{2L\sqrt{(\frac{1}{l})^2+(\frac{n\pi}{w})^2}}] \cos(n\pi \frac{\theta}{\theta_0}). \quad (2.38)$$

To determine A_n, we can apply the continuity condition Eqn.(2.32) which results in a set of countable infinite linear equations for A_n: $MA = a$ where M and a are a matrix and column vector with infinite dimension determined by Eqn.(2.32), respectively, and where A is the vector $A_0, A_1, ...$

The resulting linear algebra problem is difficult to solve, even numerically. Fortunately, as we will see below, for thin dendrites the series converges rapidly and the first coefficient A_0 can be calculated in the limit $w = \theta_0 \to 0$. Let us use $c_{1,2}$ to represent the concentrations for this limiting case, which can be related to $C_{1,2}$ respectively, as follows

$$c_1(r,\theta) = \lim_{\theta_0 \to 0} C_1(r,\theta), \quad (2.39)$$

$$c_2(x) = \lim_{w \to 0} \int_{-w}^{w} C_2(x,y)dy. \quad (2.40)$$

The diffusion equation and boundary condition for c_1 are identical to Eqn.(2.27) and Eqn.(2.29) while the diffusion equation for c_2 becomes one dimensional:

$$0 = D\frac{d^2c_2}{dx^2} - \beta c_2 + 2f, \quad (2.41)$$

with as boundary condition

$$\frac{dc_2(L)}{dx} = \lim_{w \to 0} \int_{-w}^{w} \frac{f}{D} dw = 0. \quad (2.42)$$

The continuity equation Eqn.(2.32, 2.33) at the junction of the dendrite and the soma reduces to

$$c_2(0) = \lim_{\theta_0 \to 0} \int_{-\theta_0}^{\theta_0} R c_1(R,\theta) d\theta = 0, \tag{2.43}$$

$$\frac{\partial c_1(R)}{\partial r} = \frac{f}{D} + \frac{J}{DR}\delta(\theta), \tag{2.44}$$

$$\frac{dc_2(0)}{dx} = \frac{J}{D}, \tag{2.45}$$

where J denotes the flux from the dendrite to the soma with units $1/s$. The proof of the last identity in Eqn.(2.43) is given in Appendix B. $c_2(0) = 0$ reflects the fact that in this extreme case, molecules at the junction flow into the soma and never flow back to the dendrite. Solving the above equations leads to an analytic expression

$$J = 2fl\tanh(L/l), \tag{2.46}$$

$$\begin{aligned} c_1(r,\theta) &= \frac{f}{\sqrt{\beta D}} \frac{I_0(r/l)}{I_0'(R/l)} + \frac{f}{\beta R}\frac{\tanh(L/l)}{\pi}\frac{I_0(r/l)}{I_0'(R/l)} \\ &+ \frac{2f}{\beta R}\frac{\tanh(L/l)}{\pi}\sum_{n=1}^{\infty}\frac{I_n(r/l)}{I_n'(R/l)}\cos n\theta, \end{aligned} \tag{2.47}$$

$$c_2(x) = \frac{2f}{\beta} - \frac{2f}{\beta}\frac{e^{x/l}}{1+e^{2L/l}} - \frac{2f}{\beta}\frac{e^{(2L-x)/l}}{1+e^{2L/l}}. \tag{2.48}$$

Comparing the coefficients of $c_{1,2}$ and $C_{1,2}$ through Eqn.(2.39, 2.40), we find

$$A_0 = -\frac{f}{\beta w}\frac{1}{1+e^{2L/l}}, \tag{2.49}$$

$$B_0 = \frac{f}{\beta R}\frac{\tanh(L/l)}{\pi} + o(w), \tag{2.50}$$

$$B_m = \frac{2f}{\beta R}\frac{\tanh(L/l)}{\pi} + o(w), m = 1,2,3,... \tag{2.51}$$

Therefore, we can obtain an approximate form of the concentration in the soma

$$
\begin{aligned}
C_1(r,\theta) &= \sum_{n=1}^{\infty} \frac{2f}{\beta R} \frac{\tanh(L/l)}{\pi} \frac{I_n(r/l)}{I_n'(R/l)} \cos n\theta \\
&- \sum_{n=1}^{\infty} \frac{2f}{\sqrt{\beta D}} \frac{\sin n\theta_0}{n\pi} \frac{I_n(r/l)}{I_n'(R/l)} \cos n\theta \\
&+ \frac{f}{\beta R} \frac{\tanh(L/l)}{\pi} \frac{I_0(r/l)}{I_0'(R/l)} \\
&+ \frac{f}{\sqrt{\beta D}} \frac{\pi - \theta_0}{\pi} \frac{I_0(r/l)}{I_0'(R/l)} + o(w), \qquad (2.52)
\end{aligned}
$$

and in the dendrite

$$
\begin{aligned}
C_2(x,0) &= \frac{f}{\sqrt{\beta D}} \frac{\cosh(x/l)}{\sinh(L/l)} + \frac{f}{\sqrt{\beta D}} \frac{1}{\sinh(w/l)} \\
&- \frac{f}{\beta w} \frac{\cosh((L-x)/l)}{\cosh(L/l)} + o(\frac{1}{w}). \qquad (2.53)
\end{aligned}
$$

Furthermore the gradient at the junction reads in this limit

$$
\frac{\partial C_2(0,0)}{\partial x} = \frac{f}{w\sqrt{\beta D}} \tanh(L/l) + o(\frac{1}{w}). \qquad (2.54)
$$

In Fig. 2.6 we plot the approximate solution in the dendrite as a function x (solid line), along with the full solution obtained by numerically solving the model (dotted line) for two different dendrite widths. As we can see, the approximate concentration is quite close to the numerical solution away from the soma but starts to deviate closer to the soma. The analytical solution is a function of w, of course, and approaches the numerical solution as w get smaller. This is also demonstrated in Fig. 2.7A where we plot the gradient at the junction of the the soma and the dendrite for both the full solution (circles) and our analytical approximation (solid line). Clearly, the error between the two results, plotted in Fig. 2.7B, becomes smaller as the width of the dendrite decreases, consistent with the expectation that the analytical solution converges to the full solution as $w \to 0$. We note here that our results can be extended to three dimensions as shown in Appendix C.

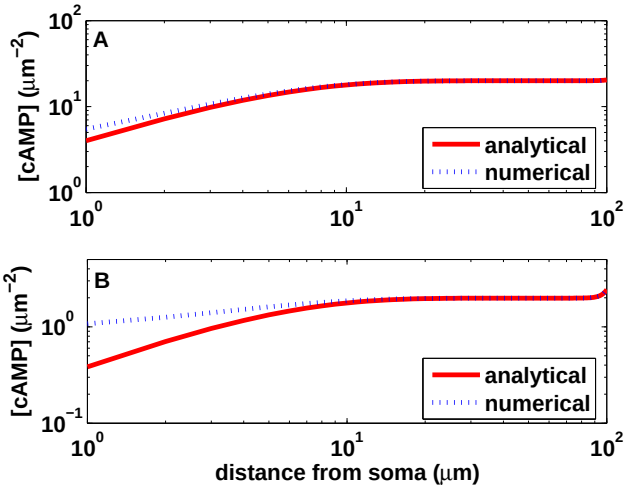

Figure 2.6: (Color online) A comparison between the analytical approximation (solid line) and the numerical result (dotted line) for the cAMP concentration in the dendrite along the symmetry line for $w = 0.1\mu m$ (A) and $w = 1\mu m$ (B). Other parameters used are $R = 10\mu m, L = 100\mu m, f = 20s^{-1}, D = 200\mu m^2/s, \beta = 10s^{-1}$.

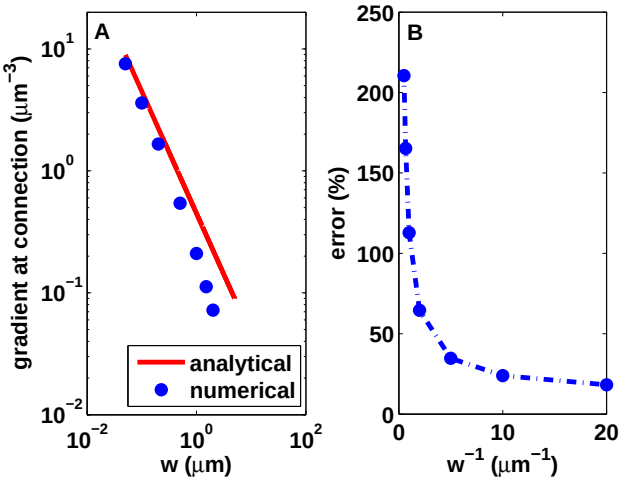

Figure 2.7: (Color online) A: A comparison between the analytical approximation (solid line) and the numerical result (circles) for the gradient at soma-dendrite junction as a function of w. B: The corresponding error as a function of w^{-1}. Other parameters used are $R = 10\mu m, L = 100\mu m, f = 20s^{-1}, D = 200\mu m^2/s, \beta = 10s^{-1}$.

2.2.4 Discussion

The main advantage of having analytical expressions for the concentrations in the two compartments and the concentration gradient at the junction is that it becomes easier to assess the effect of the system parameters on compartmentalization. From Eq. 2.52 we see that the concentration at the center of the soma can be approximated by

$$C_1(0,0) \simeq \frac{f}{I_0'(R/l)} \left(\frac{\tanh(L/l)}{\beta \pi R} + \frac{1}{\sqrt{\beta D}} \right) \tag{2.55}$$

Upon inspection of this equation, we can conclude that the cAMP concentration in the soma is largely independent of the length of the dendrite provided that this length is much larger that the decay length l. Furthermore, the concentration is independent of the width of the dendrite and thus, for small w and $L >> l$, the soma concentration depends only weakly on the geometry of the dendrite and is mostly determined by the degradation rate β.

A similar analysis can be carried out for the concentration in the middle of the dendrite ($x = L/2$), where we find from Eq.(2.53)

$$C_2(L/2,0) \simeq \frac{f}{\beta w} \left(1 - \frac{\cosh(L/(2l))}{\cosh(L/l)} \right) + \frac{f}{\sqrt{\beta D}} \frac{\cosh(L/(2l))}{\sinh(L/l)} \tag{2.56}$$

Thus, the cAMP level in dendrite decreases as the degradation rate increases but is also strongly dependent on the width of the dendrite. We note that for $L >> l$ the concentration reduces to the simple form $C_2(L/2,0) \simeq \frac{f}{\beta w}$. We can also conclude that the largest gradient of cAMP occurs at the junction between the soma and the dendrite and Eq.(2.54) shows that this gradient is inversely proportional to w and to the square root of the diffusion constant and the degradation rate. It also shows that the radius of cell body has no effect on the gradient. In fact, for $L >> l$ the gradient becomes independent of the length of the dendrite and the only geometric dependence is through the width: $\frac{\partial C_2(0,0)}{\partial x} \simeq \frac{f}{w\sqrt{\beta D}}$.

Finally, we have performed numerical simulations, using MATLAB's PDE Toolbox, to confirm the role of degradation and geometry on the concentration fields in the soma and dendrite. Fig. 2.8 shows the cAMP concentration in a

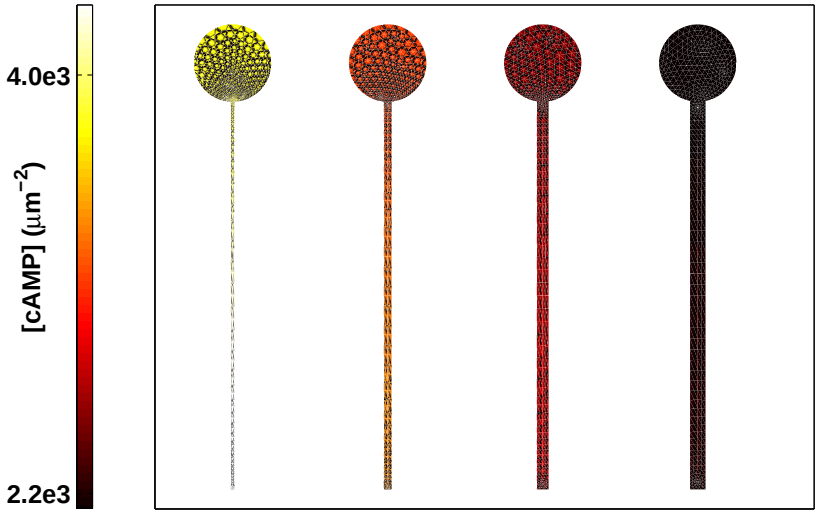

Figure 2.8: (Color online) Numerical results without degradation mechanism for different widths of the dendrite $w = 0.5, 1.0, 1.5, 2.0\mu m$ (from left to right respectively). The radius of the soma was taken to be $R = 10\mu m$ and the length of the dendrite was chosen to be $L = 100\mu m$. Other parameters are $f = 20s^{-1}, D = 200\mu m^2/s, T = 300s$.

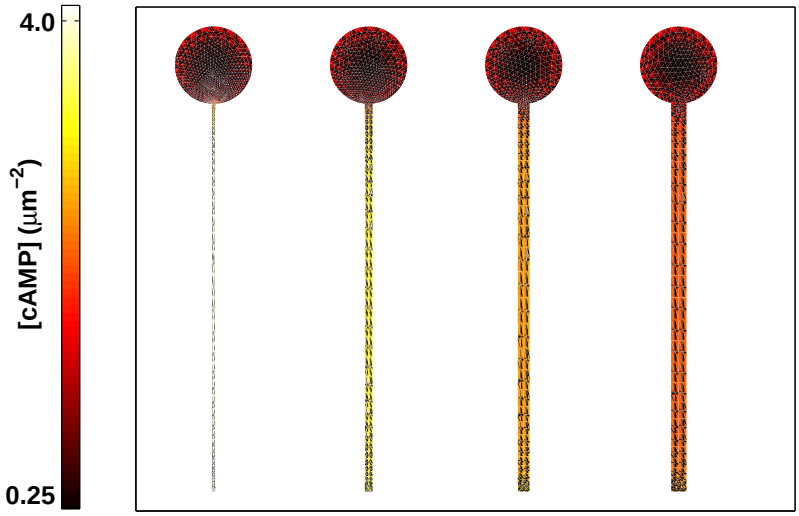

Figure 2.9: (Color online) Numerical results with degradation rate $\beta = 10s^{-1}$ for different widths of the dendrite $w = 0.5, 1.0, 1.5, 2.0\mu m$ (from left to right respectively). Parameter values are as in Fig. 2.8.

color scale in the absence of degradation ($\beta = 0$) using $C_1(r, \theta) = C_2(x, y) = 0$ as initial condition. Clearly, this is an unrealistic situation as the concentration would increase indefinitely as long as the flux is constant. Nevertheless, we can investigate the dependence of the cAMP fields in the two compartments by plotting the concentration at a particular time. This is done in Fig. 2.8 for 4 different values of w and $T = 300s$. We can see that the concentration in the dendrite increases significantly if the width becomes smaller. However, in support of our analysis above, the concentration in the soma increases as well and the resulting high concentration in both the soma and the dendrite would make it difficult to achieve signal specificity. In Fig. 2.9 we show the steady state cAMP concentration for the same set of dendrite widths and a non-zero degradation constant. Again, the results are shown for $T = 300s$, chosen such that the concentration has reached a steady state, starting at the same initial condition as in Fig. 2.8. As is evident from the figures, the introduction of cAMP degradation is able to drastically reduce the concentration of cAMP in the soma while maintaining a high cAMP level in thin dendrites. The results also show that w has little effect on cAMP level in the soma, again verifying our analytic results above.

In summary, we have derived analytical solutions for the cAMP concentration field in a simplified neuronal geometry where the difference in surface-to-volume ratio between the soma and the dendrite, coupled with a constant cAMP flux, leads to compartmentalization [32]. We find that the expression become particularly easy to analyze in the limit of thin dendrites. Our solutions show that a sufficient level of degradation, along with a dendrite with a width that is much smaller that the radius of the soma, does lead cAMP compartmentalization and offers a mechanism for signal specificity.

2.3 Acknowledgements

This Chapter, in part, contains the published material as it appears in "A mathematical analysis of second messenger compartmentalization", Wen Chen, Herbert Levine, and Wouter-Jan Rappel, *Physical Biology*, **5**, 046006 (2008), and

"Compartmentalization of second messenger in neurons: A mathematical analysis", Wen Chen, Herbert Levine, and Wouter-Jan Rappel, *Phys. Rev. E*, **80**, 041901 (2009). The dissertation author was the primary investigator and author of these papers.

Chapter 3

Gradient Sensing

3.1 External and internal constraints on eukaryotic chemotaxis

3.1.1 Introduction

Chemotaxis, the chemically guided movement of cells, plays an important role in several biological processes including cancer, wound healing, and embryogenesis. Chemotacting cells are able to sense shallow chemical gradients where the concentration of chemoattractant differs by only a few percent from one side of the cell to the other, over a wide range of local concentrations. Exactly what limits the chemotactic ability of these cells is presently unclear. Here we determine the chemotactic response of Dictyostelium cells to exponential gradients of varying steepness and local concentration of the chemoattractant cAMP. We find that the cells are sensitive to the steepness of the gradient as well as to the local concentration. Using information theory techniques, we derive a formula for the mutual information between the input gradient and the spatial distribution of bound receptors and also compute the mutual information between the input gradient and the motility direction in the experiments. A comparison between these quantities reveals that for shallow gradients, in which the concentration difference between the back and the front of a 10-m-diameter cell is $< 5\%$, and for small local

concentrations ($< 10nM$) the intracellular information loss is insignificant. Thus, external fluctuations due to the finite number of receptors dominate and limit the chemotactic response. For steeper gradients and higher local concentrations, the intracellular information processing is suboptimal and results in a smaller mutual information between the input gradient and the motility direction than would have been predicted from the ligand-receptor binding process.

Chemotaxis, the motion of cells guided by chemical gradients, plays an important role in a variety of biological processes, including wound healing, embryogenesis, and cancer metastasis. The chemical gradients required for efficient chemotaxis can be very shallow for eukaryotic cells. For example, the rapidly crawling neutrophils of the mammalian immune system and the social amoebae, Dictyostelium discoideum [36]-[43], are able to sense shallow chemical gradients where the concentration of chemoattractant differs by only a few percent from one side of the cell to the other, over a wide range of local concentrations [44]-[46].

The chemotactic response of these cells can be considered as the outcome from two distinct steps: establishment of spatial differences in the distribution of receptors with bound chemoattractant on the cell's surface [47] and the response to these differences by the signal transduction pathways leading to directed motility [48]. The first step is subject to the external fluctuations in chemoattractant binding to the surface receptor. This external noise can be precisely characterized, either through direct numerical simulations [73, 50] or through approximate analytical calculations [95]-[53]. The second step involves a number of pathways that are subject to internal background noise generated by any of the components that drive the extension and retraction of pseudopods leading to cell movement. Furthermore, these pathways can operate in a nonlinear fashion that can reduce the amount of intracellular information transfer. The internal noise and the effect of the nonlinearity of the pathways are difficult to quantify. Multiple signaling pathways operating in parallel, each with a number of unknown components, determine the direction of movement. The quantification of noise necessitates knowledge about the number of involved molecules, their reaction rates, and their diffusion constants whereas quantifying the signal processing of the nonlinear pathways re-

quires a detailed and complete mechanistic motility model.

In this study, we investigate the chemotactic response of Dictyostelium cells in stable exponential chemoattractant gradients generated in microfluidics devices. Using these experimental data, we compute the mutual information between the external gradient direction and the motility direction, which is a measure of the information that these variables share [54]. We also calculate analytically the mutual information between the external gradient and the spatial distribution of bound receptors. A comparison of these two quantities allows us to evaluate when the chemotactic response is being limited by sensing noise (assuming that the directional motility response is indicative of the goal of the chemotactic process) or alternatively by suboptimal intracellular processing of the information from the bound receptors.

3.1.2 Results

Quantitative Experimental Studies of Chemotaxis

We performed quantitative experiments of developed Dictyostelium cells in exponential cAMP gradients, using microfluidic devices. Within these devices, we can define a difference of the concentration between the front and the back of the cells, ΔC, along with the local concentration experienced by the cell, C_{local}. The choice of an exponential gradient ensures that the proportional concentration difference, i.e., the ratio $\Delta C/C_{local}$, is independent of the position in the device. Furthermore, the fluid flow within the microfluidic devices guarantees that signaling between cells can be neglected. An example of an exponential gradient in the microfluidic devices using a fluorescent dye is shown in Fig. 3.1A.

We examined the chemotactic response as a function of the two gradient parameters: C_{local} and the gradient steepness, p, which can be expressed as the percentage of difference in concentration between the front and the back. We used devices that generated gradients of different steepnesses, ranging from a 1.25 to a 10% difference in concentration across a cell with a diameter of $L = 10\mu m$, and tracked the paths of cells over a period of 8 min. The chemotactic index (CI) was calculated as the ratio of the distance covered in the direction of the gradient

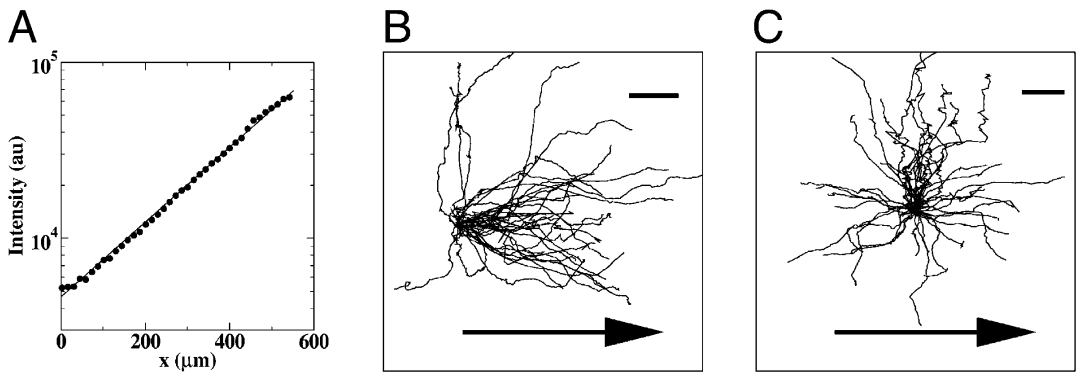

Figure 3.1: The chemotactic response of cells in exponential gradients depends on the gradient steepness. (A) The concentration as a function of the position along the gradient direction in the microfluidic device. The exponential gradient spans a $550 - \mu m - wide$ region and the concentration can be described by , where $L = 10\mu m$ and p is a measure of the steepness of the gradient. The steepness is expressed as the fractional difference in the concentration across 10 m and measures 5% for the data shown. (B and C) Typical cell tracks, with their origins brought to a common point, are shown for a steep (10%) gradient (B) where the concentration within the microfluidic device varies between 1 and 256 nM and for a shallow (1.25%) gradient (C) where the concentration spans values between 1 and 2 nM. The arrow indicates the direction of the gradient. (Scale bars: $20\mu m$.)

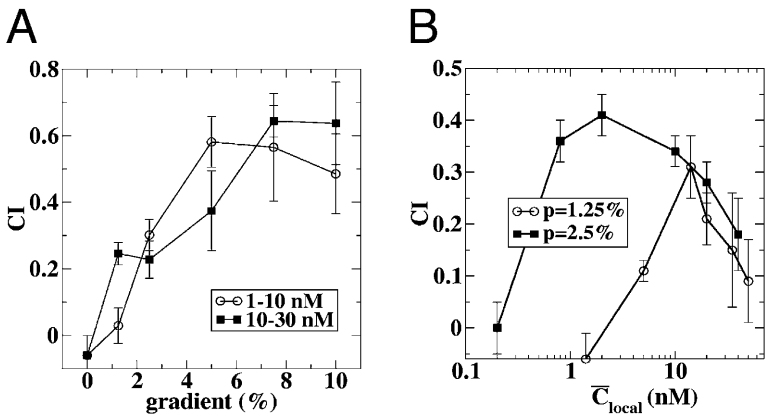

Figure 3.2: Dependence of the chemotactic index, CI, on the gradient steepness and the local concentration. (A) Mean value of the CI as a function of the gradient steepness for cell migration trajectories with an average local concentration between 1nM and 10nM and between 10nM and 30nM. (B) The CI as a function of the local concentration for two different values of the gradient steepness. Each data point is an average value for cells exposed to local concentrations in a twofold (for $p = 1.25\%$) or fourfold (for $p = 2.5\%$) range, with the plotted value of $\overline{C}_{local} \sim 15nM$ corresponding to the geometric mean of the range. In both figures, the error bars represent the standard error of the mean.

and the total distance traveled. Cell tracks in a representative steep and shallow gradient are shown in Fig. 3.1 B and C. In the steep gradient (10%, Fig. 3.1B), most cells move in the direction of the gradient and the CI for this experiment was 0.56. On the other hand, in the shallow gradient (1.25%, Fig. 3.1C) there was no detectable directional bias, resulting in a CI that is indistinguishable from 0.

The chemotactic response was determined in devices that generated gradients with five different steepnesses (Fig. 3.2A). Cells that were exposed to an average local concentration in a 1- to 10-nM range are shown as circles whereas cells with an average local concentration within 10C30 nM are plotted as squares. For the 1- to 10-nM concentration range, the cells failed to recognize the shallowest gradient (1.25%) but responded with increasingly accurate directionality to the steeper gradients (2.5C10%) with a maximum CI that is consistent with previous reports [55].

To investigate the effect of the local concentration on the CI we systematically varied the concentration range in a 1.25% and a 2.5% exponential gradient

and report the CI as a function of the geometric mean of the minimal and maximal local concentration within the microfluidic device $\overline{C}_{local}$ (Fig. 3.2B). For a 1.25% gradient, the CI increases for increasing average local concentration, reaches a maximum around $C_{local}(x) = C(0)e^{xp/L}$, and decreases upon further increasing the local concentration. The dependence of the CI on the local concentration in a 2.5% gradient is qualitatively similar but peaks at a smaller local concentration. Thus, our experiments indicate that the maximum CI is reached well below the reported value for the receptor dissociation constant $K_d = 30nM$ [56].

Analysis Using Information Theoretic Techniques

To quantify the fluctuations originating from the external binding process we first computed the mutual information [57] between the external chemoattractant gradient direction θ_s and the resulting spatial distributions of bound receptors Y. This mutual information is a measure of how much the uncertainty in Y is reduced by the knowledge of θ_s. It is typically expressed in units of bits and is always ≥ 0: A mutual information equal to 0 implies that knowing the external gradient direction does not reduce the uncertainty in the spatial distribution of bound receptors.

We considered a circular two-dimensional cell, divided the cell membrane into n segments containing an equal number of N/n receptors, where N is the total number of receptors, and considered simple first-order ligandCreceptor kinetics. An exact formula for this external mutual information $I(Y;\theta_s)$ for a single measurement is derived in Appendix D and for shallow gradients this reduces to

$$I(Y;\theta_s) \approx \frac{NK_dC_{local}p^2}{16\ln(2)(K_d + C_{local})^2} \tag{3.1}$$

where K_d is the dissociation constant of the ligandCreceptor binding process. Thus, the external mutual information has a maximum at a local concentration equal to K_d and the value of this maximum depends only on the number of receptors and on the gradient steepness. Our choice of equal numbers of receptors per segment was motivated by experimental data that show a homogeneous spatial

distribution of receptors on the membrane [58, 59]. The case of randomly placed receptors, leading to a variable number of receptors in each segment, is analyzed in Appendix D. We found that the mutual information in this case is almost identical to the mutual information found using Eq. 3.1. In Appendix D we also discuss the mutual information for elliptical cells and show that the mutual information can increase only by a modest amount ($\sim 20\%$) for highly elongated cells.

To determine how much additional information is lost in the internal processing steps, we computed the mutual information $I(\theta_r;\theta_s)$ between the gradient direction θ_s and the motility direction θ_r. This mutual information determines how much information an observer of the cell motion has about the gradient direction and takes into account both the external and the internal steps. It follows from the data processing inequality that it can be at most equal to the external mutual information. We determined, for each experiment, the instantaneous response angle θ_r for all cell tracks. Next, we divided the 360° range of θ_r in m bins and computed the fraction of angles falling within each bin, N_j. The choice of the number of bins was optimized using a procedure that minimizes a cost function that is a measure of the error introduced by binning the data [60] (Appendix D). The resulting histogram of θ_r using the optimal bin size is shown in Fig. 3.3A for a 10% gradient. Then, the external and internal mutual information was calculated as

$$I(\theta_r;\theta_s) = \sum_{j=1}^{m} N_j \log N_j + \log m \tag{3.2}$$

In Fig. 3.3B we show this mutual information as a function of the gradient steepness, along with the numerically determined external mutual information, and in Fig. 3.3C we show these quantities as a function of for a gradient of 2.5%. The error bars in the external and internal mutual information are due to the finite number of data points and the range of local concentrations to which the cells are exposed.

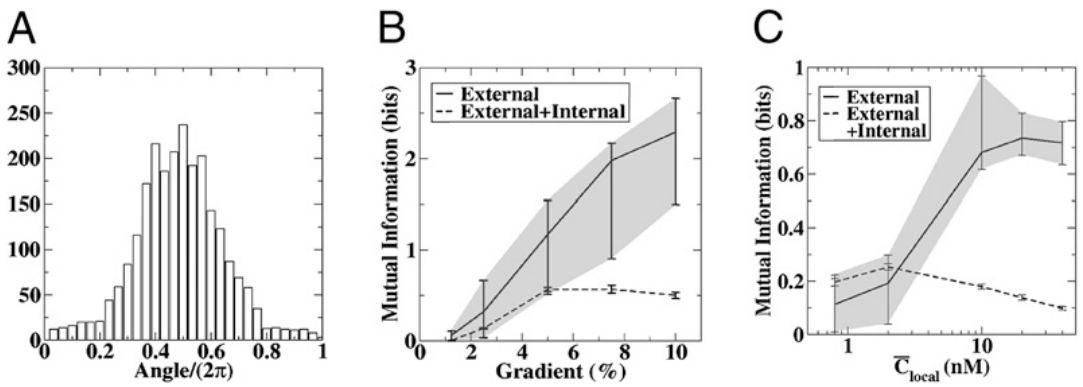

Figure 3.3: Dependence of the mutual information (MI) on the gradient parameters. (A) Histogram of the instantaneous response angle θ_r for the cell tracks in a 10% gradient, showing a pronounced peak at $\theta_r = \pi$, the gradient direction. (B and C) The external and internal MI between the input gradient angle, θ_s, and θ_r calculated using the experimental data (dashed lines), and the external MI between θ_s and the spatial distribution of bound receptors Y, calculated numerically (solid lines), as a function of the gradient steepness for cells with an average local concentration between 1 and 10nM (B) and as a function of the mean local concentration for a 2.5% gradient (C). Parameters used for the computation of the external MI are $N = 70,000$ and $K_d = 30nM$.

3.1.3 Discussion

Recently, the role of fluctuations in chemotaxis has received significant attention [50, 95, 53, 55, 61, 62]. Most studies, however, were either purely theoretical or performed under conditions that were difficult to quantify. Our approach, which uses exponential gradients generated in microfluidic devices, has several benefits. It allows us to precisely quantify the gradient presented to the cells, because the exponential profile ensures that the fractional concentration difference is independent of the position in the device. Moreover, the fluid flow abolishes any potential cell-to-cell signaling. The main parameters that determine the gradient (the steepness and the local concentration) can be controlled in each device, allowing us to fix one and vary the other.

Our experiments in which the local concentration was restricted to a narrow range show that the CI increases for increasing gradient steepness (Fig 3.2A). These results are in agreement with recent theoretical investigations of the directional sensing process that predict a sigmoidal dependence of the CI on the gradient steepness [95, 62]. Our results also indicate that the minimum gradient steepness required for a directional response depends on the local concentration: Cells exposed to a 1.25% gradient do not respond directionally in a 1- to 10-nM concentration range but do respond in a 10- to 30-nM concentration range. Hence, chemotaxis is controlled by both the gradient steepness and the local concentration. This is further illustrated when we keep the gradient steepness constant and vary the local concentration (Fig. 3.2B). The dependence of the CI on the local concentration in both a 1.25% and a 2.5% gradient is qualitatively similar. However, the CI in the 2.5% gradient peaks at a smaller local concentration. Thus, our experiments indicate that the maximum CI is reached well below the reported value for the receptor dissociation constant $K_d = 30nM$ [56].

To characterize the fluctuations originating from the external binding process we computed the mutual information between the external chemoattractant gradient direction s and the resulting spatial distributions of bound receptors Y. The result shows that this external mutual information has a maximum when the local concentration equals K_d. A similar result was also found from a signal-to-

noise analysis [50]. In other words, purely on the basis of spatial distribution of bound receptors, chemotaxing cells would perform ideally when the local concentration is equal to the dissociation constant. The optimal local concentration for neutrophils in an exponential gradient was also determined to be $\sim K_d$ [45] whereas an analysis in which receptors are randomly distributed can reduce the optimal concentration by at most 50% [61]. Thus, our experiments, combined with this theoretical analysis, suggest that the processing of the gradient cues inside cells reduces the optimal local concentration for chemotaxis and that this optimal concentration is determined through a convolution of the external (i.e., receptor binding and unbinding) and internal steps [62].

This conclusion is unchanged when one takes into account that Eq. 3.1 is valid for a single snapshot measurement and needs to be modified to include multiple independent measurements of the receptor binding distribution. A typical correlation time for this distribution can be calculated [50] using experimentally measured off rates [47] and is ~ 5 s, which is comparable to the pseudopod lifetime. In Appendix D, we show that this leads to an estimated prefactor of order 1.

For shallow gradients ($< 5\%$) we find that the external mutual information is comparable to the mutual information for the entire chemotactic process (Fig. 3.3B). This observation means that the information lost in intracellular signal pathways is negligible and that the intracellular information processing is near optimal. In other words, the receptorCligand binding noise dominates the chemotactic process and determines the precision of the cells in shallow gradients. Implicit in reaching this conclusion is the assumption that the chemotactic process is evolutionarily designed to allow the cells to track the gradient direction as accurately as possible. For steeper gradients, on the other hand, the amount of information lost due to internal fluctuations is significant and can be as high as 1.5 bits. A comparison between the two mutual information for a fixed gradient (Fig. 3.3C) reveals that they are comparable for small local concentrations. For large ($> 10nM$) concentrations, however, the external mutual information is much larger than the external and internal mutual information. Thus, we conclude that for steep gradients and for high local concentrations the intracellular information

processing is suboptimal and that intracellular pathways leading from the receptor to the establishment of a leading edge determine the chemotactic limits. For shallow gradients and low local concentrations, on the other hand, the receptorCligand fluctuations limit the chemotactic efficiency.

A possible interpretation of our results comes from realizing that the optimal local concentration for the receptorCligand process is at K_d. This interpretation suggests that the intracellular signaling networks have an optimal concentration well below this value. Increasing the steepness of the gradient increases the difference in the number of bound receptors between the front and the back of the cell. This could enlarge the relative contribution of the internal pathways, shifting the optimal local concentration to smaller values. The mechanisms behind the observed intracellular information loss are unclear. One possibility is that intracellular fluctuations become larger and limit the information transfer. Another possibility is that the signaling pathways are nonlinear and saturate for steep gradients and large concentrations, leading to a reduction in transfer of information. The latter possibility can be studied using existing models for directional sensing [50] and is currently under investigation.

3.2 Estimation Theory of Eukaryotic Gradient Sensing

3.2.1 Introduction

The response in biological systems to external stimuli is often limited by the inherent stochasticity of these stimuli. For example, the accuracy of human (and other vertebrate) vision at low light intensities approaches a fundamental limit set by statistical fluctuations of the number of absorbed photons [66, 67]. Another example is the embryo patterning along the anterior-posterior axis of the fruit fly *Drosophila melanogaster*, determined by concentration profiles of certain morphogens. The accuracy of the resulting pattern is limited by the noise levels in these gene expression profiles. A final example is provided by chemotaxis, the

directed movements of cells up or down a chemical gradient. In either prokaryotic chemotaxis, where cells measure and compare concentration signals over time [68, 69], or eukaryotic chemotaxis, where cells measure concentration differences in space [70, 40], the precision of gradient sensing is limited by the stochastic binding of diffusing chemical molecules (ligands) to specific chemoreceptors on the cell membrane.

These examples highlight the crucial role noise has on the capacities of biological signaling systems and point to the central question concerning the reliability of cells to detect environmental stimuli based on their noisy measurements. To address this question, we will use estimation theory which attempts to estimate the values of parameters based on measured data that contain a random component. The parameters represents an underlying physical setting in such a way that the value of the parameters affects the distribution of the measured data. An estimator takes the measured data as input and attempts to approximate the unknown parameters using the measurements. In order to find a desired estimator, it is first necessary to determine a probability distribution for the measured data, and the distribution's dependence on the unknown parameters of interest. After deciding upon a probabilistic model, it is helpful to find the limitations placed upon an estimator. This limitation, for example, can be found through the Cramér-Rao bound.

In this paper, we apply techniques from estimation theory to study eukaryotic gradient sensing and use the social amoeba *Dictyostelium discoideum* as our model system. Specific G-protein coupled receptors on the *Dictyostelium* cell membrane bind and detect the chemoattractants in the surrounding medium. This results in an asymmetric distribution of ligand-occupied receptors, which further activates multiple second-messenger pathways inside the cell and drive the extension of pseudopods preferentially in the direction of the chemoattractant gradient. Due to fluctuations in the ligand binding to chemoreceptors, the receptor signal is inherently noisy, as demonstrated by recent single-molecule imaging experiment [47]. Surprisingly, *Dictyostelium* cells exhibit extremely high sensitivity to gradients, as they are able to sense a $\sim 1\%$ difference in chemical concentration across

the cell length [44, 71]. The difference in receptor occupancy between the front and back halves of a cell in these shallow gradients can be calculated to be 10-30. This raises a puzzle about eukaryotic chemotaxis: how can cells reliably acquire the gradient information from such a noisy receptor signal?

In 1977, Berg and Purcell analyzed the bacterial (e.g., *E. coli*) chemotaxis and demonstrated that the limit uncertainty of concentration sensing is set by the diffusion of ligand particles [86]. Their seminal work has been extended by many others [53, 72, 73, 95, 74]. The results of Berg and Purcell, however, do not completely carry over to eukaryotic cells, which employ a spatial sensing mechanism. In this mechanism, and in contrast to prokaryotic chemotaxis, cells use the spatial asymmetry (including the gradient steepness and direction) to direct their motion. A number of studies have been carried out to reveal the limits to spatial gradient sensing, but are either applicable to idealized mechanisms that ignore the receptor kinetics [95] or are based on heuristic signaling models [50, 62]. We recently addressed this problem for circular cells using a general statistical mechanical approach, where we view the surface receptors as a (possibly coupled) spin chain and treat the chemical gradient as a perturbation field [75]. By calculating the system's partition function, we were able to derive the gradient sensing limits for either independent receptors or receptors exhibiting cooperativity. In this paper, we will first revisit the spatial gradient sensing problem for circular cell shapes using purely estimation-theoretic methods. This will be the foundation for our extension to the elliptical cell shapes in the next section. Finally, we will examine how the intracellular bias can affect the perceived gradient and compare our results with recent experimental data.

3.2.2 Gradient sensing for a circular cell

We revisit the gradient sensing problem which we have examined in our previous paper [75]. But here we directly use the method of *maximum likelihood estimate* (MLE) [76]. Consider a circular cell with diameter L placed in a chemoattractant gradient and assume that there are N receptors uniformly distributed on the cell perimeter. The angular coordinates of these receptors are denoted by φ_n

for $n = 1, ..., N$, which all satisfy the uniform distribution $P(\varphi_n) = 1/(2\pi)$. We further assume that the gradient field takes an exponential profile as has recently been realized in experiments [71, 96]. Then the local concentration at the n-th receptor can be expressed as $C_n = C_0 \exp\left[\frac{p}{2}\cos(\varphi_n - \phi)\right]$, where C_0 is the ambient (mean) concentration, $p \equiv \frac{L}{C_0}|\vec{\nabla}C|$ defines the gradient steepness that quantifies the percentage concentration change across the cell length L, and ϕ denotes the gradient direction. Each receptor switches independently between two states, either empty (0) or occupied (1), with transition rates determined by the local concentration and the relevant chemical kinetics. Therefore, these receptors in a single snapshot constitute a series of independent Bernoulli random variables, represented by

$$x_n = \begin{cases} 1, & \text{with probability} \quad P_n, \\ 0, & \text{with probability} \quad 1 - P_n, \end{cases} \tag{3.3}$$

for $n = 1, ..., N$. For simple ligand-receptor kinetics, the occupancy probability of the n_{th} receptor is $P_n = C_n/(C_n + K_d)$, where $K_d = k_-/k_+$ is the dissociation constant. The probability mass distribution for Eq. (1) can be expressed as:

$$f_n(x_n|\mathbf{\Theta}) = P_n^{x_n}(1 - P_n)^{1-x_n}, \quad \text{for} \quad x_n \in \{0, 1\}, \tag{3.4}$$

where $\mathbf{\Theta} \equiv \{p, \phi\}$ represents the parameters to estimate. Therefore, the likelihood function for a sample of N independent receptors is given by

$$\mathcal{L}(\mathbf{\Theta}|x_1, ..., x_N) = f(x_1, ..., x_N|\mathbf{\Theta}) = \prod_{n=1}^{N} f_n(x_n|\mathbf{\Theta}), \tag{3.5}$$

and the log-likelihood function is

$$\begin{aligned}
\ln \mathcal{L} &= \sum_n \left[x_n \ln \frac{C_n}{C_n + K_d} + (1 - x_n) \ln \frac{K_d}{C_n + K_d} \right] \\
&= \sum_n x_n \ln \frac{C_n}{K_d} + \sum_n \ln \frac{K_d}{C_n + K_d} \\
&= \frac{1}{2} \sum_n x_n p \cos(\varphi_n - \phi) + \ln \frac{C_0}{K_d} \sum_n x_n \\
&\quad + \int_0^{2\pi} \frac{N}{2\pi} \ln \left[\frac{K_d}{C_0 \exp\left[\frac{p}{2} \cos(\varphi - \phi)\right] + K_d} \right] d\varphi \\
&= \frac{p \cos\phi}{2} \sum_n x_n \cos\varphi_n + \frac{p \sin\phi}{2} \sum_n x_n \sin\varphi_n \\
&\quad + \ln \frac{C_0}{K_d} \sum_n x_n - \frac{N C_0 K_d p^2}{16(C_0 + K_d)^2} + \mathcal{O}(p^4).
\end{aligned} \tag{3.6}$$

Here, we introduce the transformation $\mathbf{\Theta}_\alpha = (\alpha_1, \alpha_2)^T \equiv (p\cos\phi, p\sin\phi)^T$ and define $(z_1, z_2) \equiv (\sum_n x_n \cos\varphi_n, \sum_n x_n \sin\varphi_n)$ which measures the spatial asymmetry in the receptor occupancy. Then, we have $p^2 = \alpha_1^2 + \alpha_2^2$, and for shallow gradients the log-likelihood function becomes

$$\ln \mathcal{L} \approx \frac{\alpha_1 z_1 + \alpha_2 z_2}{2} + \ln \frac{C_0}{K_d} \sum_n x_n - \frac{N C_0 K_d (\alpha_1^2 + \alpha_2^2)}{16(C_0 + K_d)^2}. \tag{3.7}$$

The method of *maximum likelihood* estimates the unknown parameters by finding a value of $\mathbf{\Theta}_\alpha$ that maximizes $\mathcal{L}(\mathbf{\Theta}_\alpha | x_1, ..., x_N)$, i.e.,

$$\widehat{\mathbf{\Theta}}_{\alpha,\mathbf{mle}} = \arg\max_{\mathbf{\Theta}_\alpha} \mathcal{L}(\mathbf{\Theta}_\alpha | x_1, ..., x_N). \tag{3.8}$$

Since the logarithm is a continuous strictly increasing function over the range of the likelihood, the values which maximize the likelihood will also maximize its logarithm. Thus, the MLE can be found from $\partial_{\alpha_1} \ln \mathcal{L} = 0$ and $\partial_{\alpha_2} \ln \mathcal{L} = 0$, with the following solution

$$\widehat{\mathbf{\Theta}}_{\alpha,\mathbf{mle}} = \begin{pmatrix} \widehat{\alpha}_1 \\ \widehat{\alpha}_2 \end{pmatrix} = \frac{1}{\mu} \begin{pmatrix} z_1 \\ z_2 \end{pmatrix}, \quad \text{where} \quad \mu \equiv \frac{N C_0 K_d}{4(C_0 + K_d)^2}. \tag{3.9}$$

This solution is indeed the maximum of the likelihood function since it is the only turning point in $\mathbf{\Theta}_\alpha$ and the second derivative is strictly less than zero. By the

properties of MLE, both $\widehat{\alpha}_1$ and $\widehat{\alpha}_2$ are asymptotically unbiased and normal as the sample size N goes to infinity, i.e., $\widehat{\alpha}_1 \xrightarrow{d} \mathcal{N}(\alpha_1, \sigma_1^2)$ and $\widehat{\alpha}_2 \xrightarrow{d} \mathcal{N}(\alpha_2, \sigma_2^2)$, where "$\xrightarrow{d}$" denotes convergence in distribution. The asymptotic variances σ_1^2 and σ_2^2 can be derived from the inverse of the Fisher information matrix [76]. This matrix has to be diagonal here as α_1 and α_2 are independent of each other. Thus, we have

$$\frac{1}{\sigma_{1,2}^2} = \mathbb{E}\left[\left(\frac{\partial \ln \mathcal{L}}{\partial \alpha_{1,2}}\right)^2\right] = -\mathbb{E}\left[\frac{\partial^2 \ln \mathcal{L}}{\partial \alpha_{1,2}^2}\right] = \frac{\mu}{2}, \tag{3.10}$$

where $\mathbb{E}[\cdot]$ represents the expectation and the proof of the second equality can be found in [76]. This equality holds because $\ln \mathcal{L}$ is twice differentiable with respect to α_1 and α_2. From the relation $\widehat{\alpha}_{1,2} = z_{1,2}/\mu$, we can see that $\mathbb{E}[z_{1,2}] = \mu\alpha_{1,2}$ and that the asymptotic variances of z_1 and z_2 are equal:

$$\sigma^2 = \mu^2\sigma_{1,2}^2 = 2\mu^2/\mu = 2\mu. \tag{3.11}$$

In addition, one can check that $\mathrm{Cov}[z_1, z_2] = 0$, as reflected in the affine form of the log-likelihood: $\ln \mathcal{L} = \alpha_1 z_1/2 + \alpha_2 z_2/2 + ...$ Thus, for small p, the joint probability density of z_1 and z_2 is [75, 96]

$$P(z_1, z_2|\mathbf{\Theta}_\alpha) = \frac{1}{2\pi\sigma^2} \exp\left[-\frac{(z_1 - \mu\alpha_1)^2 + (z_2 - \mu\alpha_2)^2}{2\sigma^2}\right]. \tag{3.12}$$

As the one-to-one transformation of $\widehat{\mathbf{\Theta}}_{\alpha,\mathbf{mle}}$, the MLE of $\mathbf{\Theta} = (p, \phi)^T$ is given by

$$\widehat{\mathbf{\Theta}}_{\mathbf{mle}} = \begin{pmatrix} \widehat{p} \\ \widehat{\phi} \end{pmatrix} = \begin{pmatrix} \mu^{-1}\sqrt{z_1^2 + z_2^2} \\ \arctan(z_2/z_1) \end{pmatrix}. \tag{3.13}$$

If we introduce the complex random variable $\mathbf{Z} \equiv z_1 + iz_2$, then $\mathbf{Z}$ follows the complex Gaussian distribution, and in the polar coordinates $\mathbf{Z} = \mu\widehat{p}\exp(i\widehat{\phi})$. Eq. (3.12) suggests that we can define a *signal-to-noise* (SNR) ratio

$$\kappa \equiv \frac{\mu^2 p^2}{\sigma^2} = \frac{\mu p^2}{2} = \frac{N p^2 C_0 K_d}{8(C_0 + K_d)^2}. \tag{3.14}$$

Again, by the properties of MLE, both $\widehat{p}$ and $\widehat{\phi}$ tend to be unbiased and normal in the large N limit, i.e., $\widehat{p} \xrightarrow{d} \mathcal{N}(p, \sigma_p^2)$ and $\widehat{\phi} \xrightarrow{d} \mathcal{N}(\phi, \sigma_\phi^2)$. It has been found numerically that the asymptotic normality becomes excellent when the SNR is larger

than 9 [78, 75]. Similarly, the asymptotic variances σ_p^2 and σ_ϕ^2 can be computed from the inverse of the Fisher information matrix with respect to $\mathbf{\Theta} = (p, \phi)$. The matrix is still diagonal due to the orthogonality of p and ϕ. Thus, we have

$$\frac{1}{\sigma_p^2} = \mathbb{E}\left[\left(\frac{\partial \ln \mathcal{L}}{\partial p}\right)^2\right] = -\mathbb{E}\left[\frac{\partial^2 \ln \mathcal{L}}{\partial p^2}\right] = \frac{\mu}{2}, \tag{3.15}$$

$$\frac{1}{\sigma_\phi^2} = \mathbb{E}\left[\left(\frac{\partial \ln \mathcal{L}}{\partial \phi}\right)^2\right] = -\mathbb{E}\left[\frac{\partial^2 \ln \mathcal{L}}{\partial \phi^2}\right] = \frac{\mu p^2}{2}, \tag{3.16}$$

or equivalently

$$\sigma_p^2 = \frac{8(C_0 + K_d)^2}{NC_0K_d} \quad \text{and} \quad \sigma_\phi^2 = \frac{8(C_0 + K_d)^2}{Np^2C_0K_d} = \frac{1}{\kappa}. \tag{3.17}$$

The above results are identical to the ones we have recently derived in [75]. According to the Cramér-Rao inequality, the variances σ_p^2 and σ_ϕ^2 represent the minimal uncertainties of gradient measurements from an instantaneous sampling of the receptor states [76].

If the cell in question integrates receptor signals over some time interval $\mathcal{T}$, then averaging over multiple measurements should obviously reduce the errors of gradient sensing. However, the error-reduction via temporal averaging is limited by the expected time it takes for every independent measurement. As shown in [73, 55], the time to make a single measurement is roughly twice the receptor correlation time τ which results from the diffusion and binding of ligand molecules. So the number of independent measurements a cell can make within $\mathcal{T}$ is about $\mathcal{T}/(2\tau)$. The correlation time can be decomposed as $\tau = \tau_{\text{rec}} + \tau_{\text{diff}}$, where $\tau_{\text{rec}} = 1/(k_- + C_0k_+)$ is the timescale of receptor-ligand reaction and τ_{diff} describes the diffusive transport time of ligands. Let $\eta \equiv \tau_{\text{diff}}/\tau_{\text{rec}}$, then the measurement is reaction-limited if $\eta \ll 1$ and diffusion-limited if $\eta \gg 1$ [64]. In a sum of the above arguments, we find that averaging signals over $\mathcal{T}$ yields a lower uncertainty of the gradient estimate,

$$\sigma_{p,\mathcal{T}}^2 \simeq \frac{2\tau}{\mathcal{T}}\sigma_p^2 = \frac{4\tau_{rec}(1+\eta)}{\mu\mathcal{T}} = \frac{16(1+\eta)(C_0+K_d)}{N\mathcal{T}k_-C_0}. \tag{3.18}$$

We shall have similar results for the direction inference, since $\sigma_{\phi,\mathcal{T}}^2 = \sigma_{p,\mathcal{T}}^2/p^2$. For typical eukaryotic cells, it has been estimated [73, 64] that $\eta \ll 1$, which implies $\sigma_{\phi,\mathcal{T}}^2 \simeq 16(C_0 + K_d)/(Np^2\mathcal{T}k_-C_0)$.

A hidden assumption in the above derivation as well as in our previous paper [75] is that the cell in question can tell the location of each receptor, as reflected in $(z_1, z_2) \equiv (\sum_n x_n \cos\varphi_n, \sum_n x_n \sin\varphi_n)$ which keep track of every individual receptor and its spatial position. Since the density of receptors on the cell surface can be high, one may argue that the cell cannot distinguish between receptors that are very close to each other. Nonetheless, we can easily relax this hidden assumption by taking advantage of the *Central Limit Theorem* (CLT). We divide the cell surface into M small sensory sectors such that receptors in the same sector are responding to an almost identical chemical concentration. Therefore, receptors in the same sector can be regarded as independent and identically distributed (Bernoulli) random variables, and the state of each sector should be represented by its receptor occupancy number which follows the binomial distribution. One can think of M as a quantity that reflects to what extent the cell can spatially distinguish its receptors. Of course, we want to ensure that the number of receptors in each sector $N_s = N/M$ is large enough for the application of CLT. For example, we may choose $M = 1000$ for $N = 40,000$, leading to $N_s = 40$. Now the local concentration at the m_{th} sector with angular position $\vartheta_m = 2\pi m/M$ is given by $C_m = C_0 \exp\left[\frac{p}{2}\cos(\vartheta_m - \phi)\right]$ for $m = 1, ..., M$. In a single snapshot, the number of occupied receptors in the m_{th} sector is approximately a Gaussian random variable by CLT, denoted $y_m = N_s C_m/(C_m + K_d) + \eta_m$ for $m = 1, ..., M$. The random component η_m satisfies $\langle\eta_m\rangle = 0$ and $\langle\eta_m\eta_n\rangle = \delta_{mn} N_s C_m K_d/(C_m + K_d)^2 \approx \delta_{mn} N_s C_0 K_d/(C_0 + K_d)^2$ [64, 50, **?**], which means the variance of y_m is approximately the same for all sectors. For small gradients, we can expand y_m around p:

$$y_m \approx \frac{N_s C_0}{K_d + C_0} + \frac{N_s K_d C_0}{2(C_0 + K_d)^2} p\cos(\vartheta_m - \phi) + \eta_m. \tag{3.19}$$

We can see that the sector states, denoted by $\mathbf{Y} = \{y_1, y_2, ..., y_M\}^T$, constitute a vector of independent Gaussian random variables with space-dependent means but approximately identical variance $\sigma_s^2 \equiv N_s K_d C_0/(C_0 + K_d)^2$. Hereafter, the superscript symbol ^{T} means transpose. Eq. (3.19) suggests that one can view $\mathbf{Y} = \{y_1, y_2, ..., y_M\}^T$ as observations of a sinusoidal signal corrupted by some

white Gaussian noise. The likelihood function of $\mathbf{Y}$ conditional on $\mathbf{\Theta}$ reads,

$$P(\mathbf{Y}|\mathbf{\Theta}) \approx \frac{1}{(2\pi\sigma_s^2)^{M/2}} \exp\left[-\frac{J(\mathbf{Y}|\mathbf{\Theta})}{2\sigma_s^2}\right], \tag{3.20}$$

where

$$J(\mathbf{Y}|\mathbf{\Theta}) = \sum_{m=1}^{M} \left(y_m - \frac{N_s C_0}{C_0 + K_d} - \frac{\sigma_s^2}{2} p\cos(\vartheta_m - \phi)\right)^2. \tag{3.21}$$

To maximize $P(\mathbf{Y}|\mathbf{\Theta})$ is equivalent to minimize $J(\mathbf{Y}|\mathbf{\Theta})$ which can be converted to a quadratic function by the one-to-one transformation $\mathbf{\Theta}_\alpha = (\alpha_1, \alpha_2)^T = (p\cos\phi, p\sin\phi)^T$:

$$J(\mathbf{Y}|\mathbf{\Theta}_\alpha) = (\mathbf{Y} - \mathbf{Y_0} - \mathbf{H}\mathbf{\Theta}_\alpha)^T(\mathbf{Y} - \mathbf{Y_0} - \mathbf{H}\mathbf{\Theta}_\alpha), \tag{3.22}$$

with

$$\mathbf{Y_0} = \frac{N_s C_0}{C_0 + K_d} \begin{pmatrix} 1 \\ 1 \\ ... \\ 1 \end{pmatrix} \quad \text{and} \quad \mathbf{H} = \frac{\sigma_s^2}{2} \begin{pmatrix} \cos\vartheta_1 & \sin\vartheta_1 \\ \cos\vartheta_2 & \sin\vartheta_2 \\ ... & ... \\ \cos\vartheta_M & \sin\vartheta_M \end{pmatrix}$$

We can apply the formula of *ordinary least squares* (OLS) estimate to find the MLE solution that minimizes the quadratic objective function $J(\mathbf{Y}|\mathbf{\Theta}_\alpha)$ and hence maximizes the likelihood function $P(\mathbf{Y}|\mathbf{\Theta}_\alpha)$:

$$\widehat{\mathbf{\Theta}}_{\alpha,\mathbf{mle}} = (\mathbf{H}^T\mathbf{H})^{-1}\mathbf{H}^T(\mathbf{Y} - \mathbf{Y_0}). \tag{3.23}$$

For large M, we have $\frac{1}{M}\sum_m \cos\vartheta_m \approx \frac{1}{M}\sum_m \sin\vartheta_m \approx 0$, $\frac{1}{M}\sum_m \cos\vartheta_m \sin\vartheta_m \approx 0$, and $\frac{1}{M}\sum_m \cos^2\vartheta_m \approx \frac{1}{M}\sum_m \sin^2\vartheta_m \approx 1/2$. Thus,

$$\begin{aligned} \widehat{\mathbf{\Theta}}_{\alpha,\mathbf{mle}} &= \begin{pmatrix} \widehat{\alpha}_1 \\ \widehat{\alpha}_2 \end{pmatrix} \approx \frac{4}{\sigma_s^4} \begin{pmatrix} M/2 & 0 \\ 0 & M/2 \end{pmatrix}^{-1} \mathbf{H}^T(\mathbf{Y} - \mathbf{Y_0}) \\ &= \frac{4(C_0 + K_d)^2}{N K_d C_0} \begin{pmatrix} \sum_m y_m \cos\vartheta_m \\ \sum_m y_m \sin\vartheta_m \end{pmatrix} \simeq \frac{1}{\mu} \begin{pmatrix} z_1 \\ z_2 \end{pmatrix}, \end{aligned}$$

where in the last line we have noticed that $z_1 = \sum_n x_n \cos\varphi_n \simeq \sum_m y_m \cos\vartheta_m$ and $z_2 = \sum_n x_n \sin\varphi_n \simeq \sum_m y_m \sin\vartheta_m$ for sufficiently large M. By inverse mapping,

we recover the MLE of $\mathbf{\Theta}$ given in Eq. (3.13). According to the asymptotic properties, $\widehat{\mathbf{\Theta}}_{\mathbf{mle}} = (\widehat{p}, \widehat{\phi})^T \xrightarrow{d} \mathcal{N}(\mathbf{\Theta}, \mathbf{I}(\mathbf{\Theta})^{-1})$, with the Fisher information matrix:

$$\begin{aligned} \mathbf{I}(\mathbf{\Theta}) &= \mathbb{E}\left[\frac{\partial \ln P(\mathbf{Y}|\mathbf{\Theta})}{\partial \mathbf{\Theta}_i}\frac{\partial \ln P(\mathbf{Y}|\mathbf{\Theta})}{\partial \mathbf{\Theta}_j}\right] \\ &\approx \begin{pmatrix} M\sigma_s^2/8 & 0 \\ 0 & M\sigma_s^2 p^2/8 \end{pmatrix} \\ &= \begin{pmatrix} \mu/2 & 0 \\ 0 & \mu p^2/2 \end{pmatrix}. \end{aligned} \tag{3.24}$$

Then, we recover our main MLE results:

$$\widehat{p} = \mu^{-1}\sqrt{z_1^2 + z_2^2} \xrightarrow{d} \mathcal{N}\left(p, \sigma_p^2 = \frac{2}{\mu}\right), \tag{3.25}$$

$$\widehat{\phi} = \arctan(z_2/z_1) \xrightarrow{d} \mathcal{N}\left(\phi, \sigma_\phi^2 = \frac{2}{\mu p^2}\right). \tag{3.26}$$

3.2.3 Summary

In this paper, we have used various concepts and techniques in estimation theory to investigate the physical limits of eukaryotic gradient sensing. We have derived explicit formulas for the variances of estimating both the gradient direction and steepness for an elliptical cell.Our theoretical and numerical results all suggest that a cell cannot improve its sensing of both the gradient steepness and direction at the same time by simply elongating itself. We also show that highly eccentric cell shapes can significantly change the gradient sensing limits, which may be relevant in experimental observations for chemotactic eukaryotes like neutrophils and *Dictyostelium*. Finally, we examined how an intracellular bias may distort the cell's perception of external stimuli. As expected, the accuracy of gradient detection increases when the internal bias aligned with the external gradient but decreases when the direction of the internal bias is significantly different from the external gradient direction. Our approach is general and in principle can be extended to cases including non-uniformly distributed receptors or more complicated cell shapes.

3.3 Acknowledgements

This Chapter, in part, contains the published material as it appears in "External and internal constraints on eukaryotic chemotaxis", Danny Fuller, Wen Chen, Micha Alder, Alex Groisman, Herbert Levine, Wouter-Jan Rappel and Williams F. Loomis, *Proc. Nat. Acad. Sci. USA*, **107**, 9656 (2010), and "How geometry and internal bias affect the accuracy of eukaryotic gradient sensing", Bo Hu, Wen Chen, Wouter-Jan Rappel, and Herbert Levine, *Physical Review E*, **83**, 021917 (2011). The dissertation author was the primary investigator and author of these papers.

Chapter 4

Biological Switch

4.1 Introduction

A wide spectrum of biological processes are mediated by certain ligand-receptor systems where receptors randomly alternate between bound and unbound states upon interacting with diffusing ligands [79]. For example, both prokaryotic and eukaryotic gene transcription depends on whether DNA promoters are occupied by specific transcription factors which either recruit or block RNA polymerase [80, 81, 82, 83, 84]. At synapses, the ligand-gated ion channels are responsible to convert the presynaptical chemical message into postsynaptic electrical signals. The opening and closing of those channels are directly linked to the binding and unbinding of specific ligands [79]. As our last example, eukaryotic chemotaxis requires an accurate sensing of chemical gradients, which is accomplished by utilizing chemoreceptors to detect external ligand concentrations [85]. A common issue behind all the above phenomena is that input signals (ligand concentrations) are intrinsically noisy, due to molecular diffusion [86] or as a result of stochastic births and deaths of molecules [87]. This raises a central question concerning the role of input noise in regulatory circuits.

Recent years have witnessed appreciable research efforts devoted to tackle this problem [87, 88, 89, 90, 91, 92, 93, 94, 95, 96], mostly using the Langevin approach with linear-noise approximation and/or the fluctuation-dissipation theorem. These approaches and associated results have facilitated a widely accepted

view that the input noise will contribute additively to the variance of the output. Previous approaches, however, involve a few caveats that deserve a careful discussion. First, it is necessary to assume that the fluctuations of input signals are very small such that one can linearize the input noise in the chemical Langevin equation. Remarkably, this linear-noise approximation itself guarantees the *additive noise rule* because equation variables are continuous. Second, previous methods usually lead to results in terms of the input-output variance relationship, whereas other details about the system, such as the residence time statistics, have been largely ignored. Third, when dealing with a single receptor (e.g., an individual DNA promoter), the linear-noise method is inappropriate: the Langevin equation with constant input is originally derived based on an infinite number of independent copies of the system; if one modifies this equation by allowing the input variable to fluctuate, the resulting equation demands that all those system copies be subject to identical input fluctuations, and hence it no longer describes an independent statistical ensemble.

4.2 Model

In this Letter, we propose a different theoretical framework that avoids all the above caveats and generates new insights about the ligand-receptor system. The input of our model, denoted by $X(t)$, represents the ligand concentration at time t and directly regulates the transition rates of a downstream receptor. The receptor states in continuous time constitute the output process, $Y(t)$. A popular proposal for $X(t)$ may be the Ornstein-Uhlenbeck (OU) process for its analytical simplicity and mean-reverting property [97]. However, the OU process may take negative values, an undesirable feature for modeling chemical concentrations. Here, we choose for $X(t)$ the following square-diffusion process [98], which is mostly well-known as the Cox-Ingersoll-Ross (CIR) model [99] for interest rates in mathematical finance:

$$dX(t) = \lambda(\mu - X(t))dt + \sigma\sqrt{X(t)}dW_t. \tag{4.1}$$

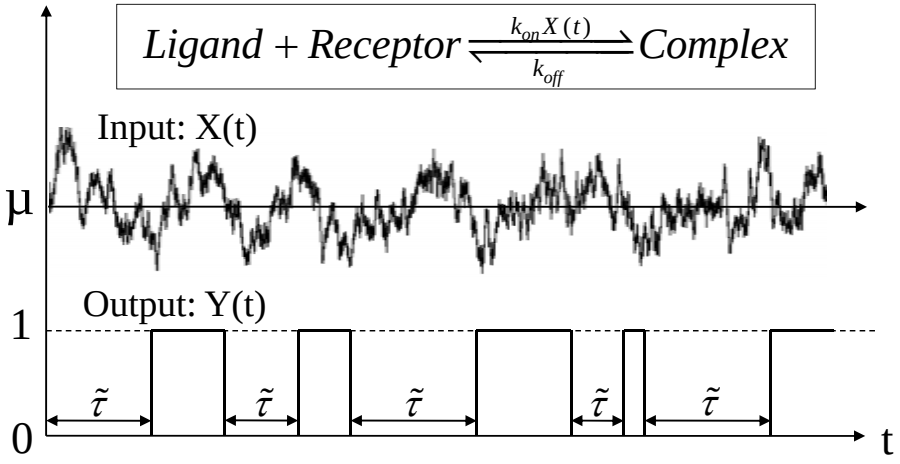

Figure 4.1: $X(t)$ represents the ligand concentration which fluctuates in time, while $Y(t)$ records the receptor configuration which alternates between the unbound ($Y = 0$) and bound ($Y = 1$) states, with transition rates $k_{\text{on}}X(t)$ and k_{off} for simple receptor-ligand kinetics. The first passage time $\widetilde{\tau}$ for the receptor switching into the bound state is equivalent to its residence time of staying unbound.

Here, λ represents the rate at which $X(t)$ will approach its steady-state mean value μ, σ controls the input noise intensity, and W_t denotes the standard Wiener process. Clearly, the CIR process is not only mean-reverting but also nonnegative. Moreover, its square-root noise term captures a common statistical feature for many biochemical processes, that is, the standard deviation of chemical concentrations scale as the square root of those concentrations. The stationary solution of Eq. 4.1 is Solving the Fokker-Planck equation for Eq. 4.1 yields the steady-state solution,

$$P_s(X = x) = \frac{\beta^\alpha x^{\alpha-1} e^{-\beta x}}{\Gamma(\alpha)}, \quad \alpha \equiv \frac{2\mu\lambda}{\sigma^2}, \quad \beta \equiv \frac{2\lambda}{\sigma^2}, \tag{4.2}$$

which is a Gamma distribution with steady-state variance $\sigma_X^2 = \mu\sigma^2/(2\lambda)$. The parameter α in Eq. (2) can be interpreted as the *signal-to-noise ratio*, since we have $\alpha = \mu^2/\sigma_X^2$. For $\alpha \geq 1$ (the Feller condition), the origin is guaranteed to be inaccessible for $X(t)$. Using Itó calculus [97], one can also find its steady-state covariance: $\text{Cov}[X(t), X(t+s)]_{t\to\infty} = \sigma_X^2 e^{-\lambda|s|}$. Therefore, $X(t)$ is a stationary Markov process with the relaxation time λ^{-1}.

For the simplest receptor-ligand reaction (Fig. 4.1), the forward and back-

ward transition rates of the receptor are given by $k_{\rm on}X(t)$ and $k_{\rm off}$, respectively. If we ignore any fluctuations of $X(t)$, the output process $Y(t)$ is simply a two-state continuous-time Markov process with transition rates $k_{\rm on}\mu$ and $k_{\rm off}$. Since the backward rate $k_{\rm off}$ is constant in both cases, we expect that the input fluctuations will affect the switching dynamics only when the receptor is unbound. In general, the input noise will make $Y(t)$ a non-Markovian process because the residence times for the receptor staying unbound will no longer be exponentially distributed. To demonstrate this point more rigorously, we consider the following first passage time problem. Without loss of generality, suppose the receptor starts being unbound at $t = 0$ and the initial ligand concentration is $X(t = 0) = x$. Let $\widetilde{\tau}$ denote the first time of the receptor switching into the bound state. Then the *survival probability* for the receptor staying unbound, conditioned on the initial input value, is

$$f(x,t) \equiv P(\widetilde{\tau} > t|X(0) = x) = \mathrm{E}^x \left[e^{-\int_0^t k_{\rm on} X(s) ds} \right], \tag{4.3}$$

where $\mathrm{E}^x[...]$ denotes expectation over all possible sample paths of $X(s)$ for $0 \leq s \leq t$, conditioned on $X(0) = x$. The Feynman-Kac formula [97] asserts that $f(x,t)$ solves the following partial differential equation:

$$\frac{\partial f(x,t)}{\partial t} = \lambda(\mu - x)\frac{\partial f}{\partial x} + \frac{1}{2}\sigma^2 x \frac{\partial^2 f}{\partial x^2} - k_{\rm on} x f, \tag{4.4}$$

with initial condition $f(x, 0) = 1$. A structurally similar equation to Eq. 4.4 has been solved in Ref. [99] to price financial bonds under the CIR interest rate model. The exact solution for our problem is similar and found to be:

$$f(x,t) = \left[\frac{\widetilde{\lambda} e^{\lambda t/2} / \sinh(\widetilde{\lambda} t/2)}{\lambda + \widetilde{\lambda} \coth(\widetilde{\lambda} t/2)} \right]^{\alpha} \exp\left[\frac{-2k_{\rm on} x}{\lambda + \widetilde{\lambda} \coth(\widetilde{\lambda} t/2)} \right], \tag{4.5}$$

where $\widetilde{\lambda} \equiv \sqrt{\lambda^2 + 2k_{\rm on}\sigma^2} = \lambda\sqrt{1 + 2k_{\rm on}\sigma^2/\lambda^2}$. Evidently, $f(x,t)$ remembers the initial input x and decays with t in a manner that is not exactly exponential.

To see how the output dynamics under input noise will deviate from that of a constant input model, we first study the case where $X(t)$ relaxes to its equilibrium very rapidly such that $\lambda^{-1} \ll \mathcal{T}_Y$. Here, $\mathcal{T}_Y \equiv (k_{\rm on}\mu + k_{\rm off})^{-1}$ is the output autocorrelation time for the constant input model. In this case, the initial input

value x in $f(x,t)$ is effectively drawn from the stationary distribution $P_s(x)$ given by Eq. 4.2, and all the residence times during which the receptor staying unbound are almost independent with each other. The distribution of these residence times is $P(\widetilde{\tau} \leq t) = 1 - P(\widetilde{\tau} > t) = 1 - \int_0^\infty f(x,t)P_s(x)dx$, where by direct integration we find

$$\begin{aligned} P(\widetilde{\tau} > t) &= \left[\frac{\beta\widetilde{\lambda}e^{\lambda t/2}}{(\beta\lambda + 2k_{\rm on})\sinh(\widetilde{\lambda}t/2) + \beta\widetilde{\lambda}\cosh(\widetilde{\lambda}t/2)}\right]^\alpha \\ &\simeq \left[\frac{2\beta\widetilde{\lambda}e^{-(\widetilde{\lambda}-\lambda)t/2}}{\beta(\lambda+\widetilde{\lambda}) + 2k_{\rm on}}\right]^\alpha \simeq \exp(-\widetilde{k}_{\rm on}\mu t). \end{aligned} \tag{4.6}$$

In the last step of the above derivation, we have used the following relationship which defines the parameter $\widetilde{k}_{\rm on}$:

$$\frac{\alpha(\widetilde{\lambda}-\lambda)}{2\mu} = \frac{\lambda}{\sigma^2}(\widetilde{\lambda}-\lambda) = \frac{2\lambda}{\widetilde{\lambda}+\lambda}k_{\rm on} \equiv \widetilde{k}_{\rm on} \leq k_{\rm on}. \tag{4.7}$$

By introducing $\theta \equiv k_{\rm on}\sigma^2/\lambda^2$ which reflects the deviation of $\widetilde{\lambda}$ from λ, one can also check that as long as $\lambda \gg k_{\rm on}\mu$ (as guaranteed by $\lambda^{-1} \ll \mathcal{T}_Y$), it holds regardless of θ:

$$\left[\frac{2\beta\widetilde{\lambda}}{\beta(\lambda+\widetilde{\lambda}) + 2k_{\rm on}}\right]^\alpha = \left(\frac{1}{2} + \frac{1+\theta}{2\sqrt{1+2\theta}}\right)^{-\frac{2}{\theta}\cdot\frac{k_{\rm on}\mu}{\lambda}} \simeq 1.$$

Fig. 4.2A shows that the approximate result $P(\widetilde{\tau} > t) \simeq e^{-\widetilde{k}_{\rm on}\mu t}$ is strikingly excellent, independent of the values of θ. Hence the output $Y(t)$ can be well approximated as a two-state Markov process with transition rates $\widetilde{k}_{\rm on}\mu$ and $k_{\rm off}$. The probability to find $Y = 1$ is then given by $\mu/(\mu + \widetilde{K}_d)$, where $\widetilde{K}_d \equiv k_{\rm off}/\widetilde{k}_{\rm on}$ is the *effective* dissociation constant. Combining the assumption $\lambda^{-1} \ll \mathcal{T}_Y$ with the Feller condition $\alpha = \mu^2/\sigma_X^2 \geq 1$, we see that:

$$\theta \equiv k_{\rm on}\frac{\sigma^2}{\lambda^2} = \frac{2k_{\rm on}\mu}{\lambda}\left(\frac{\sigma_X^2}{\mu^2}\right) \ll 1 \quad \text{and} \quad \widetilde{\lambda} \simeq \lambda(1+\theta). \tag{4.8}$$

So the stationary variance of $Y(t)$ can be expanded as:

$$\begin{aligned} \widetilde{\sigma}_Y^2 &= \frac{\mu\widetilde{K}_d}{(\mu+\widetilde{K}_d)^2} \simeq \sigma_Y^2 + \frac{\mu K_d(\mu - K_d)}{2(\mu+K_d)^3}\theta + \mathcal{O}(\theta^2), \\ &= \sigma_Y^2 + \frac{\mu - K_d}{(\mu+K_d)^3}\frac{k_{\rm off}}{\lambda}\sigma_X^2 + \mathcal{O}(\sigma_X^4), \end{aligned} \tag{4.9}$$

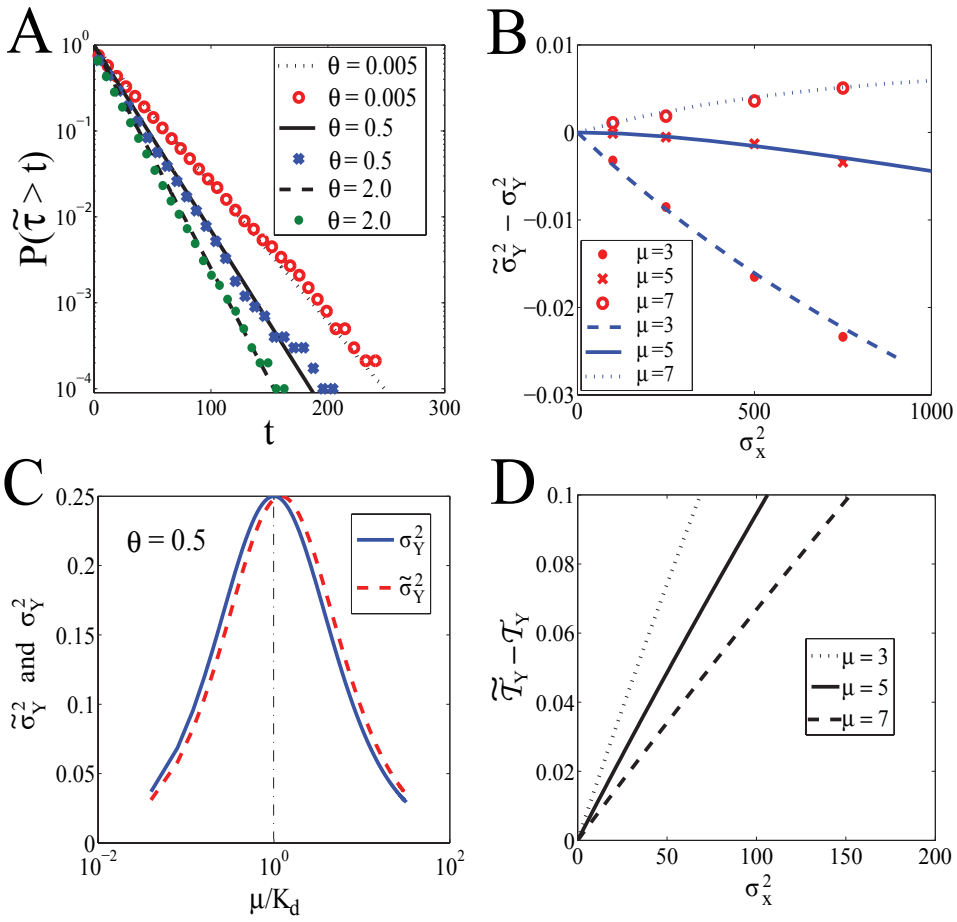

Figure 4.2: Here we use $\lambda = 10$, $k_{\text{on}} = 0.02$, and $k_{\text{off}} = 0.1$ (thus $K_d = 5$). (A) $P(\widetilde{\tau} > t)$ versus t for $\mu = 3$ and $\theta = 0.005$, 0.5, and 2.0 which are achieved by choosing $\sigma = 5$, 50, and 100. Symbols represent simulation results, while lines denote $\exp(-\widetilde{k}_{\text{on}}\mu t)$. (B) $\widetilde{\sigma}_Y^2 - \sigma_Y^2$ versus σ_X^2, where different values of σ_X^2 are obtained by tuning σ. (C) $\widetilde{\sigma}_Y^2$ and σ_Y^2 versus μ/K_d with $\theta = 0.50$. (D) $\widetilde{\mathcal{T}}_Y - \mathcal{T}_Y$ versus σ_X^2.

where $\sigma_Y^2 \equiv \mu K_d/(\mu + K_d)^2$ is the output variance of the constant input model and $K_d \equiv k_{\rm off}/k_{\rm on}$ is the *original* dissociation constant. Eq. 4.9 indicates that the input noise σ_X^2 does not always contribute additively to the output variance $\widetilde{\sigma}_Y^2$. In fact, the contribution is negligible when μ is near K_d and even negative for $\mu < K_d$ (Fig. 4.2B). This seemingly surprising result has a simple explanation: a two-state switch at any moment is just a Bernoulli random variable and hence its variance is strictly upper bounded by one quarter. From Eq. 4.9 and Fig. 4.2C, one can see that the net effect of input noise is to slightly shift the dissociation constant from K_d to $\widetilde{K}_d$. This turns out to be a general feature for any two-state (single) receptor system, no matter how the input process is assigned or whether the receptor is mediated by cooperative binding of ligands. We will elaborate this point in a separate publication. Back to our noisy input model, the output autocorrelation time is $\widetilde{\mathcal{T}}_Y \simeq (\widetilde{k}_{\rm on}\mu + k_{\rm off})^{-1}$, which can also be expanded in σ_X^2 by using Eq. 4.8:

$$\widetilde{\mathcal{T}}_Y \simeq \mathcal{T}_Y \left(1 - \frac{\widetilde{\lambda} - \lambda}{\widetilde{\lambda} + \lambda} \frac{\mu}{\mu + K_d}\right)^{-1} \simeq \mathcal{T}_Y + \frac{1}{\lambda} \frac{\sigma_X^2}{(\mu + K_d)^2}. \tag{4.10}$$

Thus, $\widetilde{\mathcal{T}}_Y$ increases almost linearly with σ_X^2 (Fig. 2D). Consider an integration of the output $Y(t)$ over a time window T (assuming $T \gg \mathcal{T}_Y$). The output variance after temporal averaging will be: $\mathrm{Var}\left[\frac{1}{T}\int_0^T Y(t)dt\right] \simeq 2\widetilde{\sigma}_Y^2 \widetilde{\mathcal{T}}_Y/T$, which may still decrease with the input noise σ_X^2 when $\mu \ll K_d$, just as $\widetilde{\sigma}_Y^2$ does (Fig. 4.2B). All the above results show that the *additive noise rule* is incomplete to characterize the input-output noise relationship for a single receptor system.

We now examine the opposite extreme where the receptor switches much faster than the input process relaxes to its equilibrium (i.e. $\lambda^{-1} \gg \mathcal{T}_Y$). Intuitively, the initial input values for successive "first-passage" events of duration $\widetilde{\tau}$ should be correlated in this case. This temporal correlation makes it difficult to calculate $P(\widetilde{\tau} > t)$ like what we have done in Eq. 4.6. We thus resort to the Monte Carlo simulations. If the input noise is sufficiently large such that $\alpha \sim \mathcal{O}(1)$, then by Eq. 4.8 we have $\theta = 2k_{\rm on}\mu/(\lambda\alpha) \gg 1$ since $\lambda << k_{\rm on}\mu$. As shown in Fig. 4.3A, the successive residence times of the receptor staying unbound are mildly correlated with each other, as a natural result of the interdependence in the input time series.

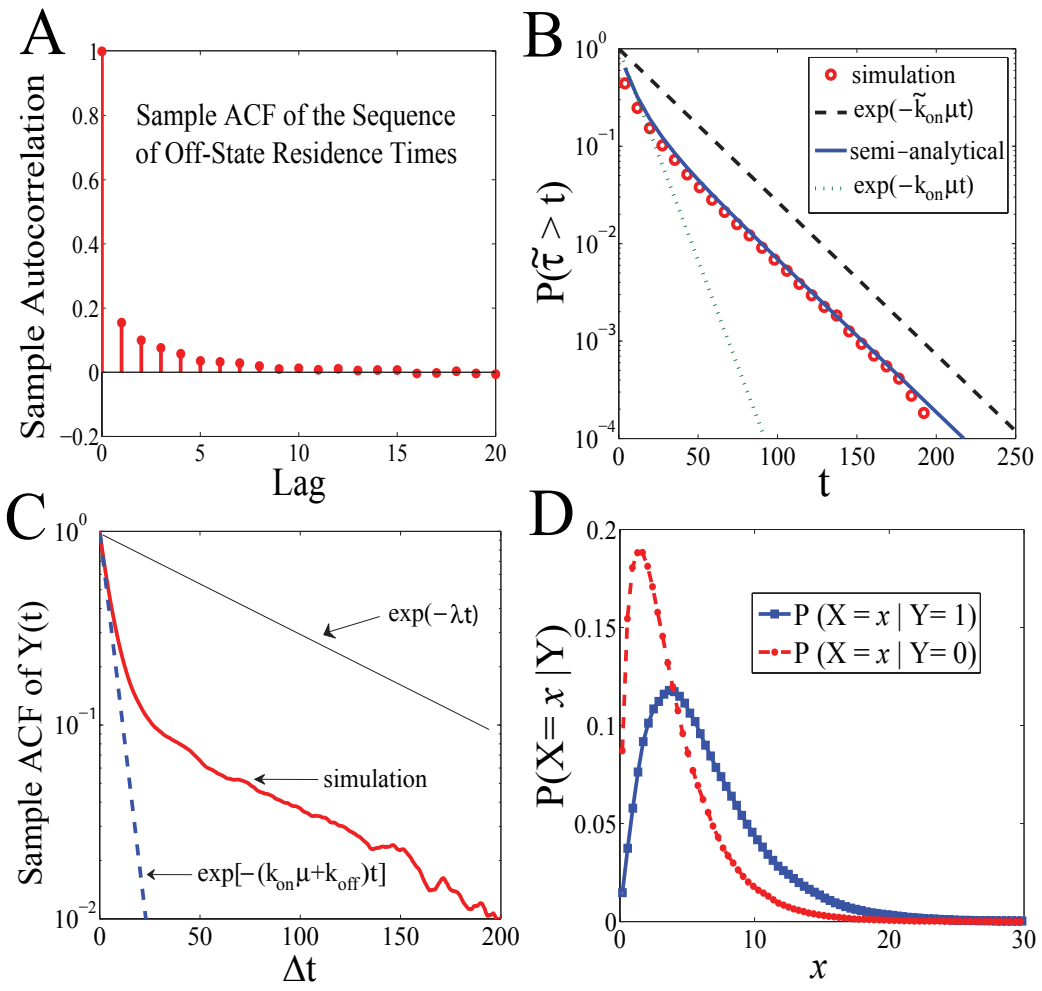

Figure 4.3: Here we choose $\lambda = 0.0125$, $\mu = 5$, $k_{\text{off}} = 0.1$, $k_{\text{on}} = 0.02$, and $\theta = 10$ (such that $\sigma \simeq 0.28$). (A) Sample ACF of successive (unbound-state) residence times. (B) Statistics of (unbound-state) residence times, where symbols are from Monte-Carlo simulation and solid line is the semi-analytical fitting described in the maintext. (C) Sample ACF of $Y(t)$ in the semi-log scale, with a subplot in the log-log scale. (D) Input distribution conditioned on the output.

The distribution of these unbound-state residence times is not simply exponential (Fig. 4.3B), especially at the head, although its tail decays exponentially again at the rate $\widetilde{k}_{\rm on}\mu$. We can still use the analytical expression $f(x,t)$ in Eq. 4.5 to fit the simulation data (open circles in Fig. 4.3B). Specifically, we evaluate $\int_0^\infty f(x,t)P_e(x)dx$ (solid line in Fig. 4.3B) where $P_e(x)$ is the empirical distribution of the initial input x for each "first-passage" event and is obtained from Monte-Carlo simulations. In Fig. 4.3C, we draw the sample *autocorrelation function* (ACF) for the simulated output process. Clearly, the ACF of $Y(t)$ exhibits a much longer tail than what one expects from a constant input model, demonstrating a long-term memory in $Y(t)$. All the above results (Fig. 4.3A-C) show that the output process $Y(t)$ is strongly non-Markovian in the dynamic scheme $\lambda^{-1} \gg \mathcal{T}_Y$ and $\theta \gg 1$. Finally, we illustrate the interdependence of the input and output processes by plotting the input distributions conditional on the output in Fig. 4.3D. In fact, $P(X = x|Y = 1) \simeq P_e(x)$.

4.3 Discussion

The results we have so far presented can have broad biological implications. The impact of input noise on the output dynamics may be quite different, depending on the input relaxation time λ^{-1} compared to the typical receptor switching time $\mathcal{T}_Y$. An usual biophysical basis for the relaxation time λ^{-1} is molecular diffusion. If the input (ligand) dynamics is governed by molecular diffusion, then a larger diffusion coefficient of the ligands will make the input noise less appreciable, consistent with the Burg-Percell formula for concentration sensing limits [86, 89, 94, 95]. Many biological processes may be classified into this scheme where fluctuations of input signals are not impactful. For example, switching of DNA promoters usually occurs at a time scale much longer than the characteristic diffusion time of transcription factors, providing a temporal averaging opportunity to suppress the input noise. Eukaryotic gradient sensing is another example where the chemoattractant cAMP diffuses so fast that one can ignore the input diffusive noise when considering cellular gradient sensing capacities [94, 96]. Nonetheless, there

exist biological situations where the input relaxes much slower than the receptor flips its states. Take for example the bacterial chemotactic movements which are generated by rotations, either clockwise or counterclockwise, of certain bacterial flagellar motors. In E. coli, the probability of clockwise motor spinning depends sharply on the concentration of CheY-P [101]. Nonetheless, the input CheY-P correlation time is dominated by slow methylation kinetics and hence should far exceed the characteristic switching time for the flagellar motors [102]. Therefore, the input noise in this system is expected to have interesting effects on the motor switching dynamics, as experimentally revealed in [100, 101] and theoretically explored in [102].

In summary, we present a new theoretical approach to analyze how input fluctuations can influence the output dynamics of a simple biochemical switch. Contrary to the common belief, our analysis shows that the presence of input noise does not necessary increase the output variance for a single switch. We also demonstrate that a long-last memory in the input process can generate non-exponential statistics in the output switching dynamics. We stress that these results are of general value since they do not rely on the details of how the input process is specifically modeled. Future research may extend our current framework by incorporating other effects like feedback loops and cooperative ligand binding.

Appendix A

Laplace Transforms

Here, we find an analytical solution for the time dependent 2D problem in the case of an instantaneous flux source:

$$\lim_{r\to 0} r\frac{\partial C_1}{\partial r} = -\frac{F}{\pi D}\delta(t) \tag{A.1}$$

We will employ the Laplace transform

$$\widetilde{C_1}(r,s) = \int_0^\infty C_1(r,t)e^{-ts}dt \tag{A.2}$$

$$\widetilde{C_2}(r,s) = \int_0^\infty C_2(r,t)e^{-ts}dt \tag{A.3}$$

for which the problem at hand is written as

$$(D\nabla^2 - \beta_1)\widetilde{C_1} = s\widetilde{C_1}, 0 \le r \le R \tag{A.4}$$

$$(D\nabla^2 - \beta_2)\widetilde{C_2} = s\widetilde{C_2}, r > R \tag{A.5}$$

with as boundary conditions:

$$\widetilde{C_1}(R,s) = \widetilde{C_2}(R,s) \tag{A.6}$$

$$\frac{\partial\widetilde{C_1}(R,s)}{\partial r} = \frac{\partial\widetilde{C_2}(R,s)}{\partial r} \tag{A.7}$$

$$\lim_{r\to 0} r\frac{\partial \widetilde{C_1}}{\partial r} = -\frac{F}{\pi D} \tag{A.8}$$

Using polar coordinates, these equations can be rewritten as

$$\frac{\partial^2 \widetilde{C_1}}{\partial r^2} + \frac{1}{r}\frac{\partial \widetilde{C_1}}{\partial r} - \frac{\beta_1 + s}{D}\widetilde{C_1} = 0 \tag{A.9}$$

$$\frac{\partial^2 \widetilde{C_2}}{\partial r^2} + \frac{1}{r}\frac{\partial \widetilde{C_2}}{\partial r} - \frac{\beta_2 + s}{D}\widetilde{C_2} = 0 \tag{A.10}$$

with as solution

$$\widetilde{C_1}(r,s) = \frac{F}{\pi D}K_0(r\gamma_1) + \frac{F}{\pi D}\frac{N_1(s)}{N(s)}I_0(r\gamma_1),\ 0 \le r \le R \tag{A.11}$$

$$\widetilde{C_2}(r,s) = \frac{F}{\pi DR}\frac{1}{N(s)}K_0(r\gamma_2),\ r > R \tag{A.12}$$

where

$$N(s) = \gamma_1 I_1(R\gamma_1)K_0(R\gamma_2) + \gamma_2 K_1(R\gamma_2)I_0(R\gamma_1) \tag{A.13}$$

$$N_1(s) = \gamma_1 K_1(Rk_1)K_0(Rk_2) - \gamma_2 K_1(R\gamma_2)K_0(R\gamma_1) \tag{A.14}$$

and $\gamma_1(s) = \sqrt{\frac{\beta_1+s}{D}}$, $\gamma_2(s) = \sqrt{\frac{\beta_2+s}{D}}$.

The final solutions can be found through the inverse Laplace transform

$$\begin{aligned} C_1(r,t) &= \frac{1}{2\pi i}\int_{x_0-i\infty}^{x_0+i\infty} \widetilde{C_1}(r,s)e^{ts}ds \\ &= \frac{F}{2\pi Dt}\exp(-\frac{r^2}{4Dt} - \beta_1 t) + \frac{F}{\pi D}\frac{1}{2\pi i}\int_{x_0-i\infty}^{x_0+i\infty}\frac{N_1(s)}{N(s)}I_0(r\gamma_1)e^{ts}ds, \end{aligned}$$

$0 \le r \le R$ (A.15)

$$\begin{aligned} C_2(r,t) &= \frac{1}{2\pi i}\int_{x_0-i\infty}^{x_0+i\infty} \widetilde{C_2}(r,s)e^{ts}ds \\ &= \frac{F}{\pi DR}\frac{1}{2\pi i}\int_{x_0-i\infty}^{x_0+i\infty}\frac{1}{N(s)}K_0(r\gamma_2)e^{ts}ds,\ r > R \end{aligned} \tag{A.16}$$

where x_0 is an arbitrary positive number.

The main challenge is to calculate the following two inverse Laplace transforms:

$$u_1(r,t) \equiv \mathcal{L}^{-1}[U_1(s)] \equiv \frac{1}{2\pi i}\int_{x_0-i\infty}^{x_0+i\infty} \frac{N_1(s)}{N(s)} I_0(r\gamma_1)e^{ts}ds, \;\; x_0 > 0 \tag{A.17}$$

$$u_2(r,t) \equiv \mathcal{L}^{-1}[U_2(s)] \equiv \frac{1}{2\pi i}\int_{x_0-i\infty}^{x_0+i\infty} \frac{1}{N(s)} K_0(r\gamma_2)e^{ts}ds, \;\; x_0 > 0 \tag{A.18}$$

where $U_1(s) = \frac{N_1(s)}{N(s)} I_0(r\gamma_1)$, $U_2(s) = \frac{1}{N(s)} K_0(r\gamma_2)$.

A.1 Region 1

We first calculate $u_1(r,t)$ by contour integration of $s = x+iy$ in the complex plane as shown in Figure A.1:

$$\begin{aligned} u_1(r,t) \;\; = \;\; & -\frac{1}{2\pi i}[\int_{BC+JA} U_1(z)e^{tz}dz + \int_{FG} U_1(z)e^{tz}dz \\ & + \int_{CD_n+\sum_{j=2}^{n} E_j D_{j-1}+E_1 F} U_1(z)e^{tz}dz \\ & + \int_{GH_1+\sum_{j=1}^{n-1} I_j H_{j+1}+I_n J} U_1(z)e^{tz}dz \\ & + \sum_{j=1}^{n} \int_{D_j E_j + H_j I_j} U_1(z)e^{tz}dz] \end{aligned} \tag{A.19}$$

Since $\beta_2 > \beta_1 \geq 0$, it is easy to proof that $N(s)$ has only zeros in the range $(-\beta_2, -\beta_1)$. We will use x_j $(j = 1, 2, \cdots, n)$ to denote these zeroes which are all located on the negative real axis. Notice that $U_1(s)$ contains the multivalued functions K_0, K_1 and $\sqrt{\cdot}$ with branch points at 0 and ∞. Consequently the contour involves a branch cut along the negative real axis of the s-plane starting from $-\beta_1$, *i.e.* $(-\infty, -\beta_1]$ (see Figure A.1).

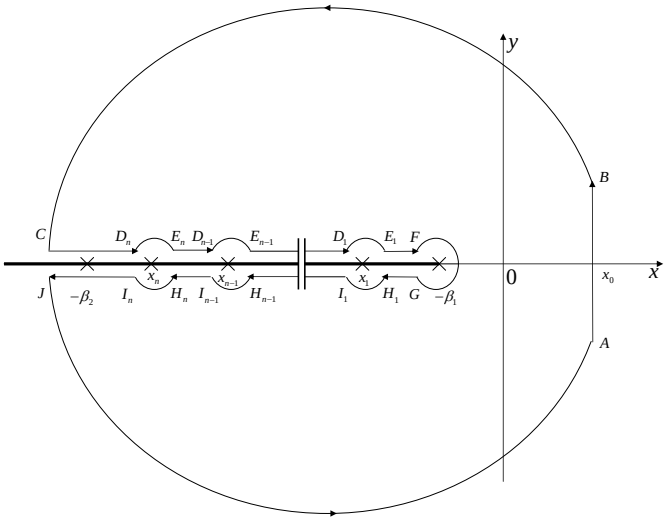

Figure A.1: The contour used to invert the Laplace transform in region 1.

In the limit $|z| \to \infty$ the contribution along the arcs BC, JA, and FG vanish. Furthermore, the last term can be evaluated using the residues of the simple poles to obtain

$$\begin{aligned} u_1(r,t) &= -\frac{1}{2\pi i}[\int_{CD_n+\sum_{j=2}^{n} E_j D_{j-1}+E_1 F} U_1(z)e^{tz}dz \\ &\quad + \int_{GH_1+\sum_{j=1}^{n-1} I_j H_{j+1}+I_n J} U_1(z)e^{tz}dz] \\ &\quad + \sum_{j=1}^{n} res[U_1(z)e^{tz}, x_j] \end{aligned} \tag{A.20}$$

Here,

$$res[U_1(z)e^{tz}, x_j] = \frac{N_1(x_j)}{N'(x_j)} I_0(r\gamma_1(x_j))e^{x_j t} \tag{A.21}$$

where the symbol $'$ means $\frac{d}{ds}$. After some algebra, we can find expressions for the single valued real functions $N_1(x_j)I_0(r\gamma_1(x_j))$ and $N'(x_j)$:

$$
\begin{aligned}
& N_1(x_j)I_0(r\gamma_1(x_j)) \\
= \; & \frac{\pi}{2}[\sqrt{\frac{x_j+\beta_2}{D}}K_1(R\sqrt{\frac{x_j+\beta_2}{D}})Y_0(R\sqrt{-\frac{x_j+\beta_1}{D}}) - \\
& \sqrt{-\frac{x_j+\beta_1}{D}}Y_1(R\sqrt{-\frac{x_j+\beta_1}{D}})K_0(R\sqrt{\frac{x_j+\beta_2}{D}})]J_0(r\sqrt{-\frac{x_j+\beta_1}{D}}) \qquad \text{(A.22)}
\end{aligned}
$$

where J and Y represent the Bessel function of the first and second kind, respectively, and

$$
\begin{aligned}
N^{'}(x_j) \; = \; & \gamma_2^{'}(x_j)K_1(R\gamma_2(x_j))J_0(R\gamma_1^*(x_j)) - \gamma_1^{*'}(x_j)J_1(R\gamma_1^*(x_j))K_0(R\gamma_2(x_j)) \\
& -\frac{R}{2}\gamma_2(x_j)\gamma_2^{'}(x_j)[K_0(R\gamma_2(x_j)) + K_2(R\gamma_2(x_j))]J_0(R\gamma_1^*(x_j)) \\
& -\frac{R}{2}\gamma_1^*(x_j)\gamma_1^{*'}(x_j)[J_0(R\gamma_1^*(x_j)) - J_2(R\gamma_1^*(x_j))]K_0(R\gamma_2(x_j)) \\
& +R[\gamma_1^*(x_j)\gamma_2^{'}(x_j) - \gamma_1^{*'}(x_j)\gamma_2(x_j)]J_1(R\gamma_1^*(x_j))K_1(R\gamma_2(x_j)) \qquad \text{(A.23)}
\end{aligned}
$$

The first two terms in Eq. A.20 are the branch cut integrals. For these, we have along $CD_n + \sum_{j=2}^{n} E_j D_{j-1} + E_1 F$: $z = xe^{\pi i}$ and $dz = e^{\pi i}dx$, so that for finite number of non-integrable points we have,

$$
\begin{aligned}
\int_{CD_n+\sum_{j=2}^{n} E_j D_{j-1}+E_1 F} U_1(z)e^{tz}dz \; &= \; \int_{-\infty}^{-\beta_1} U_1(xe^{\pi i})e^{tx}dx \\
&= \; \int_{-\infty}^{-\beta_2} U_1(xe^{\pi i})e^{tx}dx \\
&\quad + \int_{-\beta_2}^{-\beta_1} U_1(xe^{\pi i})e^{tx}dx \qquad \text{(A.24)}
\end{aligned}
$$

Along $GH_1 + \sum_{j=1}^{n-1} I_j H_{j+1} + I_n J$ we have $z = xe^{-\pi i}$ and $dz = e^{-\pi i}dx$ so that

$$
\begin{aligned}
\int_{GH_1+\sum_{j=1}^{n-1} I_j H_{j+1}+I_n J} U_1(z)e^{tz}dz \; &= \; \int_{-\beta_1}^{-\infty} U_1(xe^{-\pi i})e^{tx}dx \\
&= \; \int_{-\infty}^{-\beta_2} -U_1(xe^{-\pi i})e^{tx}dx \\
&\quad + \int_{-\beta_2}^{-\beta_1} -U_1(xe^{-\pi i})e^{tx}dx \qquad \text{(A.25)}
\end{aligned}
$$

Summing both contributions we obtain

$$\begin{aligned} & \int_{-\infty}^{-\beta_2} [U_1(xe^{\pi i}) - U_1(xe^{-\pi i})]e^{tx}dx + \int_{-\beta_2}^{-\beta_1} [U_1(xe^{\pi i}) - U_1(xe^{-\pi i})]e^{tx}dx \\ = \; & 2i \int_{-\infty}^{-\beta_2} \mathrm{Im}[U_1(xe^{\pi i})]e^{tx}dx + 2i \int_{-\beta_2}^{-\beta_1} \mathrm{Im}[U_1(xe^{\pi i})]e^{tx}dx \end{aligned} \tag{A.26}$$

For $x \in (-\infty, -\beta_2)$, both γ_1 and γ_2 are imaginary and both the nominator $N_1(z)$ and the denominator $N(z)$ of $U_1(z)$ have different values above or below the branch cut:

$$N(xe^{\pm\pi i}) = \frac{\pi}{2}(P \pm iQ),\ x \in (-\infty, -\beta_2) \tag{A.27}$$

where

$$P(x) = \gamma_1^*(x)J_1(R\gamma_1^*(x))Y_0(R\gamma_2^*(x)) - \gamma_2^*(x)J_0(R\gamma_1^*(x))Y_1(R\gamma_2^*(x)) \tag{A.28}$$

$$Q(x) = \gamma_1^*(x)J_1(R\gamma_1^*(x))J_0(R\gamma_2^*(x)) - \gamma_2^*(x)J_0(R\gamma_1^*(x))J_1(R\gamma_2^*(x)) \tag{A.29}$$

Similarly

$$I_0(r\gamma_1(xe^{\pm\pi i})) = J_0(r\gamma_1^*(x)),\ x \in (-\infty, -\beta_2) \tag{A.30}$$

$$N_1(xe^{\pm\pi i}) = \frac{\pi^2}{4}(R \pm iS),\ x \in (-\infty, -\beta_2) \tag{A.31}$$

where

$$\begin{aligned} R(x) = \; & -\gamma_1^*(x)J_1(R\gamma_1^*(x))J_0(R\gamma_2^*(x)) - \gamma_2^*(x)J_0(R\gamma_1^*(x))J_1(R\gamma_2^*(x)) \\ & +\gamma_1^*(x)Y_1(R\gamma_1^*(x))Y_0(R\gamma_2^*(x)) - \gamma_2^*(x)Y_0(R\gamma_1^*(x))Y_1(R\gamma_2^*(x)) \end{aligned} \tag{A.32}$$

$$\begin{aligned} S(x) = \; & \gamma_1^*(x)J_1(R\gamma_1^*(x))Y_0(R\gamma_2^*(x)) + \gamma_2^*(x)J_0(R\gamma_1^*(x))Y_1(R\gamma_2^*(x)) \\ & +\gamma_1^*(x)Y_1(R\gamma_1^*(x))J_0(R\gamma_2^*(x)) - \gamma_2^*(x)Y_0(R\gamma_1^*(x))J_1(R\gamma_2^*(x)) \end{aligned} \tag{A.33}$$

Thus,

$$\begin{aligned} 2i\int_{-\infty}^{-\beta_2} \mathrm{Im}[U_1(xe^{\pi i})]e^{tx}dx &= i\pi\int_{-\infty}^{-\beta_2} \frac{PS+QR}{P^2+Q^2}J_0(r\gamma_1^*)e^{tx}dx \\ \overset{x=-s-\beta_2}{=} i\pi e^{-\beta_2 t}\int_0^{\infty} F_1(r,s)e^{-ts}ds &= i\pi e^{-\beta_2 t}\mathcal{L}[F_1(r,s)] \end{aligned} \tag{A.34}$$

where

$$F_1(r,s) = \frac{P(-s-\beta_2)S(-s-\beta_2)-Q(-s-\beta_2)R(-s-\beta_2)}{P^2(-s-\beta_2)+Q^2(-s-\beta_2)}J_0(r\gamma_1^*(-s-\beta_2) \tag{A.35}$$

We can expand $\mathcal{L}[F_1(r,s)]$ in powers of $\frac{1}{t}$ by partial integration

$$\begin{aligned} \mathcal{L}[F_1(r,s)] &= \int_0^{\infty} F_1(r,s)e^{-ts}ds = -\frac{1}{t}\int_0^{\infty} F_1(r,s)de^{-ts} \\ &= -\frac{1}{t}F_1(r,s)e^{-ts}|_{s=0}^{s=\infty} - \frac{1}{t^2}\int_0^{\infty} F_1^{(1)}(r,s)de^{-ts} \\ &= -\sum_{n=1}^{\infty}\frac{1}{t^n}F_1^{(n-1)}(r,s)e^{-ts}|_{s=0}^{s=\infty} \end{aligned} \tag{A.36}$$

where $F_1^{(n)}(r,s) = \frac{\partial^n F_1(r,s)}{\partial s^n}$. After keeping only the first order of $\frac{1}{t}$, we obtain

$$\mathcal{L}[F_1(r,s)] \sim \frac{1}{t}J_0(r\sqrt{\frac{\beta_2-\beta_1}{D}}) + o(\frac{1}{t^2}) \tag{A.37}$$

Similarly, we can compute that

$$\begin{aligned} & 2i\int_{-\beta_2}^{-\beta_1} \mathrm{Im}[U_1(xe^{\pi i})]e^{tx}dx \\ = \; & i\pi\frac{1}{t}[\exp(-\frac{r^2}{4Dt}-\beta_1 t) - \exp(-\frac{r^2}{4Dt}-\beta_2 t)] \end{aligned} \tag{A.38}$$

By combining the above results we get a final expression for the cAMP concentration in Region 1:

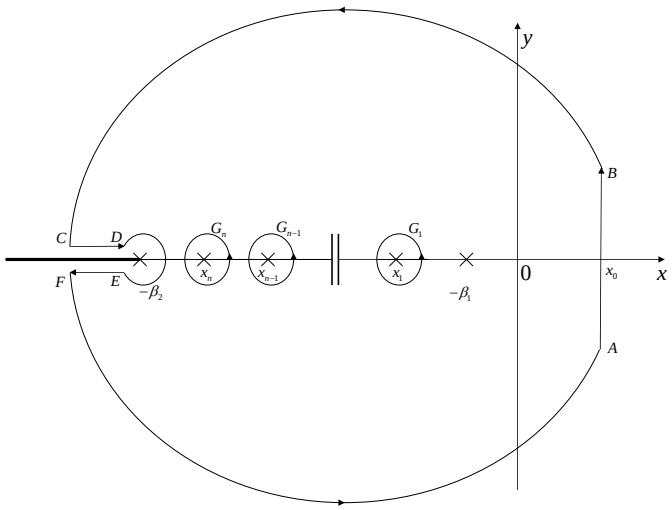

Figure A.2: The contour used to invert the Laplace transform in region 2.

$$
\begin{aligned}
C_1(r,t) &= \frac{F}{\pi D}\sum_{j=1}^{n}\frac{N_1(x_j)}{N'(x_j)} I_0(r\gamma_1(x_j))\exp(x_j t) + \frac{F}{2\pi D t}\exp(-\frac{r^2}{4Dt} - \beta_2 t) \\
&\quad -\frac{F}{2\pi D}\mathcal{L}[F_1(r,s)]\exp(-\beta_2 t) \qquad \text{(A.39)} \\
&\sim \frac{F}{\pi D}\sum_{j=1}^{n}\frac{N_1(x_j)}{N'(x_j)} I_0(r\gamma_1(x_j))\exp(x_j t) + \frac{F}{2\pi D t}\exp(-\frac{r^2}{4Dt} - \beta_2 t) \\
&\quad -\frac{F}{2\pi D t} J_0(r\sqrt{\frac{\beta_2-\beta_1}{D}})\exp(-\beta_2 t) + o(\frac{1}{t^2})\exp(-\beta_2 t) \qquad \text{(A.40)}
\end{aligned}
$$

A.2 Region 2

To obtain a solution in the second region, we again use contour integration of s in the complex plane as shown in Figure A.2. Since $U_2(s)$ has the same denominator as $U_1(s)$, $U_2(s)$ has the same simple poles $x_j \in (-\beta_2,-\beta_1)$ $(j = 1, 2, \cdots, n)$. After some algebra, we find the branch cut of $U_2(s)$ is along the negative axis of s-plane starting from $-\beta_2$, *i.e.* $(-\infty, -\beta_2]$ (see Figure A.2). Since the contribution along the arcs BC, FA, and DE, vanish in the limit $|z| \to \infty$ we find

$$u_2(r,t) = -\frac{1}{2\pi i}\int_{CD+EF} U_2(z)e^{tz}dz + \sum_{j=1}^{n} res[U_2(z)e^{tz}, x_j] \quad (A.41)$$

where

$$res[U_2(z)e^{tz}, x_j] = \frac{K_0(r\gamma_2(x_j))}{N'(x_j)}e^{x_j t} = \frac{K_0(r\sqrt{\frac{x_j+\beta_2}{D}})}{N'(x_j)}e^{x_j t} \quad (A.42)$$

For the branch cut integrals, we have along the CD $z = xe^{\pi i}$ and $dz = e^{\pi i}dx$, while along EF we have $z = xe^{-\pi i}$ and $dz = e^{-\pi i}dx$, so that

$$\begin{aligned}\int_{CD+EF} U_2(z)e^{tz}dz &= \int_{-\infty}^{-\beta_2} U_2(xe^{\pi i})e^{tx}dx - \int_{-\infty}^{-\beta_2} U_2(xe^{-\pi i})e^{tx}dx \\ &= \int_{-\infty}^{-\beta_2} [U_2(xe^{\pi i}) - U_2(xe^{-\pi i})]e^{tx}dx \\ &= 2i\int_{-\infty}^{-\beta_2} \mathrm{Im}[U_2(xe^{\pi i})]e^{tx}dx \end{aligned} \quad (A.43)$$

The nominator $K_0(r\gamma_2)$ can be expressed in terms of a real and imaginary part by the using the properties of Bessel functions

$$K_0(r\gamma_2(xe^{\pm\pi i})) = -\frac{\pi}{2}[Y_0(r\gamma_2^*(x)) \pm iJ_0(r\gamma_2^*(x))],\ x \in (-\infty, -\beta_2) \quad (A.44)$$

Thus,

$$\begin{aligned}\int_{CD+EF} U_2(z)e^{tz}dz &= 2i\int_{-\infty}^{-\beta_2} \frac{QY_0(r\gamma_2^*) - PJ_0(r\gamma_2^*)}{P^2+Q^2}e^{tx}dx \\ \overset{x=-s-\beta_2}{=} 2ie^{-\beta_2 t}\int_0^{\infty} F_2(r,s)e^{-ts}ds &= 2ie^{-\beta_2 t}\mathcal{L}[F_2(r,s)] \end{aligned} \quad (A.45)$$

where

$$F_2(r,s) = \frac{Q(-s-\beta_2)Y_0(r\sqrt{\frac{s}{D}}) - P(-s-\beta_2)J_0(r\sqrt{\frac{s}{D}})}{P^2(-s-\beta_2) + Q^2(-s-\beta_2)} \quad (A.46)$$

By expanding $\mathcal{L}[F_2(r,s)]$ in powers of $\frac{1}{t}$ as above, we obtain

$$\begin{aligned}\mathcal{L}[F_2(r,s)] &= -\sum_{n=1}^{\infty}\frac{1}{t^n}F_2^{(n-1)}(r,s)e^{-ts}|_{s=0}^{s=\infty} \\ &\sim 0+o(\frac{1}{t^2}) \end{aligned} \tag{A.47}$$

After some algebra, we find a final solution for the the concentration of cAMP in Region 2

$$C_2(r,t)=\frac{F}{\pi DR}\sum_{j=1}^{n}\frac{K_0(r\sqrt{\frac{x_j+\beta_2}{D}})}{N'(x_j)}\exp(x_jt)-\frac{F}{\pi DR}\frac{\mathcal{L}[F_2(r,s)]}{\pi}\exp(-\beta_2 t) \tag{A.48}$$

$$\sim \frac{F}{\pi DR}\sum_{j=1}^{n}\frac{K_0(r\sqrt{\frac{x_j+\beta_2}{D}})}{N'(x_j)}\exp(x_jt)+o(\frac{1}{t^2})\exp(-\beta_2 t) \tag{A.49}$$

Appendix B

Proof of equation (2.43)

Here, we will present a proof of the last identity in Eqn.(2.43):

$$\lim_{\theta_0 \to 0} \int_{-\theta_0}^{\theta_0} R c_1(R,\theta) d\theta = 0.$$

From Eqn.(2.27) with the left hand side set to zero and the boundary condition Eqn.(2.44), we can obtain the general solution for c_1 at the junction $-\theta_0 < \theta < \theta_0$

$$\begin{aligned} c_1(R,\theta) &= [\frac{f}{\sqrt{\beta D}} + \frac{1}{2\pi}\frac{J}{\sqrt{\beta D}R}]\frac{I_0(R/l)}{I_0'(R/l)} \\ &+ \frac{1}{\pi}\frac{f}{D}\sum_{n=1}^{\infty}\frac{I_n(R/l)}{(R/l)I_n'(R/l)}\cos n\theta, \end{aligned} \tag{B.1}$$

where J is an unknown constant. The first term of $c_1(R,\theta)$ is independent of θ, so the limit of the first term's integration gives zero. Thus, we need to prove $\lim_{\theta_0 \to 0} Q(\theta_0) = 0$, where $Q(\theta_0) = \int_{-\theta_0}^{\theta_0} \sum_{n=1}^{\infty} \frac{I_n(R/l)}{(R/l)I_n'(R/l)} \cos n\theta d\theta$. Since we can not change the order of the integral with the infinite summation, we will find the upper and lower bound of $Q(\theta_0)$ instead. It is easy to show that for positive arguments x

$$\frac{n+1}{n(n+1)+\frac{x^2}{2}} < \frac{I_n(x)}{xI_n'(x)} < \frac{1}{n}, n = 1,2,3,... \tag{B.2}$$

Thus, we have

$$
\begin{aligned}
|\frac{I_n(x)}{xI_n'(x)}\cos n\theta - \frac{\cos n\theta}{n}| &\leq |\frac{I_n(x)}{xI_n'(x)} - \frac{1}{n}||\cos n\theta| \\
&\leq |\frac{I_n(x)}{xI_n'(x)} - \frac{1}{n}| \\
&= \frac{1}{n} - \frac{I_n(x)}{xI_n'(x)} \\
&< \frac{1}{n} - \frac{n+1}{n(n+1)+\frac{x^2}{2}} \\
&= \frac{x^2}{2}\frac{1}{(n+1)n^2+\frac{x^2}{2}n} \\
&< \frac{x^2}{2}\frac{1}{(n+1)n^2}. \qquad \text{(B.3)}
\end{aligned}
$$

Therefore, for each n, $\frac{I_n(x)}{xI_n'(x)}\cos n\theta$ is bounded as follows

$$
\begin{aligned}
\frac{\cos n\theta}{n} - \frac{x^2}{2}\frac{1}{(n+1)n^2} &< \frac{I_n(x)}{xI_n'(x)}\cos n\theta \\
&< \frac{\cos n\theta}{n} + \frac{x^2}{2}\frac{1}{(n+1)n^2}. \qquad \text{(B.4)}
\end{aligned}
$$

Thus, the upper and lower bound of the infinite summation is given by

$$
\begin{aligned}
&\sum_{n=1}^{\infty}\frac{\cos n\theta}{n} \pm \frac{1}{2}(\frac{R}{l})^2\sum_{n=1}^{\infty}\frac{1}{(n+1)n^2} \\
&= \frac{1}{2}\log\frac{1}{2-2\cos\theta} \pm \frac{1}{2}(\frac{R}{l})^2(\frac{\pi^2}{6}-1). \qquad \text{(B.5)}
\end{aligned}
$$

By integrating Eqn.(B.5) from $-\theta_0$ to θ_0, we find the upper and lower bound of $Q(\theta_0)$

$$
\begin{aligned}
&i[Li_2(e^{-i\theta_0}) - Li_2(e^{i\theta_0})] - (\frac{R}{l})^2(\frac{\pi^2}{6}-1)\theta_0 < Q(\theta_0) \\
&< i[Li_2(e^{-i\theta_0}) - Li_2(e^{i\theta_0})] + (\frac{R}{l})^2(\frac{\pi^2}{6}-1)\theta_0, \qquad \text{(B.6)}
\end{aligned}
$$

where Li_2 denotes the dilogarithm function. Taking the limit of $\theta_0 \to 0$ in Eqn.(B.6), both the lower and upper bound go to zero, so that $\lim_{\theta_0\to 0} Q(\theta_0) = 0$ and, hence, $\lim_{\theta_0\to 0}\int_{-\theta_0}^{\theta_0} Rc_1(R,\theta)d\theta = 0$.

Appendix C

3D model of cAMP distribution

The analytic solutions found in two dimensions can be extended to three dimensional geometry. By rotating FIG. 2.5 around the x-axis, we can arrive at a 3D model with the cell body as a sphere with radius R, and the dendrite as a cylinder with length L and radius w. Since the dendrite is very thin compared to the soma, *i.e.* $w \ll R$, Eqn.(2.26) remains valid. The concentration in the sphere, $\hat{C}_1(r, \theta, \varphi)$, and in the cylinder, $\hat{C}_2(x, \rho, \varphi)$, obey the diffusion equation with a homogeneous degradation rate β as in Eqn.(2.27,2.28), but now written in. n spherical and cylinder coordinate, respectively, where $0 \leq r \leq R$, $0 \leq \theta \leq \pi$, $0 \leq x \leq L$, $0 \leq \rho \leq w$ and $0 \leq \varphi \leq 2\pi$. Because of the symmetry around x-axis, both concentration fields are independent of φ and they become effectively two dimensional: $\hat{C}_1(r, \theta, \varphi) = \hat{C}_1(r, \theta)$ and $\hat{C}_2(x, \rho, \varphi) = \hat{C}_2(x, \rho)$.

In the 3D case, the constant cAMP source flux, F, has units of $1/(s\mu m^2)$, and the boundary conditions read

$$\frac{\partial \hat{C}_1(R, \theta)}{\partial r} = \frac{F}{D}, (\theta_0 \leq \theta \leq \pi, 0 \leq \varphi \leq 2\pi) \tag{C.1}$$

$$\frac{\partial \hat{C}_2(L, \rho)}{\partial x} = \frac{F}{D}, (0 \leq \rho \leq w, 0 \leq \varphi \leq 2\pi) \tag{C.2}$$

$$\frac{\partial \hat{C}_2(x, w)}{\partial \rho} = \frac{F}{D}, (0 \leq x \leq L, 0 \leq \varphi \leq 2\pi). \tag{C.3}$$

Since $w \ll R$, we can approximate the junction of the sphere and the cylinder to be a disk, and we require that the concentration and gradient at the

dist to be continuous

$$\hat{C}_1(R,\theta) = \hat{C}_2(0,\rho), (0 \le \theta < \theta_0, 0 \le \varphi \le 2\pi) \tag{C.4}$$

$$\frac{\partial \hat{C}_1(R,\theta)}{\partial r} = \frac{\partial \hat{C}_2(0,\rho)}{\partial x}, (0 \le \theta < \theta_0, 0 \le \varphi \le 2\pi) \tag{C.5}$$

where $\rho \simeq R\theta$.

Therefore, the steady state solution can be obtained as

$$\begin{aligned} \hat{C}_1(r,\theta) &= \sum_{m=0}^{\infty} \hat{B}_m \frac{i_m(r/l)}{i'_m(R/l)} p_m(\cos\theta) \\ &+ \frac{F}{\sqrt{\beta D}} \frac{1+\cos\theta_0}{2} \frac{i_0(r/l)}{i'_0(R/l)} \\ &+ \sum_{n=1}^{\infty} \frac{F}{\sqrt{\beta D}} \frac{1}{2} [p_{n+1}(\cos\theta_0) \\ &- p_{n-1}(\cos\theta_0)] \frac{i_n(r/l)}{i'_n(R/l)} p_n(\cos\theta), \end{aligned} \tag{C.6}$$

$$\begin{aligned} \hat{C}_2(x,\rho) &= \sum_{n=0}^{\infty} \hat{A}_n [e^{x\sqrt{(\frac{1}{l})^2+k_n^2}} \\ &+ e^{(2L-x)\sqrt{(\frac{1}{l})^2+k_n^2}}] J_0(k_n\rho) \\ &+ \frac{F}{\sqrt{\beta D}} \frac{\cosh(x/l)}{\sinh(L/l)} + \frac{F}{\sqrt{\beta D}} \frac{I_0(\rho/l)}{I'_0(w/l)}, \end{aligned} \tag{C.7}$$

where i_n and J_n represent the modified spherical Bessel function of the first kind and Bessel function of the first kind respectively, k_n is the n-th root of $J_1(k_n w) = 0$, and P_n^m denotes the Legendre function. Here $p_n = P_n^0$. The coefficients $\hat{B}_m$ are determined by $\hat{A}_n$ through Eqn.(C.5),

$$\hat{B}_m = \frac{2m+1}{2} l \int_0^{\theta_0} \hat{g}(\theta) p_m(\cos\theta) \sin\theta d\theta, m = 0, 1, 2, ... \tag{C.8}$$

where $\hat{g}(\theta)$ is the flux from the dendrite to the soma, given by

$$\begin{aligned} \hat{g}(\theta) &= \frac{\partial \hat{C}_2(0,\rho)}{\partial x} = \sum_{n=0}^{\infty} \hat{A}_n \sqrt{(\frac{1}{l})^2 + k_n^2} [1 \\ &- e^{2L\sqrt{(\frac{1}{l})^2+k_n^2}}] J_0(k_n\rho). \end{aligned} \tag{C.9}$$

To determine $\hat{A}_n$, one needs to solve Eq.(C.4), which is a difficult task.

Similarly to out two dimensional case, we can consider the limiting case $w = \theta_0 = 0$, *i.e.* a sphere connected to a line. We use $\hat{c}_{1,2}$ to represent the concentrations for this limit case, which can be related to $\hat{C}_{1,2}$ as follows

$$\hat{c}_1(r,\theta) = \lim_{\theta_0 \to 0} \hat{C}_1(r,\theta), \tag{C.10}$$

$$\hat{c}_2(x) = \lim_{w \to 0} \int_0^{2\pi} \int_0^w \hat{C}_2(x,\rho) d\rho d\varphi. \tag{C.11}$$

The diffusion equation and boundary condition for $\hat{c}_1$ are identical to Eqn.(2.27) and Eqn.(C.1) while the diffusion equation for $\hat{c}_2$ becomes one dimensional:

$$0 = D\frac{d^2\hat{c}_2}{dx^2} - \beta\hat{c}_2 + 2f, \tag{C.12}$$

where $f = \pi w F$.

The boundary condition is

$$\begin{aligned} \frac{d\hat{c}_2(L)}{dx} &= \lim_{w \to 0} \int_0^{2\pi} \int_0^w \frac{F}{D} \rho d\rho d\varphi \\ &= \lim_{w \to 0} \int_0^{2\pi} \int_0^w \frac{f}{\pi w D} \rho d\rho d\varphi = 0. \end{aligned} \tag{C.13}$$

and the continuity property at the junction reduces to

$$\begin{aligned} \hat{c}_2(0) &= \lim_{\theta_0 \to 0} \int_0^{2\pi} \int_0^{\theta_0} R^2 \sin\theta \hat{c}_1(R,\theta) d\theta d\varphi \\ &= 0, \end{aligned} \tag{C.14}$$

$$\frac{\partial \hat{c}_1(R)}{\partial r} = \frac{f}{\pi w D} + \frac{J}{DR^2}\delta^2(\theta,\varphi), \tag{C.15}$$

$$\frac{d\hat{c}_2(0)}{dx} = \frac{J}{D}, \tag{C.16}$$

where $\delta^2(\theta,\varphi)$ denotes the Dirac delta function in spherical coordinates. Solving the above equations leads to an analytic solution

$$J = 2fl\tanh(L/l), \tag{C.17}$$

$$\hat{c}_1(r,\theta) = \frac{f}{\beta R^2}\frac{\tanh(L/l)}{\pi}\sum_{n=0}^{\infty}(2n+1)\frac{i_n(r/l)}{i'_n(R/l)}p_n(\theta) + \frac{f}{\pi w\sqrt{\beta D}}\frac{i_0(r/l)}{i'_0(R/l)}, \tag{C.18}$$

$$\hat{c}_2(x) = \frac{2f}{\beta} - \frac{2f}{\beta}\frac{e^{x/l}}{1+e^{2L/l}} - \frac{2f}{\beta}\frac{e^{(2L-x)/l}}{1+e^{2L/l}}. \tag{C.19}$$

Comparing the coefficients of $\hat{c}_{1,2}$ and $\hat{C}_{1,2}$ through Eqn.(C.10, C.11), we find

$$\hat{A}_0 = -\frac{F}{\beta w}\frac{1}{1+e^{2L/l}}, \tag{C.20}$$

$$\hat{B}_m = (2m+1)\frac{\pi w F}{\beta R^2}\tanh(L/l) + o(w^2), \quad m = 0, 1, 2, ... \tag{C.21}$$

Therefore, we can obtain an approximate form for the concentration in the soma

$$\hat{C}_1(r,\theta) = \frac{\pi w F}{\beta R^2}\tanh(L/l)\sum_{n=0}^{\infty}(2n+1)\frac{i_n(r/l)}{i'_n(R/l)}p_n(\cos\theta) + \frac{F}{2\sqrt{\beta D}}\sum_{n=1}^{\infty}[p_{n+1}(\cos\theta_0) - p_{n-1}(\cos\theta_0)]\frac{i_n(r/l)}{i'_n(R/l)}p_n(\cos\theta) + \frac{F}{\sqrt{\beta D}}\frac{1+\cos\theta_0}{2}\frac{i_0(r/l)}{i'_0(R/l)} + o(w^2), \tag{C.22}$$

and in the dendrite

$$\hat{C}_2(x,0) = \frac{F}{\sqrt{\beta D}}\frac{\cosh(x/l)}{\sinh(L/l)} + \frac{F}{\sqrt{\beta D}}\frac{1}{I'_0(w/l)} - \frac{F}{\beta w}\frac{\cosh((L-x)/l)}{\cosh(L/l)} + o(\frac{1}{w}). \tag{C.23}$$

Furthermore the gradient at the junction reads in this limit

$$\frac{\partial \hat{C}_2(0,0)}{\partial x} = \frac{F}{w\sqrt{\beta D}} \tanh(L/l) + o(\frac{1}{w}), \tag{C.24}$$

similar in form to the two dimensional case.

Appendix D

Calculation of mutual information

D.1 External Mutual Information

We start with the definition of the mutual information for two continuous random variables U and V [54]:

$$I(U;V) = \int p(u,v) \log \frac{p(u,v)}{p(u)p(v)} dudv \tag{D.1}$$

where $p(u,v)$ is the joint probability density function of U and V and where $p(u)$ and $p(v)$ are the marginal probability density functions of U and V respectively. It can be shown that $I(U;V) \geq 0$ and that $I(U;V) = 0$ if U and V are independent random variables. The mutual information can also be expressed in terms of the differential entropy for U and V, $H(U)$ and $H(U)$, and the conditional differential entropy $H(U|V)$: $I(U;V) = I(V;U) = H(U) - H(U|V)$, where the entropies can be calculated as

$$H(U) = -\int p(u) \log p(u) du \tag{D.2}$$

$$H(U|V) = -\int p(u,v) \log p(u|v) dudv \tag{D.3}$$

Finally, if U is a n-dimensional vector with density function $p(u_1, \cdots, u_n)$, then the differential entropy for U can be expressed as

$$H(U) = -p(u_1, ..., u_n) \log p(u_1, ..., u_n) du_1 \cdots du_n \tag{D.4}$$

with equivalent expression for $H(V)$ and $H(U|V)$.

To derive an expression for the external mutual information between the direction of the gradient θ_s and the resulting distribution of bound receptors Y, $I(Y; \theta_s)$, we take a circular disk-shaped cell with diameter L and divide the membrane in n sectors θ_i, $i \in \{1, 2, \cdots, n\}$. We assume that receptors in each sector interact independently and the fraction of bound receptors on the membrane is a n-dimensional vector $Y = (y_1, y_2, \cdots, y_n)^T$, with each element y_i is the binding fraction at sector i. We will assume that the cells are unpolarized, i.e., they are newly introduced to a gradient and have no prior asymmetry. Thus, the gradient angle θ_s is uniformly distributed and

$$p(\theta_s) = \frac{1}{2\pi}, \tag{D.5}$$

The remaining probability density functions depends on the shape of the chemoattractant profile.

D.1.1 Exponential Gradient

In our experiments, an exponential gradient of the chemoattractant is produced by microfluidic device such that difference in concentration across a fixed length is proportional to the local concentration: $C_{local}(x) = C_0 e^{\frac{p}{L}x}$, where p is the gradient steepness. Thus, the concentration in the vicinity of sector θ_i, $i \in \{1, 2, \cdots, n\}$, can be expressed as

$$C_i = C_0 \cdot e^{-p \cos(\theta_i - \theta_s)/2}. \tag{D.6}$$

During the experiments, the cells are exposed to a steady state gradient and we can assume that the ligand binding has reached equilibrium. Thus, given the gradient direction θ_s, the conditional probability distribution of binding fraction y_i at sector i is normal [64] with mean

$$\mu_i(\theta_s) = \frac{C_i}{K_d + C_i}, \tag{D.7}$$

and variance

$$\sigma_i^2(\theta_s) = \frac{K_d C_i}{N_i(K_d + C_i)^2}, \tag{D.8}$$

where K_d is the ligand-receptor binding dissociation constant and N_i is the number of receptor in sector i. Therefore, the conditional probability distribution of binding fraction vector Y is n-dimensional normal distribution $N_n(\mu, K)$. Since we assumed that the sectors are independent, the mean vector is

$$\mu(\theta_s) = (\mu_1, \cdots, \mu_n)^T, \tag{D.9}$$

and the covariance matrix is

$$K(\theta_s) = \begin{pmatrix} \sigma_i^2 & 0 & 0 \\ 0 & \ddots & 0 \\ 0 & 0 & \sigma_n^2 \end{pmatrix} \tag{D.10}$$

It follows that

$$p(Y|\theta_s) = \frac{1}{(\sqrt{2\pi})^n |K(\theta_s)|^{\frac{1}{2}}} \exp[-\frac{1}{2}(Y - \mu(\theta_s))^T K^{-1}(Y - \mu(\theta_s))]. \tag{D.11}$$

By Bayes Theorem, $p(Y, \theta_s)$ and $p(Y)$ can be calculated as follows

$$p(Y, \theta_s) = p(\theta_s)p(Y|\theta_s), \tag{D.12}$$

$$p(Y) = \int p(Y|\theta_s)p(\theta_s)d\theta_s. \tag{D.13}$$

We can now derive expressions for the conditional entropy

$$
\begin{aligned}
H(Y|\theta_s) &= -\int\int p(Y,\theta_s)\log p(Y|\theta_s)dY\,d\theta_s && \text{(D.14)}\\
&= \int p(\theta_s)[-\int p(Y|\theta_s)\log p(Y|\theta_s)dY]d\theta_s && \text{(D.15)}\\
&= \int p(\theta_s)[\frac{1}{2}\log[(2\pi e)^n|K(\theta_s)|]d\theta_s && \text{(D.16)}\\
&= \frac{1}{2}\log(2\pi e)^n + \frac{1}{2\pi}\int \log|K(\theta_s)|^{\frac{1}{2}}d\theta_s && \text{(D.17)}\\
&= \frac{1}{2}\log(2\pi e)^n + \frac{1}{2\pi}\int \frac{1}{2}\log\prod_{i=1}^{n}\sigma_i^2 d\theta_s, && \text{(D.18)}
\end{aligned}
$$

where the derivation of Eq.D.16 can be found in Ref. [54]. Furthermore, the marginal entropy can be found as:

$$
\begin{aligned}
H(Y) &= -\int p(Y)\log p(Y)dY && \text{(D.19)}\\
&= -\int\int p(\theta_s)p(Y|\theta_s)\log[\int p(Y|\theta_s')p(\theta_s')d\theta_s']dY\,d\theta_s && \text{(D.20)}\\
&= -\frac{1}{2\pi}\int\int p(Y|\theta_s)\log f(Y)dY\,d\theta_s + \log 2\pi, && \text{(D.21)}
\end{aligned}
$$

where

$$
\begin{aligned}
f(Y) &= \int p(Y|\theta_s)d\theta_s && \text{(D.22)}\\
&= \int \frac{1}{(\sqrt{2\pi})^n\prod_{i=1}^{n}\sigma_i(\theta_s)}\prod_{i=1}^{n}\exp[-\frac{(y_i-\mu_i(\theta_s))^2}{2\sigma_i^2(\theta_s)}]d\theta_s. && \text{(D.23)}
\end{aligned}
$$

These equations simplify for the case of a shallow gradient, *i.e.* $p/L << 1$. The mean binding fraction in each sector can then be expanded in powers of p as

$$
\begin{aligned}
\mu_i(\theta_s) &= \frac{C_0\cdot e^{-p\cos(\theta_i-\theta_s)/2}}{K_d + C_0\cdot e^{-p\cos(\theta_i-\theta_s)/2}} && \text{(D.24)}\\
&= \frac{C_0}{K_d+C_0} - \frac{C_0K_d}{(K_d+C_0)^2}\cos(\theta_i-\theta_s)p && \text{(D.25)}\\
&\quad -\frac{C_0K_d(C_0-K_d)}{2(K_d+C_0)^3}(\cos(\theta_i-\theta_s)p)^2 + o(p^3), && \text{(D.26)}
\end{aligned}
$$

The sector variance can also be simplified by noting the factor $N_i(>> 1)$ in the denominator of Eq.D.8. Thus, the dependence on p is weaker than the mean dependence on p and, for simplicity, we can treat $\sigma_i^2(\theta_s)$ be independent of θ_s: $\sigma_i^2(\theta_s) = \sigma_i^2$. This leads to a simplification of Eq.D.22:

$$f(Y) = \frac{1}{(\sqrt{2\pi})^n \prod_{i=1}^{n} \sigma_i} \int \prod_{i=1}^{n} \exp[-\frac{(y_i - \mu_i(\theta_s))^2}{2\sigma_i^2}] d\theta_s. \tag{D.27}$$

Next, we expand $(y_i - \mu_i(\theta_s))^2$ in terms of powers of p:

$$(y_i - \mu_i(\theta_s))^2 = A_i^2 + 2A_iB \cdot \cos(\theta_i - \theta_s)p + B(A_ib + B)(\cos(\theta_i - \theta_s)p)^2 + o(p^3) \tag{D.28}$$

where

$$A_i = y_i - \frac{C_0}{K_d + C_0}, \tag{D.29}$$

$$B = \frac{C_0 K_d}{(K_d + C_0)^2}, \tag{D.30}$$

$$b = \frac{C_0 - K_d}{K_d + C_0}. \tag{D.31}$$

Thus we can expand $\prod_{i=1}^{n} \exp[-\frac{(y_i - \mu_i(\theta_s))^2}{2\sigma_i^2}]$ in terms of powers of p:

$$\begin{aligned} \prod_{i=1}^{n} \exp[-\frac{(y_i - \mu_i(\theta_s))^2}{2\sigma_i^2}] \;=\; & [\prod_{i=1}^{n} \exp(-\frac{A_i^2}{2\sigma_i^2})][1 - \sum_{i=1}^{n} \frac{A_iB}{\sigma_i^2} \cos(\theta_i - \theta_s)p \\ & + \frac{1}{2} \sum_{i=1}^{n} (\frac{A_i^2 B^2}{\sigma_i^4} - \frac{B(B + A_ib)}{\sigma_i^2})(\cos(\theta_i - \theta_s)p)^2 \\ & + \frac{1}{2} \sum_{i \neq j} \frac{A_iA_jB^2}{\sigma_i^2 \sigma_j^2} \cos(\theta_i - \theta_s) \cos(\theta_j - \theta_s)p^2 \\ & + o(p^3)]. \end{aligned} \tag{D.32}$$

After performing the integration, we find

$$f(Y) = \frac{\prod_{i=1}^{n} \exp(-\frac{A_i^2}{2\sigma_i^2})}{(\sqrt{2\pi})^n \prod_{i=1}^{n} \sigma_i} \{2\pi + \frac{\pi}{2} p^2 [\sum_{i=1}^{n} (\frac{A_i^2 B^2}{\sigma_i^4} - \frac{B(B + A_i b)}{\sigma_i^2}) + \sum_{i \neq j} \frac{A_i A_j B^2}{\sigma_i^2 \sigma_j^2} \cos(\theta_i - \theta_j)] + o(p^3)\},$$

which gives

$$\begin{aligned} \log f(Y) &= \log 2\pi - \frac{1}{2} \log(2\pi)^n - \frac{1}{2} \log \prod_{i=1}^{n} \sigma_i^2 - \sum_{i=1}^{n} \frac{A_i^2}{2\sigma_i^2} + \\ & [\sum_{i=1}^{n} (\frac{A_i^2 B^2}{\sigma_i^4} - \frac{B(B + A_i b)}{\sigma_i^2}) + \sum_{i \neq j} \frac{A_i A_j B^2}{\sigma_i^2 \sigma_j^2} \cos(\theta_i - \theta_j)] \frac{p^2}{4} + o(p^3). \end{aligned}$$

As Eq.D.21 shows, an estimate of $H(Y)$ for small p, requires to calculate the following equation:

$$\begin{aligned} \langle \log f(Y) \rangle &= \int p(Y|\theta_s) \log f(Y) dY \\ &= \log 2\pi - \frac{1}{2} \log(2\pi)^n - \frac{1}{2} \log \prod_{i=1}^{n} \sigma_i^2 - \sum_{i=1}^{n} \frac{\langle A_i^2 \rangle}{2\sigma_i^2} \\ &\quad + [\sum_{i=1}^{n} (\frac{B^2 \langle A_i^2 \rangle}{\sigma_i^4} - \frac{Bb \langle A_i \rangle}{\sigma_i^2} - \frac{B^2}{\sigma_i^2}) \\ &\quad + \sum_{i \neq j} \frac{B^2 \langle A_i A_j \rangle}{\sigma_i^2 \sigma_j^2} \cos(\theta_i - \theta_j)] \frac{p^2}{4} + o(p^3), \end{aligned} \tag{D.33}$$

where

$$\begin{aligned} \langle A_i \rangle &= \left\langle y_i - \frac{C_0}{K_d + C_0} \right\rangle \\ &= \mu_i - \frac{C_0}{K_d + C_0} \\ &= -B \cos(\theta_i - \theta_s) p - bB(\cos(\theta_i - \theta_s) p)^2, \end{aligned} \tag{D.34}$$

$$\left\langle A_i^2 \right\rangle = \sigma_i^2 + B^2 (\cos(\theta_i - \theta_s) p)^2 + o(p^3), \tag{D.35}$$

$$\langle A_i A_j \rangle = B^2 \cos(\theta_i - \theta_s) \cos(\theta_j - \theta_s) p^2 + o(p^3). \tag{D.36}$$

Thus,

$$\langle \log f(Y) \rangle = \log 2\pi - \frac{1}{2} \log(2\pi e)^n - \frac{1}{2} \log \prod_{i=1}^{n} \sigma_i^2 - \frac{B^2 p^2}{2} \sum_{i=1}^{n} \frac{\cos^2(\theta_i - \theta_s)}{\sigma_i^2} + o(p^3).$$

By integrating $\langle \log f(Y) \rangle$ over θ_s, we arrive at an estimate for $H(Y)$:

$$H(Y) = \frac{1}{2} \log(2\pi e)^n + \frac{1}{2\pi} \int \frac{1}{2} \log \prod_{i=1}^{n} \sigma_i^2 d\theta_s + \frac{B^2 p^2}{4} \sum_{i=1}^{n} \frac{1}{\sigma_i^2} + o(p^3). \tag{D.37}$$

Hence, for small p, the mutual information between Y and θ_s is

$$\begin{aligned} I(Y;\theta_s) &= H(Y) - H(Y|\theta_s) \\ &= \frac{B^2 p^2}{4} \sum_{i=1}^{n} \frac{1}{\sigma_i^2} + o(p^3) \\ &= \frac{(K_d C_0 p)^2}{4(K_d + C_0)^4} \sum_{i=1}^{n} \frac{1}{\sigma_i^2} + o(p^3). \end{aligned} \tag{D.38}$$

Following our assumption that σ_i^2 is independent of θ_i and that every sector has the same number of receptors, we have

$$\sigma_i^2 \approx \frac{n K_d C_0}{N(K_d + C_0)^2}, \tag{D.39}$$

where N is the total number of receptors on the membrane. Finally, we arrive at the estimate for $p << 1$ for the external mutual information reported in the main text:

$$I(Y;\theta_s) \approx \frac{N K_d C_0 p^2}{4(K_d + C_0)^2} + o(p^3) \tag{D.40}$$

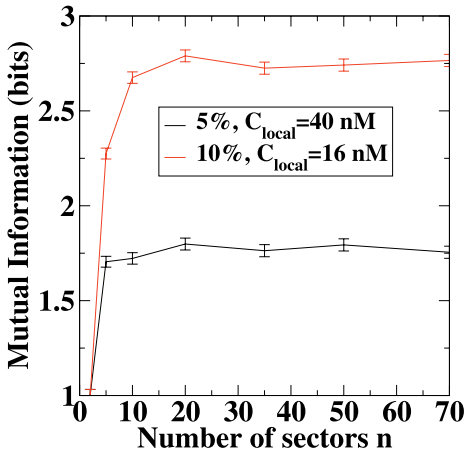

Figure D.1: The external mutual information as a function of the number of sectors for two different values of the gradient and local concentration. The parameters used are $K_d = 30nM$ and total number of receptors 70,000.

D.1.2 Linear Gradient

A similar analysis can be carried out for linear gradients in which the concentration profile has the form $C(x) = C_0 + \nabla C x$ where the gradient ∇C is constant throughout the device. Thus, the concentration of the chemoattractant in the vicinity of each sector is

$$C_i = C_0 + R\nabla C \cos(\theta_i - \theta_s). \tag{D.41}$$

Following the same general procedure as for the exponential gradient, we can derive an expression for the external mutual information $I(Y;\theta_s)$ for small gradients ($R \cdot \nabla C << K_d + C_0$:

$$I(Y;\theta_s) \approx \frac{NK_d}{4C_0}(\frac{R \cdot \nabla C}{K_d + C_0})^2 + o((\frac{R \cdot \nabla C}{K_d + C_0})^3). \tag{D.42}$$

D.1.3 Comparison between the numerical and analytical results

$I(Y;\theta_s)$ for exponential and linear gradient can only be approximated by Eq.D.40 and Eq.D.42 respectively when the gradient steepness is very small. For

steeper gradients, we can calculate $I(Y;\theta_s)$ numerically. The approximate equation derived above suggests that the mutual information may be independent of n as long as n is large enough to make the integral approximation reliable. To verify this, we have numerically evaluated the external mutual information as a function of n (Fig. D.1). The figure shows that the mutual information converges quickly when $n > 10$. Thus, in the following simulations the cell membrane is divided into $n = 36$, with a total membrane receptor number of $N = 70000$, $K_d = 30nM$ and $L = 10\mu m$. Importantly, just as the small p limit expression, the full numerical calculations peaks at $C_{local} = K_d$.

D.2 External and Internal Mutual Information

We will now derive an expression for the mutual information between the gradient direction and the motility direction θ_r, $I(\theta_r, \theta_s$. Since there is no internal bias during the downstream signaling process, the conditional probability $p(\theta_r|\theta_s)$ only depends on $\theta_r - \theta_s$ and the probability of the movement direction θ_r the cell will choose is identical, because the gradient angle θ_s is uniformly distributed:

$$p(\theta_r) = \int p(\theta_r|\theta_s)p(\theta_s)d\theta_s = \frac{1}{2\pi} \tag{D.43}$$

and

$$\begin{aligned} I(\theta_r, \theta_s) &= \int\int p(\theta_s)p(\theta_r|\theta_s)\log\frac{p(\theta_r|\theta_s)}{p(\theta_r)}d\theta_s d\theta_r & \text{(D.44)} \\ &= \log 2\pi + \int p(\theta_r|\theta_s)\log p(\theta_r|\theta_s)d\theta_r & \text{(D.45)} \\ &= \log 2\pi - h(\Theta_r) & \text{(D.46)} \end{aligned}$$

where

$$\begin{aligned} h(\Theta_r) &= -\int p(\theta_r|\theta_s)\log p(\theta_r|\theta_s)d\theta_r & \text{(D.47)} \\ &= -\int p(\theta_r|\theta_0)\log p(\theta_r|\theta_0)d\theta_r & \text{(D.48)} \end{aligned}$$

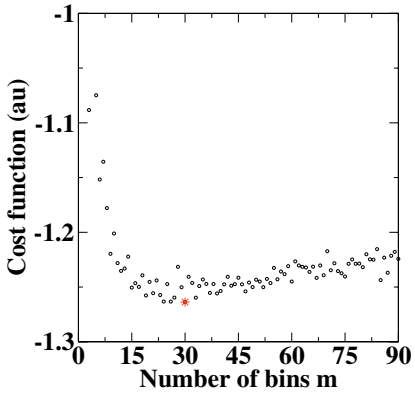

Figure D.2: The cost function as a function of the number of bins. The asterisk denotes the bin number ($m^* = 30$) that minimizes the cost function and that is selected to compute the mutual information for this particular value of the gradient $p = 7.5e-2$ and mean background concentration 8 nM.

where θ_0 is the gradient direction in experiment. The last step was carried out since $p(\theta_r|\theta_s)$ only depends on $\theta_r - \theta_s$. We choose $\theta_s = \theta_0$ because we can calculate each set of $p(\theta_r|\theta_0)$ for different gradients from the experiments.

A complication in our analysis is that $h(\Theta_r)$ is defined for a continuous probability distribution $p(\theta_r|\theta_0)$ while the results of the experiments are a set of discrete data. Thus, in order to calculate the probability distribution, we divide the range θ_r (*i.e.* $[0, 2\pi]$) into m bins of length $\Delta = \frac{2\pi}{m}$ and compute the number of angles in each bin P_j. Then, for an infinite amount of data points, we can calculate

$$h(\Theta_r^{\Delta})^{\infty} = -\sum_{j=1}^{m} P_j^{\infty} \log P_j^{\infty} \tag{D.49}$$

which can be shown to converge to the continuous quantity [54]

$$h(\Theta_r^{\Delta})^{\infty} + \log \Delta \to h(\Theta_r) \text{ as } \Delta \to 0 \tag{D.50}$$

leading to

$$I(\theta_r; \theta_s) = \sum_{j=1}^{m} P_j^{\infty} \log P_j^{\infty} + \log m \text{ as } m \to \infty \tag{D.51}$$

In reality, of course, we cannot make m arbitrarily large due to the limited

size of the data set. To circumvent this problem, we use a method proposed by Shimazaki and Shinomoto [60] to select the optimal number of bins m. This method uses a cost function defined that is minimized for the optimal m. This optimal number of bins needs to be computed for each data set, after which we can calculate the discrete entropy $h(\Theta_r^{\Delta})$ for finite sized data sets as An example of this procedure is shown in Fig. D.2 where we plot the value of the cost function as a function of the number of bins for a representative data set. For this particular data set, the cost function has a clear minimum at $m = m^*$.

$$h(\Theta_r^{\Delta}) = -\sum_{j=1}^{m} P_j \log P_j. \tag{D.52}$$

An estimate of the error in the above procedure was provided in Ref. [65] and is given by

$$\frac{m^* - 1}{2N_d} \tag{D.53}$$

where N_d denotes the number of data points. In conclusion, the external and internal mutual information $I(\theta_r; \theta_s)$ can be estimated by

$$I(\theta_r; \theta_s) = \sum_{j=1}^{m} P_j \log P_j + \log m^* \tag{D.54}$$

Bibliography

[1] D. M. Cooper, *Biochem J.*, **375**(Pt 3), 517 (2003).

[2] S. F. Steinberg, and L. L. Brunton, *Annu Rev. Pharmacol Toxicol*, **41**, 751 (2001).

[3] M. Zaccolo, and T. Pozzan, *Science*, **295**(5560), 1711 (2002).

[4] R. Fischmeister, L. R. Castro, A. Abi-Gerges, F. Rochais, J. Jurevicius, J. Leroy, and G. Vandecasteele, *Circ. Res.*, **99**(8), 816 (2006).

[5] V. O. Nikolaev, M. Bunemann, E. Schmitteckert, M. J. Lohse, and S. Engelhardt, *Circ. Res.*, **99**(10), 1084 (2006).

[6] J. Leroy, A. Abi-Gerges, V. O. Nikolaev, W. Richter, P. Lechene, J. L. Mazet, M. Conti, R. Fischmeister, and G. Vandecasteele, *Circ. Res.*, **102**(9), 1091 (2008).

[7] T. C. Rich, K. A. Fagan, T. E. Tse, J. Schaack, D. M. Cooper, and J. W. Karpen, *Proc Natl Acad Sci. U S A*, **98**(23), 13049 (2001).

[8] M. A. Davare, V. Avdonin, D. D. Hall, E. M. Peden, A. Burette, R. J. Weinberg, M. C. Horne, T. Hoshi, and J. W. Hell, *Science*, **293**(5527), 98 (2001).

[9] L. L. Brunton, J. S. Hayes, and S. E. Mayer, *Adv. Cyclic Nucleotide Res.*, **14**, 391 (1981).

[10] A. Terrin, G. D. Benedetto, V. Pertegato, Y. F. Cheung, G. Baillie, M. J. Lynch, N. Elvassore, A. Prinz, F. W. Herberg, M. D. Houslay, and M. Zaccolo, *J. Cell Biol.*, **175**(3), 441 (2006).

[11] M. Zaccolo, G. D. Benedetto, V. Lissandron, L. Mancuso, A. Terrin, and I. Zamparo, *Biochem Soc. Trans.*, **34**(Pt 4), 495 (2006).

[12] M. Mongillo, T. McSorley, S. Evellin, A. Sood, V. Lissandron, A. Terrin, E. Huston, A. Hannawacker, M. J. Lohse, T. Pozzan, M. D. Houslay, and M. Zaccolo, *Circ. Res.*, **95**(1), 67 (2004).

[13] M. Mongillo, C. G. Tocchetti, A. Terrin, V. Lissandron, Y. F. Cheung, W. R. Dostmann, T. Pozzan, D. A. Kass, N. Paolocci, M. D. Houslay, and M. Zaccolo, *Circ. Res.*, **98**(2), 226 (2006).

[14] W. Wong, and J. D. Scott, *Nat. Rev. Mol. Cell Biol.*, **5**(12), 959 (2004).

[15] J. J. Saucerman, L. L. Brunton, A. P. Michailova, and A. D. McCulloch, *J. Biol. Chem*, **278**(48), 47997 (2003).

[16] W. Xin, T. M. Tran, W. Richter, R. B. Clark, and T. C. Rich, *J. Gen. Physiol*, **131**(4), 349 (2008).

[17] S. R. Neves, P. Tsokas, A. Sarkar, E. A. Grace, P. Rangamani, S. M. Taubenfeld, C. M. Alberini, J. C. Schaff, R. D. Blitzer, I. I. Moraru, and R. Iyengar, *Cell*, **133**, 666 (2008).

[18] M. Abramowitz, and I. A. Stegun, *ninth dover printing, tenth gpo printing edn.*, **Dover, New York**, (1964).

[19] M. L. Reeves, B. K. Leigh, and P. J. England, *Biochem J.*, **241**(2), 535 (1987).

[20] D. C. Bode, J. R. Kanter, and L. L. Brunton, *Circ. Res.*, **68**(4), 1070 (1991).

[21] A. Takeuchi, S. Tatsumi, N. Sarai, K. Terashima, S. Matsuoka, and A. Noma, *J. Gen. Physiol*, **128**(5), 495 (2006).

[22] S. R. Post, R. Hilal-Dandan, K. Urasawa, L. L. Brunton, and P. A. Insel, *Biochem J.*, **311**(Pt 1), 75 (1995).

[23] J. A. Beavo, P. J. Bechtel, and E. G. Krebs, *Proc. Natl. Acad. Sci. U S A*, **71**(9), 3580 (1974).

[24] C. W. Dessauer, and A. G. Gilman, *J. Biol. Chem.*, **271**(28), 16967 (1996).

[25] T. C. Rich, K. A. Fagan, H. Nakata, J. Schaack, D. M. Cooper, and J. W. Karpen, *J. Gen. Physiol*, **116**(2), 147 (2000).

[26] J. J. Saucerman, J. Zhang, J. C. Martin, L. X. Peng, A. E. Stenbit, R. Y. Tsien, and A. D. McCulloch, *Proc. Natl. Acad. Sci. U S A*, **103**(34), 12923 (2006).

[27] I. L. Buxton, and L. L. Brunton, *J. Biol. Chem.*, **258**, 10233 (1983).

[28] M. Zaccolo, and T. Pozzan, *Science*, **295**, 1711 (2002).

[29] T. C. Rich, K. A. Fagan, T. E. Tse, J. Schaack, D. M. Cooper, and J. W. Karpen, *Proc. Natl. Acad. Sci.*, **98**, 13049 (2001).

[30] M. A. Davare, V. Avdonin, D. D. Hall, E. M. Peden, A. Burette, R. J. Weinberg, M. C. Horne, T. Hoshi, and J. W. Hell, *Science*, **293**, 98 (2001).

[31] W. Chen, H. Levine, and W. Rappel, *Phys. Biol.*, **5**, 1478 (2008).

[32] S. R. Neves, P. Tsokas, A. Sarkar, E. A. Grace, P. Rangamani, S. M. Taubenfeld, C. M. Alberini, J. C. Schaff, R. D. Blitzer, I. I. Moraru, and R. Iyengar, *Cell*, **133**, 666 (2008).

[33] T. C. Rainbow, B. Parsons, and B. B. Wolfe, *Proc. Natl. Acad. Sci. U S A*, **81**, 1585 (1984).

[34] G. E. Duncan, K. Y. Little, P. A. Koplas, J. A. Kirkman, G. R. Breese, and W. E. Stumpf, *Brain Res.*, **561**, 84 (1991).

[35] G. A Ordway, C. Gambarana, and A. Frazer, *J. Pharmacol. Exp. Ther.*, **247**, 379 (1988).

[36] O. D. Weiner, et al. *Nat. Cell Biol.*, **1**, 75 (1999).

[37] C. A. Parent, and P. N. Devreotes, *Science*, **284**, 765 (1999).

[38] J. Geiger, D. Wessels, D. R. Soll, *Cell Motil. Cytoskeleton*, **56**, 27 (2003).

[39] D. R. Soll, D. Wessels, P. J. Heid, H. Zhang, *J. Muscle Res. Cell Motil.*, **23**, 659 (2002).

[40] P. J. M. van Haastert, P. N. Devreotes, *Nat. Rev. Mol. Cell Biol.*, **5**, 626 (2004).

[41] P. G. Charest, R. A. Firtel, *Biochem J.*, **401**, 377 (2007).

[42] O. D. Weiner, et al., *PLoS Biol*, **4**, e38 (2006).

[43] L. Bosgraaf, P. J. van Haastert, *PLoS One*, **4**, e5253 (2009).

[44] L. Song, et al., *Eur. J. Cell Biol.*, **85**, 981 (2006).

[45] P. Herzmark, et al., *Proc. Natl. Acad. Sci. U S A*, **104**, 13349 (2007).

[46] P. N. Devreotes, and S. H. Zigmond, *Annu Rev. Cell Biol.*, **4**, 649 (1988).

[47] M. Ueda, Y. Sako, T. Tanaka, P. Devreotes, and T. Yanagida, *Science*, **294**, 864 (2001).

[48] J. Franca-Koh, Y. Kamimura, and P. Devreotes, *Curr. Opin. Genet. Dev.*, **16**, 333 (2006).

[49] K. Wang, W-J Rappel, R. Kerr, and H. Levine, *Phys. Rev. E*, **75**, 061905 (2007).

[50] W-J Rappel, and H. Levine, *Proc. Natl. Acad. Sci. U S A*, **105**, 19270 (2008).

[51] R. G. Endres, and N. S. Wingreen, *Proc. Natl. Acad. Sci. U S A*, **105**, 15749 (2008).

[52] H. C. Berg, and E. M. Purcell, *Biophys J.*, **20**, 193 (1977).

[53] W. Bialek, and S. Setayeshgar, *Proc. Natl. Acad. Sci. U S A*, **102**, 10040 (2005).

[54] T. M. Cover, and J. A. Thomas, *Wiley* **NewYork**, 2nd Ed. (2005).

[55] P. J. van Haastert, and M. Postma, *Biophys J.*, **93**, 1787 (2007).

[56] P. J. van Haastert, *J. Biol. Chem.*, **258**, 9643 (1983).

[57] B. W. Andrews, and P. A. Iglesias, *PLoS Comput. Biol.*, **3**(8), e153 (2007).

[58] Z. Xiao, N. Zhang, D. B. Murphy, and P. N. Devreotes, *J. Cell Biol.*, **139**, 365 (1997).

[59] T. Jin, N. Zhang, Y. Long, C. A. Parent, and P. N. Devreotes, *Science*, **287**, 1034 (2000).

[60] H. Shimazaki, and S. Shinomoto, *Neural. Comput.*, **19**, 1503 (2007).

[61] D. Mortimer, et al., *Proc. Natl. Acad. Sci. U S A*, **106**, 10296 (2009).

[62] W-J Rappel, and H. Levine, *Phys. Rev. Lett.*, **100**, 228101 (2008).

[63] M. Sussman, *Methods Cell Biol.*, **28**, 9 (1987).

[64] D. A. Lauffenburger, and J. L. Linderman, *Receptors*, **Oxford Univ Press**, London (1993).

[65] M. S. Roulston, *Physica D*, **125**, 285 (1999).

[66] H. B. Barlow, *Proc. R Soc. Lond B Biol. Sci.*, **212**, 1 (1981).

[67] F. Rieke, and D. A. Baylor, *Biophys J.*, **75**, 1836 (1998).

[68] D. Bray, M. D. Levin, and C. J. Morton-Firth, *Nature*, **393**, 85 (1998).

[69] V. Sourjik, and H. C. Berg, *Proc Natl Acad Sci U S A*, **99**, 123 (2002).

[70] C. A. Parent, and P. N. Devreotes, *Science*, **284**, 765 (1999).

[71] D. Fuller, W. Chen, M. Adler, A. Groisman, H. Levine, W-J Rappel, and W. F. Loomis, *Proc Natl Acad Sci U S A*, **107**, 9656 (2010).

[72] W. Bialek, and S. Setayeshgar, *Phys. Rev. Lett.*, **100**, 258101 (2008).

[73] K. Wang, W-J Rappel, R. Kerr, and H. Levine, *Phys. Rev. E*, **75**, 061905 (2007).

[74] R. G. Endres, and N. S. Wingreen, *Phys Rev Lett*, **103**, 158101 (2009).

[75] B. Hu, D. Fuller, W. F. Loomis, H. Levine, and W-J Rappel, *Phys. Rev. E*, **81**, 031906 (2010).

[76] S. Kay, *Prentice Hall*, **Upper Saddle River** (1993).

[77] B. Hu, W. Chen, W-J Rappel, and H. Levine, *Phys. Rev. Lett.*, **105**, 048104 (2010).

[78] H. Gudbjartsson, and S. Patz, *Magn. Reson Med.*, **34**, 910 (1995).

[79] B. Alberts, *et. al.*, *Molecular biology of the cell*, Garland Science, (2002).

[80] M. B. Elowitz, A. J. Levine, E. D. Siggia, and P. D. Swain, *Science*, **207**, 1183 (2002); P. S. Swain, M. B. Elowitz, and E. D. Siggia, *Proc. Natl. Acad. Sci. U S A*, **99**, 12795 (2002).

[81] W. J. Blake, M. Kærn, C. R. Cantor, and J. J. Collins, *Nature*, **422**, 633 (2003).

[82] J. M. Raser, and E. K. O'Shea, *Science*, **309**, 2010 (2005).

[83] J. M. Pedraza, and A. van Oudenaarden, *Science*, **307**, 1965 (2005).

[84] L. Cai, N. Friedman, and X. S. Xie, *Nature*, **440**, 358 (2006).

[85] C. A. Parent, and P. N. Devreotes, *Science*, **284**, 765 (1999).

[86] H. C. Berg, and E. M. Purcell, *Biophys. J.*, **20**, 193 (1977).

[87] J. Paulsson, *Nature*, **427**, 415 (2004).

[88] M. L. Simpson, C. D. Cox, and G. S. Saylor, *J. Theor. Biol.*, **229**, 383 (2004).

[89] W. Bialek, and S. Setayeshgar, *Proc. Natl. Acad. Sci. U S A*, **102**, 10040 (2005); W. Bialek, and S. Setayeshgar, *Phys. Rev. Lett.*, **100**, 258101 (2008).

[90] T. Shibata, and K. Fujimoto, *Proc. Natl. Acad. Sci. U S A*, **102**, 331 (2005).

[91] S. Tănase-Nicola, P. B. Warren, and P. R. ten Wolde, *Phys. Rev. Lett.*, **97**, 068102 (2006).

[92] Gašper Tkačik, T. Gregor, and W. Bialek, *PLoS ONE*, **3**, e2774 (2008).

[93] E. Levine, and T. Hwa, *Proc. Natl. Acad. Sci. U S A*, **104**, 9224 (2007).

[94] K. Wang, W-J Rappel, R. Kerr, and H. Levine, *Phys. Rev. E*, **75**, 061905 (2007); W-J Rappel, and H. Levine, *Phys. Rev. Lett.*, **100**, 228101 (2008).

[95] R. G. Endres, and N. S. Wingreen, *Proc. Natl. Acad. Sci. U S A*, **105**, 15749 (2008); R. G. Endres, and N. S. Wingreen, *Phys. Rev. Lett.*, **103**, 158101 (2009).

[96] B. Hu, D. Fuller, W. F. Loomis, H. Levine, and W-J Rappel, *Phys. Rev. E*, **81**, 031906 (2010); B. Hu, W. Chen, W-J Rappel, and H. Levine, *Phys. Rev. Lett.*, **105**, 048104 (2010).

[97] B. K. Øksendal, *Stochastic differential equations: an introduction with applications*, **Springer**, Berlin (2000).

[98] L. Pechenik, and H. Levine, *Phys. Rev. E*, **59**, 3893 (1999).

[99] J. C. Cox, J. E. Ingersoll, and S. A. Ross, *Econometrica*, **53**, 385 (1985).

[100] S. M. Block, J. E. Segall, and H. C. Berg, *J. Bacteriol.*, **154**, 312 (1983).

[101] P. Cluzel, M. Surette, and S. Leibler, *Science*, **287**, 1652 (2000); E. A. Korobkova, T. Emonet, J. M. G. Vilar, T. S. Shimizu, and P. Cluzel, *Nature*, **428**, 574 (2004); E. A. Korobkova, T. Emonet, H. Park, and P. Cluzel, *Phys. Rev. Lett.*, **96**, 058105 (2006).

[102] Y. Tu, and G. Grinstein, *Phys. Rev. Lett.*, **94**, 208101 (2005).